Long-term X-ray variability of Active Galactic Nuclei and X-ray Binaries

Dissertation
zur Erlangung des Grades eines
Doktors der Naturwissenschaften
der Fakultät für Mathematik und Physik
der Eberhard-Karls-Universität Tübingen

vorgelegt von

Sara Benlloch García

aus Madrid
2004

Erweiterte deutsche Zusammenfassung

Sara Benlloch García
Langzeitvariabilität im Röntgenbereich von
Aktiven Galaxienkernen und Röntgendoppelsternen

In dieser Dissertation beschäftige ich mich mit der Langzeitvariabilität von zwei Klassen von Röntgenobjekten: Aktiven Galaxiekernen (engl. *Active Galactic Nuclei*, AGN) und Röntgendoppelsternen (engl. *X-ray Binaries*, XRBs).

Variabilität im Röntgenbereich ist ein allgemeines Phänomen in vielen astronomischen Quellen. Variabilität ist eine lange bekannte Eigenschaft von AGN, die in allen Wellenlängen und auf Zeitskalen (von Dekaden zu Tagen/Stunden) auftritt. Die Veränderungen scheinen aperiodisch zu sein und variable Amplituden zu haben. Es gib einige Berichte über das periodische Verhalten auf Zeitskalen von einigen Kilosekunden in Form sogenannter quasiperiodischer Oszillationen (QPO). Die Bestätigung einiger dieser Modulationen ist jedoch noch unklar (z.B. Priedhorsky & Holt, 1987; Schwarzenberg-Czerny, 1992; Wijers & Pringle, 1999; Ogilvie & Dubus, 2001). In einer kleinen aber wachsenden Zahl von hellen XRBs ist eine dritte (oder "superorbitale") Periode zusätzlich zu den üblichen Periodizitäten zu beobachten. Solche langfristigen Veränderungen helfen, Fragen über die Struktur der Akretionsscheiben von Röntgendoppelsternen, das Vorhandensein eines dritten Objektes in solchen Systemen, die intrinsische Variationen aufgrund von Änderung der Massenakretionsrate oder der Opazität im nahe gelegenen bedeckenden Material und über die Natur der nicht immer beobachtbaren *transienten* Quellen zu beantworten (Smale & Lochner, 1992).

Nach einer Einleitung in die Röntgenastronomie im Kapitel 1 folgt in Kapitel 2 eine Beschreibung der Klassifikationen, der beobachteten Eigenschaften und der Variabilitätscharakteristika von AGN und von XRBs.

Kapitel 3 bezieht sich auf mathematische Methoden der Zeitreihenanalyse. Zur Zeit werden in der Astronomie vor allem zwei Techniken für die Variabilitätsanalyse, speziell der Periodensuche, angewandt: Periodogramm- und Faltungsmethoden. Andere Methoden, wie das dynamische Periodogramm oder die Wavelet-Zerlegung einer Lichtkurve können Informationen über eine mögliche spektrale Variabilität der Daten (d.h. eine Änderung von Perioden, Amplituden und Phasen) geben. Methoden, welche die Röntgenvariabilität direkt im Zeitbereich überprüfen, wie die Strukturfunktion (SF) und das *excess pair fraction* (EPF), werden ebenfalls häufig in der astronomischen Zeitreihenanalyse verwendet. Eine weitere Methode im Zeitbereich ist das lineare Zustandsraummodell (LSSM) welches das Rauschen in den Daten explizit modelliert und eine Abschätzung des versteckten stochastischen Prozesses erlaubt.

Im Anschluß daran werden in Kapitel 4 Methoden besprochen, welche die Signifikanzniveaus für das Bestehen von QPOs in Röntgenlichkurven bestimmen und die den Charaker des roten Rauschens der astronomischen Objekte in Betracht ziehen.

Die folgenden Kapitel dieser Dissertation enthalten Ergebnisse von Langzeitvariabilitätsstudien, in denen die in den vorhergehenden Kapiteln beschriebenen Methoden und Theorien angewendet wurden. In Kapitel 5 werden zwei Variabilitätsstudien von AGN vorgestellt. Ich berichte über die Analyse von insgesamt ~110 ks Beobachtungen des AGN Cen A, die mit dem Satelliten Rossi X-ray Timing Explorer (*RXTE*) zwischen 1996 und 2000 durchgeführt wurden. Spektrale und zeitliche Variabilitäten auf Zeitskalen von Jahren bis zu Minuten sind zu beobachten. Das Röntgenspektrum kann durch ein stark absorbiertes Potenzgesetz mit Photonenindex 1.8 und einer schmalen Eisenlinie gut beschrieben werden. Die gemessene Säulendichte verringerte sich um ungefähr 30% zwischen 1996 und 2000, während der ermittelte 2–10 keV Kontinuums-Fluß zwischen 1996 und 1998 konstant blieb, jedoch in 2000 um 60% zunahm. Da in allen Beobachtungen der Fluß der Eisenlinie nicht schwankte, wurde eine entsprechende Abnahme ihrer Äquivalentsbreite beobachtet. Es wurde kein Hinweis auf ein Reflexions-Kontinuum im Spektrum gefunden. Wir stellen die Deutung der Stärke der Eisenlinie durch Monte-Carlo Simulationen verschiedener Geometrien dar.

Durch die Anwendung von *epoch-folding* und Periodogrammanalyse auf eine *XMM-Newton* Beobachtung der Seyfert Galaxie Mrk 766, konnte über eine mögliche QPO auf einer Zeitskala von 4200 s berichtet werden (Boller et al., 2001). Unsere Berechnung der Signifikanz dieser QPO zeigt jedoch, daß die 4200 s Modulation nicht auf dem 95% Niveau signifikant ist. Ich stelle fest, daß die 4200 s Eigenschaft ein Kunstprodukt des roten Rauschen und nicht das Resultat eines physikalisches Prozesses innerhalb der Galaxie ist.

In Kapitel 6 wird die Zeitvariabilität von Langzeitlichkurven, die mit dem *All-Sky Monitor* (ASM) an Bord des *Rossi X-ray Timing Explorer* RXTE gewonnen wurden, untersucht. Resultate der Suche nach Periodizitäten in den ASM Lichtkurven von Röntgendoppelsternen werden dargestellt. Die ASM Lichtkurven zeigen eine große Vielzahl von Phänomenen.

Zum Abschluß dieser Dissertation gibt Kapitel 7 eine Zusammenfassung und einen Ausblick auf zukünftige Arbeiten.

Abstract

Sara Benlloch García
Long-term X-ray variability of Active Galactic Nuclei and X-ray Binaries

In this thesis I present long-term X-ray variability studies of sources belonging to two of the big groups of objects present in the X-ray universe: the Active Galactic Nuclei (AGN) and the X-ray Binaries (XRBs).

X-ray variability is a common phenomenon in many astronomical sources. Variability has long been known to be a property of AGN at all wavelengths and time scales from decades to days/hours (Peterson, 2001). The variations appear to be aperiodic and have variable amplitude. There have been reports of periodic behavior at time scales of a few kiloseconds, in the form of quasi-periodic oscillations (QPO). However, the veracity of some of these modulations is still unclear. X-ray variability on long time scales (from days to years) has been also found in many XRBs, but its origin is not always clear (e.g., Priedhorsky & Holt, 1987; Schwarzenberg-Czerny, 1992; Wijers & Pringle, 1999; Ogilvie & Dubus, 2001). In a small but growing number of bright XRBs a third (or "superorbital") period is present in addition to the usual periodicities. Such long-term variations assist in answering questions about the structure of accretion disks in X-ray binary systems, the presence of third bodies in such systems, intrinsic variations due to changing mass accretion rates or opacity changes in nearby obscuring material, and the nature of transient sources (Smale & Lochner, 1992).

After an introduction to X-ray astronomy in chapter 1, a description of the classification, observational properties, and variability characteristics of AGN and XRBs are presented in chapter 2.

Chapter 3 refers to mathematical methods for the time series analysis. Currently, two methods for the variability analysis of astronomical sources, especially in searching for periodic signals, are common in astronomy: periodogram analysis and epoch-folding. Other methods, as the dynamical power spectra or the wavelet decomposition of the light curve, can give information on the possible variable spectral properties of the data (i.e., change of periods, amplitude, and phases). Methods to examine the X-ray variability directly in the time domain, as the Structure Function (SF) and Excess Pair Fraction (EPF), are also commonly used in time-series analysis in astronomy. An alternative analysis method in the time domain is the Linear State Space Model (LSSM) which explicitly models the noise of astronomical data and allows to estimate the hidden stochastic process.

For the detection of periodic signals, it is worth scrutinizing the methods used to determine their significance. Methods to compute significance levels for the existence of QPOs in X-ray light curves which take the red-noise character of the astronomical objects into account are discussed in chapter 4.

The following chapters of the thesis contain the results of long-term variability studies applying the methods and theory described in the previous chapters. In chapter 5 two variability studies of AGN are presented. I report on the analysis from ~110 ks of X-ray observations of the AGN Cen A carried out with the Rossi X-ray Timing Explorer (*RXTE*) satellite between 1996 and 2000. Spectral and temporal variability on time scales from years to tens of minutes are present. The X-ray spectrum can be well described by a heavily absorbed power-law with photon index 1.8 and a narrow iron line due to fluorescence of cold matter. The measured column depth decreased by about 30% between 1996 and 2000, while the detected 2–10 keV continuum flux remained constant between 1996 and 1998, but increased by 60% in 2000. Since in all observations the iron line flux did not vary, a corresponding decrease in equivalent width was noted. No appreciable evidence for a reflection continuum in the spectrum was detected. We present the interpretation of the iron line strength through Monte Carlo computations of various geometries.

Applying epoch-folding and periodogram analysis to the *XMM-Newton* observation of the Seyfert galaxy Mrk 766, a possible QPO at a time scale of 4200 s has been reported (Boller et al., 2001). Our computation of the significance of this QPO, however, shows that the 4200 s peak is not significant at the 95% level. We conclude that the 4200 s feature is an artifact of the red-noise process and not the result of a physical process within the galaxy.

In chapter 6 temporal variability behavior from long-term light curves obtained with the *All-Sky Monitor* (ASM) on board the *RXTE* is reviewed. Results of searches for periodicities in the ASM light curves from X-ray binaries are presented. The ASM light curves show a wide variety of phenomena.

In conclusion, chapter 7 presents a summary and outlook on future work.

Contents

List of Figures

CHAPTER 1

Introduction

1.1   X-ray astronomy

The initial discovery of X-ray radiation was made by Wilhelm Röntgen in 1895, a German scientist who found this new type of radiation quite by accident when experimenting with vacuum tubes. He took an X-ray photograph of his wife's hand which clearly revealed her wedding ring and her bones. Röntgen called this new form of radiation "X" to indicate it was an unknown type, although they are still referred to Röntgen rays in German-speaking countries. Over the next decades X-rays proved to be an invaluable tool for the investigation of the micro-world of the atom, the development of the quantum theory of matter, and the research in medical sciences.

Although the more energetic X-rays ($E > 30\,\mathrm{keV}$) can penetrate the air at least for distances of meters (otherwise, Röntgen would never have observed them), the Earth's atmosphere is thick enough that virtually none are able to penetrate from outer space all the way to the Earth's surface. It is thus impossible to observe X-rays from astronomical sources with ground-based instruments. To see X-rays from the sky, the X-ray detectors must be flown above most of the atmosphere. It becomes possible through the use of rockets and balloons as well as satellites and spacecraft.

Astronomers got their first quick look at the X-ray sky from brief rocket flights during the late 1940s, when radiation detectors aboard rockets were carried above the atmosphere for a few minutes where they detected X-rays coming from the Sun. It took more than a decade before a greatly improved detector discovered X-rays coming from sources beyond the solar system.

The first rocket flight which successfully detected, again quite by accident, a cosmic source of X-ray emission was launched in 1962 by a group at American Science and Engineering (AS&E). The team of scientists on this project included Riccardo Giacconi, Herb Gursky, Frank Paolini, and Bruno Rossi. This rocket
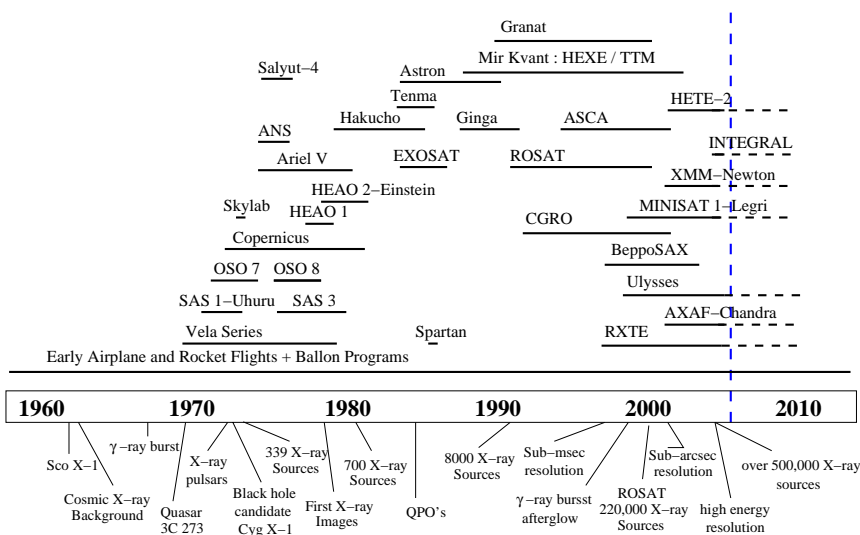
Figure 1.1: X-ray astronomy missions, from 1960–2003

flight detected a very bright source they named Sco X-1, because it was the first X-ray source found in the constellation Scorpius (Giacconi et al., 1962). For this and other pioneering work in astronomy, Riccardo Giacconi won the 2002 Nobel Prize in Physics and several other awards. Major advances in the field began in the 1970s with the use of satellites equipped with X-ray detectors. The first of these, *Uhuru*, was launched in 1970. The satellite's name means "Freedom" in Swahili. This and later missions have observed X-rays from different kinds of objects in the sky. Figure 1.1 represents a brief history of X-ray astronomy with the most notable X-ray missions and their most significant contributions.

By rocket flights in the 1960s, scientists began to observe X-rays from stellar sources in our Galaxy. These objects were bright in X-rays but were rather faint optically. More observations with *Uhuru* showed them to be pulsating regularly and to show X-ray eclipses when observed for longer periods. The only explanation was a close binary system in which a rapidly spinning neutron star was responsible for the X-rays. Because the binary periods were so short, it was recognized that these systems must be so close as to be interacting, with mass exchanged from the "normal" star to the compact star. In these X-ray Binaries, the X-rays originate from material falling from the normal star to the neutron star in a process called accretion. The binary nature of the systems allowed for measurements of the mass of the neutron star. For other systems, the inferred mass of

the degenerate object supported the ideas of the existence of black holes, as they were too massive to be neutron stars. The first object identified as a black hole candidate was Cyg X-1 (Bolton, 1972; Webster & Murdin, 1972). Finally, some of these galactic X-ray sources were found to be highly variable; in fact, some sources would appear in the sky, remain bright for a few weeks, and then fade again from view. Such sources are called "X-ray Transients", and were first discovery in 1967 by the identification of the bright X-ray source, Cen X-2 (Francey et al., 1967). The inner regions of some galaxies were also found to emit X-rays. The X-ray emission from these "Active Galactic Nuclei" is believed to originate from ultra-relativistic gas near a very massive black hole at the galaxy's center. The first detection of this class of object was reported by Friesdman & Byram (1967), who using sounded rockets made the detection of the quasar 3C 273 in 1967. Lastly, diffuse X-ray emission was found to exist all over the sky. It was initially recognized in data from the 1962 rocket flight which first detected Sco X-1. It is now known that a large fraction (possibly all) of this background is due to faint unresolved sources (Setti & Woltjer, 1979; Mather et al., 1990; Hasinger, 1996).

In 1978, the *Einstein* X-ray observatory was the first large focusing X-ray telescope to be placed in orbit. This telescope produced high-resolution images and accurate locations for thousands of cosmic X-ray sources. This and later missions have observed X-rays from ordinary stars, white dwarf stars, neutron stars, black holes, interstellar shock waves produced by stellar explosions, the nuclei of galaxies, and the hot gas in clusters of galaxies. These X-ray images reveal regions in space where particles are accelerated to very high energies by phenomena such as strong magnetic fields, violent explosions, or intensive gravitational forces.

1.2   X-ray variability

The first clear example of an object variable in X-ray was reported by Byram, Chubb & Friedman (1966) who found that the previously detected source Cyg X-1 had varied by a factor of several compared to its strength nine months earlier. With the launch of the *Uhuru* X-ray satellite, monitoring of X-ray stars for prolonged periods of time was possible. It was discovered that the X-ray emission from these stars undergoes rapid, intense, and sometimes periodic variations. Combined observations with optical and X-ray telescopes demonstrated that these X-ray sources are members of binary systems in which matter streams from a normal star onto a nearby collapsed object.

Progress in the study of compact Galactic X-ray sources has come mostly through the analysis of their time variations. Rapid aperiodic variability on time

scales from milliseconds to seconds is common to all types of X-ray binaries, XRBs (see van der Klis, 1995, for a review). This includes the types of variability that are usually called quasi-periodic oscillations (QPOs) and noise, and also sometimes flickering, irregular flaring, fluctuations, etc. Such rapid variability arises in the immediate vicinity of the compact object and provides a probe of changes in physical parameters, such as accretion rate, optical depth, and temperature. Periodic variations corresponding to neutron star rotations and orbital motion are also seen on time scales ranging from milliseconds to tens of days (White, Nagase & Parmar, 1995). Furthermore, explosive thermonuclear processes on neutron stars give rise to X-ray bursts (Lewin, Paradijs & Taam, 1995). On a small number of sources (e.g., SMC X-1, Her X-1, LMC X-4) a third or "superorbital" period is also present, typically on a scale of tens to hundreds of days. Such long-term variations assist in answering questions about the structure of accretion disks in X-ray binary systems, the presence of third bodies in such systems, intrinsic variations due to changing mass accretion rates or opacity changes in nearby obscuring material, and the nature of transient sources (Smale & Lochner, 1992). Priedhorsky & Holt (1987) provide a summary of the observations and interpretations of these long-term cycles. The data bases from long-term X-ray scanning experiments, such as obtained by *Vela 5B* (1969–1979), the All Sky Monitor on *Ariel 5* (1974–1980), the Burst and Transient Source Experiment (BATSE) aboard *CGRO* (1991–2000), and the All Sky Monitor (ASM) on *RXTE* (since 1996), have provided opportunities for studying such long-term variations in cosmic X-ray sources.

Irregular X-ray variability is also a common phenomenon of Active Galactic Nuclei, AGN. The X-ray flux shows the fastest variability in any wavelength range (McHardy, 1988), which indicates that it originates from a small region very close to the central object (see Mushotzky, Done & Pounds, 1993, for a review). In fact, the AGN light curves fluctuate over wide range of time scales, from years to hours. There were some reports of periodic behavior, in the form of QPOs, at time scales of a few kiloseconds, but some of these are controversial and are still a matter of discussion (see Benlloch et al., 2001b, and references therein).

1.3   Outline of this Thesis

The main subject of this thesis is the study of the temporal variability on long time scales of two of the big groups of X-ray objects presented in the last sections, AGN and XRBs.

Chapter 2 introduces the definition and main variability characteristics of AGN and XRBs, giving an overview about the classification and observational properties, and introducing the physical models which may be responsible for the long time variability of these objects.

Chapter 3 refers to mathematical methods for the variability analysis of astronomical sources. This includes the classical period determination methods based either on Fourier decomposition analysis or on folding techniques, which are complemented by an interpretation in the two-dimensional time-frequency domain. Methods to examine the X-ray variability directly in the time domain are also presented. Finally an alternative analysis method in the time domain based on modeling the light curve with stochastic processes, the Linear State Space Model, is described.

For the detection of periodic signals, it is worth scrutinizing the methods used to determine their significance. In chapter 4, I present a study of how to compute this significance using Monte Carlo simulations of light curves with the method of Timmer & König (1995) and using periodogram analysis and epoch-folding to detect periodicity.

The rest of the thesis contains results of applying these methods and the theory described in the previous chapters to some examples of astronomical time series. In chapter 5, I present the data analysis of two prominent AGN, Cen A and Mrk 766. Section 5.1 describes the results of three observations of Cen A performed by the Rossi X-ray Timing Explorer (*RXTE*) – one of 10 ks in 1996 August, one of 74 ks in 1998 August, and one of 25 ks in 2000 January (Benlloch et al., 2001a). Preliminary results from the 1996 August observation, using earlier versions of the response matrix and background models, have been presented by Rothschild et al. (1999). Here the data are re-analyzed using the new and improved response matrices and background models, and the results on all three observations are presented.

In section 5.2, I present the light curve of Mrk 766 observed by *XMM-Newton* on 20th May 2000 during revolution 0082 lasting ~60 ks. As a result of the analysis of this observation, a QPO in the range of 4200 s was claimed by Boller et al. (2001). I present the re-analysis of the Mrk 766 *XMM-Newton* light curve applying the "significance level" methods outlined in chapter 4 to the putative QPO. We find that the QPO claimed in Boller et al. (2001) has in fact low statistical significance (Benlloch et al., 2001b).

In chapter 6 time variability studies of galactic sources are presented. It summarizes the results from a program aiming to study the long time behavior of a larger sample of XRBs. The goal is to identify observational signatures in order to constrain physical causes of the variability. Such a program has only recently become feasible with the availability of data from the ASM on *RXTE*. This instrument has been monitoring the entire sky for X-ray sources since 1996 February.

The ASM light curves show a wide variety of phenomena. Different long-term behaviors such as stable and non stable periods, temporary periods, or just stochastic behavior are present. We have collected a list of 27 Low and High Mass X-ray Binaries (LMXB & HMXB) monitored with the ASM and have studied their long-term variability. I present the detailed long-term variability study for six of these sources (Cyg X-1, Aql X-1, GX 339−4, 4U 1705−44, 4U 1957+115, and SMC X-1) and summarize the results of the other 21 sources.

At last, a summary and an outlook for future work are presented as conclusion of this thesis in chapter 7.

On the nature of X-ray variability

2.1 *An introduction to Active Galactic Nuclei*

There are over ten billion galaxies visible in the Universe and the vast majority are termed "normal" galaxies. These radiate by the combined output of their billions of stars and most fall into the category of spiral, elliptical, or irregular galaxies. There are some galaxies, about the 5% of all galaxies, which are characterized by extreme brightness and activity of their central regions. These are the active galaxies in which a significant fraction of its total luminosity, between 10^{10}–10^{14} $L_{\odot}$, is radiation not ultimately attributed to stars. Just only the very central region of a galaxy is active, therefore they are called Active Galactic Nuclei (AGN). Variability of a significant fraction of the luminosity of AGN with time scales measured in weeks to days provides critical evidence of the very compact nature of the central engine. The source of this extreme central activity is thought to be the accretion of material onto a supermassive black hole with an estimated mass of $\sim 10^{8}$ $M_{\odot}$. A large number of classes and sub-classes exist, which mainly developed historically (Krolik, 1999).

2.1.1 *Unified model*

The differences among apparently diverse classes of AGN are mainly the result of the orientation of the spin axis of the supermassive black hole with respect to the observer (Antonucci, 1993; Urry & Padovani, 1995). The unified model, also called "unification-by-orientation" scenario, assumes the following general structure for all AGN (see Fig. 2.1):

- At the very center there is a **supermassive black hole**, which accretes matter from an **accretion disk**. The internal friction of the accreting material heats the disk which therefore emits X and UV radiation.
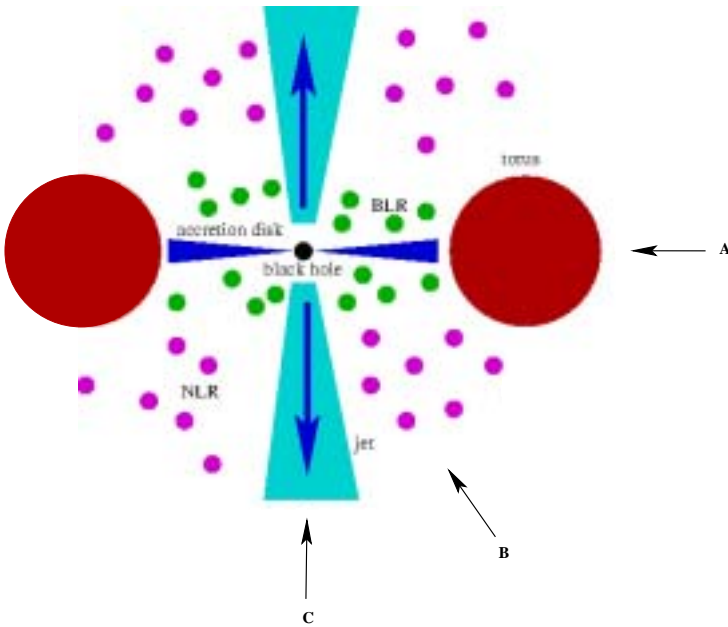
Figure 2.1: Unified model (adapted from `http://www.astro.soton.ac.uk/~crk/PH227/node55.html`).

- A hot **corona** above the accretion disk populates the inner region and may also play a role in producing the hard X-ray continuum.

- Broad emission lines are produced in clouds orbiting at high velocity above the disk and perhaps by the disk itself. The size of this **broad-line region** (BLR) is restricted to ~1 pc or less.

- A thick **torus** composed of dust and cold, largely molecular gas absorbs most of the X-ray emission and the UV radiation coming from the central region and obscures the BLR from transverse lines of sight; some continuum and broad-line emission can be scattered into the line of sight by hot electrons that pervade the region. The dusty torus emits mainly infrared light.

- Beyond the torus, slower moving clouds of gas produce emission lines with narrower widths. This **narrow line region** (NLR) extends from a few tens of parsecs to over a kiloparsec.

- In a radio-loud AGN a strong **jet** of relativistic particles emanates perpendicular to the plane of the accretion disk. The radio emission originates from highly relativistic particles inside the jet. The synchrotron emission from the jet may extend up into the X-ray regime and scattered photons reach γ-ray energies.

AGN generally come in two flavors: **radio-quiet** or **radio-loud**, depending on whether the ratio of the fluxes emitted in the radio and in the optical band is less or greater than one, respectively. Radio-loud objects constitute the smaller fraction ($\sim$10%) of AGN but they have been studied in great detail and seem to form a more extreme population. Radio observations reveal directed outflows (jets), often with apparent superluminal velocities. Depending on the spatial orientation with respect to our line of sight we observe the different types of AGN (for a full discussion see Urry & Padovani, 1995). Based also on the characteristics of their optical and ultraviolet spectra, AGN can be separated into three broad types (see Fig. 2.2 for a scheme of the AGN classification) :

1. If we look at an offset angle of the order of $30°$ from the jet axis (observer B in Fig. 2.1), at which both the narrow-line and broad-line regions are visible, we are looking at the Type 1 AGN. They show bright continua and broad as well as narrow emission lines. Infrared emission from the torus can be detected , as well as the jets in radio-loud objects, and X-ray and UV emission from the accretion disk. In the radio-quiet group, these include the **Seyfert 1 galaxies** (which are relatively low luminosities and therefore are seen only nearby, where the host galaxy can be resolved) and the higher-luminosity radio-quiet quasars, or **quasi-stellar objects** (QSO, which are typically seen at greater distances). The radio-loud Type 1 AGN are called **Broad-line radio galaxies** (BLRG) at low luminosities and **radio-loud quasars** at high luminosities, also called Steep Spectrum Radio Quasars (SSRQ).

2. At larger angular offsets (observer A in Fig. 2.1) the broad-line region will be hidden by the extended molecular torus giving rise to Type 2 AGN. They have weak continua and only narrow emission lines. Infrared emission from the torus can be detected, as well as the jets in radio-loud objects, but not the X-rays and UV emission from the accretion disk. Radio-quiet Type 2 AGN include **Seyfert 2 galaxies** at low luminosities, as well as the **Narrow-emission-line galaxies** (NELG), or the **Low-Ionization Nuclear Emission-Line Regions** (LINERS). Radio-loud Type 2 AGN, often called **Narrow-line radio galaxies** (NLRG), include two distinct morphological types: the low-luminosity **Fanaroff-Riley type I radio galaxies**
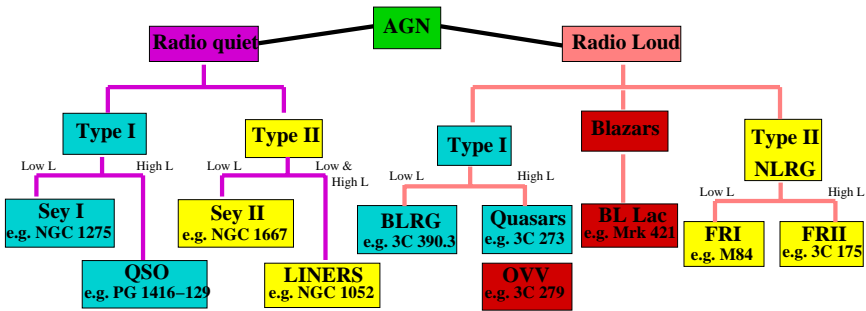
Figure 2.2: AGN classification.

(FR I), which have often-symmetric radio jets whose intensity falls off with increasing distance from the nucleus, and the high-luminosity **Fanaroff-Riley type II radio galaxies** (FR II), which have more highly collimated jets leading to well-defined lobes with prominent hot spots (Fanaroff & Riley, 1974).

3. Looking towards the "central engine" along the jet axis ($< 20°$), i.e., basically directly into the jet (observer C in Fig. 2.1), we observe blazars. Observer C sees the same as observer B if the object is radio-quiet, otherwise looks down the jet and therefore mainly sees the jet emission (radio to X-ray synchrotron and Compton scattered emission). If the central engine is very luminous, X-rays and UV emission from the accretion disk, and the BLR can be observed. Blazars include the **BL Lacertae** (BL Lac) objects, which are radio-loud AGN that lack strong emission or absorption features. A subset of Type 1 quasars, including **Optically Violently Variable** (OVV) quasars, **Highly Polarized Quasars** (HPQ), **Core-Dominated Quasars** (CDQ), or **Flat Spectrum Radio Quasars** (FSRQ) are probably also found at a small angle between the jet and the line of sight. Even though these objects have strong broad emission lines, they have the same blazar-like continuum emission as BL Lac objects. They are characterized by very rapid variability, unusually high and variable polarization, high brightness temperatures, and superluminal velocities of jet components.

2.1.2 X-ray variability in AGN

Variability has long been known to be a common property of AGN in all the wavelengths and time scales. For a review see Peterson (2001). The variations appear
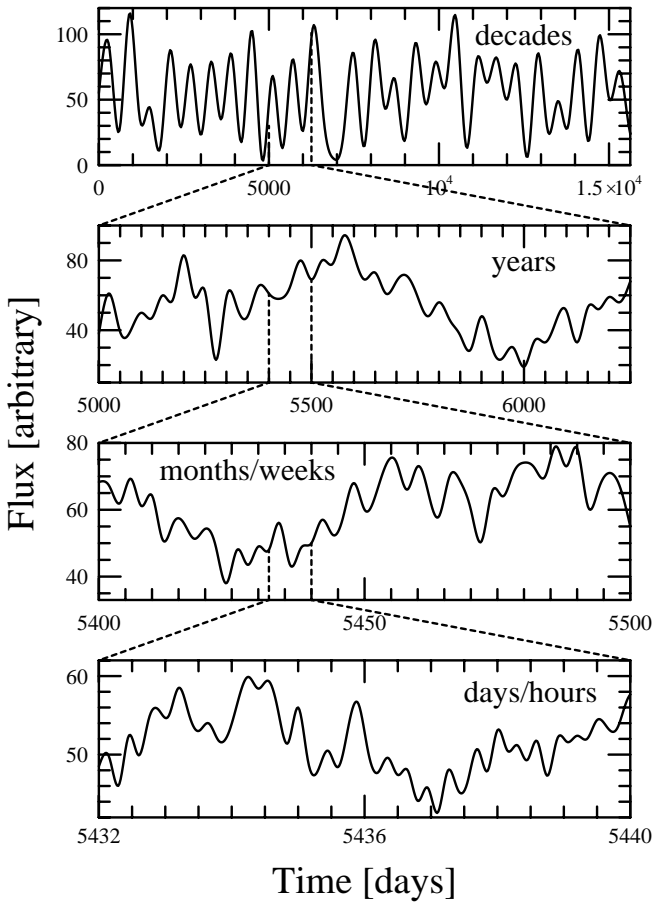
Figure 2.3: Schematic light curves of an AGN on different time scales (Kawaguchi & Mineshige, 1998).

to be aperiodic and have variable amplitude. In fact, the AGN light curves fluctuate over wide time scales from decades to days/hours as can be see in Fig. 2.3. The following three features are typical for different time scales (Kawaguchi & Mineshige, 1998): (1) random up and down fluctuations are show on time scales longer than decades, (2) for variability on shorter time scales there are no typical time scales, and (3) amplitudes of the variations over less than years decrease as the time scales become shorter.

Rapid X-ray variability of AGN is a powerful probe of the innermost regions of AGN and can be used in getting information about the central object, such as mass, accretion rate, geometry and radiation mechanisms (Mushotzky, Done & Pounds, 1993, for a review).

A useful way to characterize variability is in terms of the *Power Spectral Density* (PSD), which is the product of the Fourier transform of the light curve and its complex conjugate, and describes the contribution of variability structures with a given frequency to the total light curve variance. It will be described in detail in chapter 3. The PSD for AGN is often parameterized as a power-law, $P(f) = f^{-\alpha}$. *EXOSAT* data (McHardy, 1988) showed that AGN X-ray variations can be characterized by PSD indices in the range $1 < \alpha < 2$ over time scales of hours to months. The total power in the variations is given by integrating the PSD over all frequencies. Thus, the PSD must turn over at low frequencies (i.e., α as defined above must become less than unity) to prevent divergences in the total power. Such breaks in the PSD are observed in stellar-mass X-ray sources, and scaling AGN relative to stellar-mass systems (which have turnover frequencies $f \sim 0.1\,\mathrm{Hz}$), we expect that the turnover frequencies for AGN will occur at about $10^{-8}\,\mathrm{Hz}$. Edelson & Nandra (1999) find that for the NGC 3516 Seyfert 1 galaxy the turnover frequency is $f \sim 4 \times 10^{-7}\,\mathrm{Hz}$, which correspond to a time scale of about one month.

To date, quasi-periodic oscillations (QPOs) at time scales of a few kiloseconds have been claimed for some AGN: NGC 4151 (Fiore et al., 1989), NGC 6814 (Mittaz & Branduardi-Raymont, 1989), NGC 5548 (Papadakis & Lawrence, 1993b), NGC 4051 (Papadakis & Lawrence, 1995), RX J0437.4−4711 (Halpern & Marshall, 1996), IRAS 18325−5926 (Iwasawa et al., 1998), MCG−6-30-15 (Lee et al., 2000), Mrk 766 (Boller et al., 2001), IRAS 13224−3809 (Pfefferkorn et al., 2001), as well as Ton S180, and 1H 0419−577 (Halpern, Leighly & Marshall, 2003). In addition, possible long-term periodicities with periods of months have been claimed for the radio loud AGN Mrk 421, Mrk 501, and PKS 2155−304 (Osone, Teshima & Mase, 2001). Some of these findings, however, are controversial, with the strongest EXOSAT result (NGC 5548) being disputed by Tagliaferri et al. (1996), who attribute it mostly to periodic swapping of detectors. NGC 6814 turned out to be confused with a cataclysmic variable (Madejski et al., 1993; Staubert et al., 1994). At a fundamental level, the physical origin of variations is not known, although accretion-disk instabilities are probably involved. Variable accretion rates have also been considered. In some specific atypical cases, variations have been attributed to variable obscuration of the nuclear source and to microlensing due to stars in the host galaxy.

2.2 An introduction to X-ray Binaries

Systems composed of two stars that orbit around their common center of mass are called binary star systems. A special class of binary systems are the X-ray binaries, which are made up of a compact object and a companion star (see Fig. 2.4). A compact object can be either a neutron star (NS), a black hole (BH), or a white dwarf (WD). These systems produce X-rays by the accretion of material from the companion star onto the compact object.

NSs are compact objects that are created in the cores of massive stars during supernova explosions. The core of the star collapses and crushes together every proton with a corresponding electron turning each electron-proton pair into a neutron. The neutrons, however, can often stop the collapse and remain as a neutron star. Such objects have a typical radius of 10–15 km and a mass around $1.4 M_\odot$. BHs are completely collapsed objects (a space-time singularity). They are believed to form from the gravitational collapse of astronomical objects containing two or more solar masses. Specifically defined, a BH is a region in space with gravitation so strong that even light cannot escape from it. The radius of such region, called "Schwarzschild radius", can be calculated by using the equation for escape velocity, $v_{\mathrm{escape}} = \sqrt{2GM/R}$, where G is the Newton's gravitational constant, M the mass of the object, and R the distance from the center of the object. Setting the escape velocity equal to the speed of light c, and solving for R, we obtain the "Schwarzschild radius", $R_S = 2GM/C^2$. For an object with the mass of our Sun, R_S equals about 3 km. An X-ray source is classified as black hole X-ray binary (BHXB) if the observed mass function, or other less direct dynamical evidence, places the mass of the compact object above $3 M_\odot$, or if the spectral and temporal characteristic of the source are similar to those of the well-established BHXBs (e.g., GX 339−4, 1E 1740.7−2942, GRS 1915−105, GRO J1719−24, Cyg X-1). WDs are stars of low and medium mass that has exhausted most or all of its nuclear fuel and has collapsed to a very small size. Typically, a WD has a radius equal to about 0.01 times that of the Sun, and a mass roughly equal or less than the Sun. Cataclysmic variables (CVs) are binary systems which have a white dwarf as the compact companion. They are typically small with an orbital period in the range 1–10 hr. CVs are also fairly faint in X-rays, and are not included in this work.

2.2.1 The classification of X-ray binaries

X-ray binaries can be further divided into two different classes according the mass of the companion star: high-mass X-ray binaries (HMXB) and low-mass X-ray binaries (LMXB) (see Fig. 2.5).

In HMXBs the companion is an O or B star with $M_S \geq 10 M_\odot$ and whose
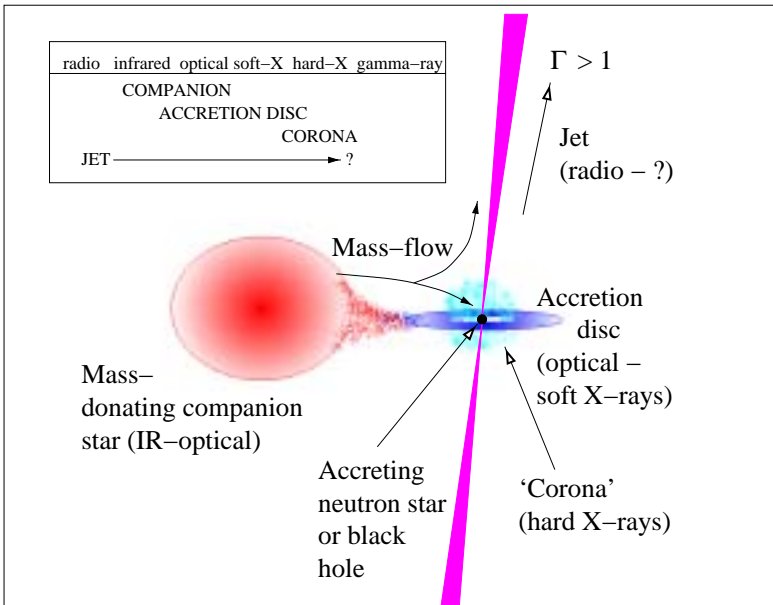
Figure 2.4: Sketch of an X-ray binary. The localization of the sites believed to correspond to observed emission at different wavelengths are indicated (Fender, 2002, Fig. 1).

optical/UV luminosity may be comparable to, or greater than, that of the X-ray source. X-ray heating is minimal, with the optical properties dominated by the companion star. The X-ray emission in these sources is due to wind accretion mass transfer from the early-type mass-loosing star by the compact companion. Roche-lobe overflow can also be a supplement to the mass transfer rate in HMXBs (Lewin, van Paradijs & van den Heuvel, 1995). Actually, the number of known HMXBs is about 130 (see Liu, van Paradijs & van den Heuvel, 2000, for a recent catalog).

Conventionally, HMXBs containing NS can be further divided into two sub-groups: those in which the primary is a Be star (Be/X-ray binary) and those in which the primary is a supergiant (SG/X-ray binary). The majority of the known HMXBs are Be/X-ray systems. A Be star is an early-type non-supergiant star, which at some time has shown emission of Balmer lines which originate from circumstellar material (Slettebak, 1988). Most Be/X-ray binaries have relatively wide orbits with moderate eccentricity, with periods generally $\gtrsim 20$ days. Their compact companions spend most of their time far away from the circumstellar disk surrounding the Be stars (Apparao, 1994). X-ray outbursts are expected dur-
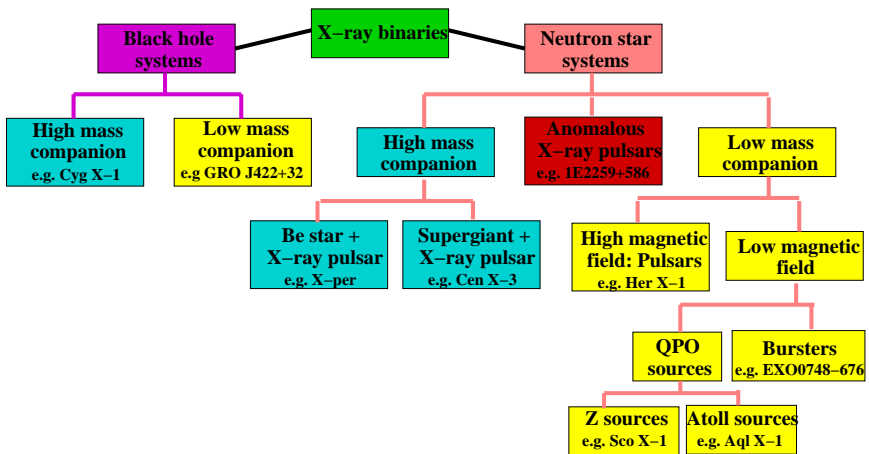
Figure 2.5: Taxonomy of the X-ray binaries.

ing the time of the NS's periastron passage, from low velocity and high-density wind around Be stars. Such objects are thus collectively termed Be/X-ray transients. In the SG/X-ray binary systems the compact star orbits a supergiant early-type star. The orbital periods are generally less than ∼10 days. The X-ray luminosity is either powered by pure stellar wind accretion or, in the case of the brighter systems, by Roche-lobe overflow via an accretion disk.

In the LMXB the secondary is a low-mass (in general $M_S \leq 1\,\mathrm{M_\odot}$) star, which transfers matter by Roche-lobe overflow. Among the low-mass companion stars we find WDs, late-type main-sequence stars, two A-type stars, and F-G-type subgiants. The optical counter parts of LMXBs are intrinsically faint objects. The spectra of most of them show a few characteristic emission lines. The optical continuum of LMXBs is dominated by the emission from an accretion disk around the compact star, which is predominantly the result of reprocessing of a fraction of the X-rays into optical photons in the disk. The contribution of the secondary is generally negligible. On occasion, however, the presence of the secondary can be discerned in the spectrum (or colors) of the LMXBs. This particular is the case for systems with donors that are or started out as intermediate mass stars, such Her X-1 and Cyg X-2.

The classification as LMXB is mainly based on the spectra obtained from an optical identifications, and/or on the mass function from X-ray pulse arrival time measurements. If neither is available, a classification may be inferred based on the similarity of the X-ray properties to other identified systems. An unidenti-

fied system is classified as an LMXB containing a neutron star if one or more
of the following properties are observed (Liu, van Paradijs & van den Heuvel,
2001): (1) type I X-ray burst, (2) QPOs in the 6–60 Hz range (van der Klis et al.,
1985) (3) the 1–10 keV spectrum is soft with a characteristic temperature of 5–
10 keV, and/or (4) the orbital period is less than about 12 hr. The number of known
LMXBs is about 150 (see Liu, van Paradijs & van den Heuvel, 2001, for a recent
catalog of LMXB).

If the X-ray binary contains a NS, it may be seen to pulse in X-rays. The
material falling in from the companion is funneled by the strong magnetic field
of the NS onto its magnetic poles. It will hit a hard surface and this will shine
in X-rays as an intense hot spot. If the spin axis and the magnetic axis of the
neutron star are not aligned, the radiation sweeps past us once per rotation and we
see X-ray pulsations. These systems are called X-ray pulsars, i.e., X-ray binaries
containing a rotating and strongly magnetized NS that accretes gas from a stellar
companion.

But not all neutron star systems have such intense magnetic fields and it ap-
pears that in many of the LMXB systems the field is much weaker. In these cases
the flow of material onto the NS is more erratic, with the pulsations unstable.
Many of these low magnetic field systems show QPOs. These oscillations seem
to originate from the interaction of the NS with the surrounding accretion disk, or
from instabilities in the captured material caused by the overwhelming intensity
of the X-ray emission. The QPO sources can be observationally divided into two
main categories, known as atoll and Z sources (Hasinger & van der Klis, 1989).
This classification is based on changes in both spectral and timing properties as
the source varies. Z sources are named after a Z-shaped track they produce on
an X-ray color-color diagram (see Fig. 2.6). Atoll sources can fall into one of
the two spectral states, a hard, low luminosity "island" or a soft, high luminos-
ity "banana". They trace an U-shaped or C-shaped track as the source spectrum
evolves between the island and the banana (see Fig. 2.6). These differences be-
tween the two LMXBs categories probably reflect differences in both the mass
accretion rate, $\dot{M}$, and the magnetic field, B, with the Z sources having high lumi-
nosity (typically $> 0.5 L_{\text{Edd}}$) and high magnetic field ($B \geq 10^9$ G) while the atolls
have lower luminosity (generally $< 0.1 L_{\text{Edd}}$) and low magnetic field ($B \ll 10^9$ G)
(Hasinger & van der Klis, 1989). In the frequency range 10^{-2}–10^{-3} Hz the power
spectra of atoll and Z-sources are represented by a power-law with index 1–1.5
(atoll sources) and 1.5–2 (Z sources), which describes the spectrum at low fre-
quencies (below ~1 Hz) and a power law plus exponential cut off with index 0–0.8
(atoll sources), ~0 (Z sources) and $\nu_{\text{cut}} = 0.3$–25 Hz (atoll sources), $\nu_{\text{cut}} = 30$–
100 Hz (Z sources) at higher frequencies. The strength of these two components
correlates with the position of the source in the color-color diagram. On the top
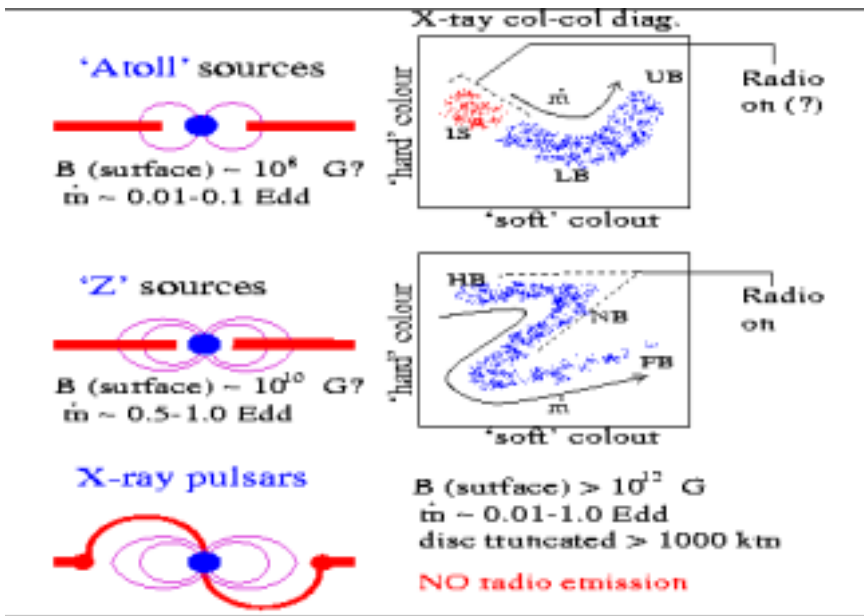
Figure 2.6: Schematic illustrating the X-ray and radio properties of the neutron star X-ray binaries (from Fender, 2002).

of this continuum several types of QPOs in the 6–60 Hz range are seen (van der Klis et al., 1985).

Another phenomenon associated with low magnetic field NS that have low-mass companions are X-ray bursts. These typically last a few seconds to a few minutes, and have a peak luminosity of nearly $10^5 L_\odot$ (Lewin & Joss, 1983). The model for these bursts is that as hydrogen is transferred to the NS from the accretion disk, it builds up in a surface layer of hydrogen, which will burn (in the sense of nuclear fusion) steadily, producing an underlying layer of helium. Eventually the density and temperature in the helium layer reaches a critical point and it too starts burning, releasing a tremendous amount of energy. There is then a brief flash, or burst of X-rays as a thermonuclear explosion. The steady accretion of fresh hydrogen from the disk then continues, and after a similar, but not exact, amount of time another burst will occur.

Furthermore, there is a new class of pulsating objects with spin periods in the 6–12 s range, which are different from "normal" binary X-ray pulsars. These objects are referred to as braking X-ray pulsars (Mereghetti & Stella, 1995) or anomalous

X-ray pulsars (AXP) (van Paradijs, Taam & van den Heuvel, 1995). It has been suggested that AXPs may consist of NSs accreting from a very low-mass companion (Mereghetti & Stella, 1995), or isolated NSs accreting from circumstellar debris (van Paradijs, Taam & van den Heuvel, 1995), or they are isolated NSs with very high magnetic fields, i.e., magnetars related to the soft gamma-ray repeaters (Thompson & Duncan, 1996; Kaspi et al., 2001, 2003).

X-ray binaries are also emitters in other wavelengths. See Fig. 2.4 for a X-ray binary sketch. Radio emission has now been detected from ~20% of all X-ray binaries. In nearly all cases it has been found to be variable and to display a nonthermal spectrum. Synchrotron emission of electrons in jet-like outflows has been established as the most likely emission mechanism (Fender et al., 1999). The radio and optical emission is found to be strongly correlated with hard X-ray emission but anticorrelated with soft X-ray emission (Fender, 2001c; Corbel et al., 2000).

2.2.2   Spectral states

The spectrum of a black hole X-ray binary system usually consists of four components: a blackbody-like component at low energies, an iron line, disk reflection, and a power-law component at high energies ($E^{-\Gamma}$ with power index Γ). The blackbody soft component is seen up to energies of a few keV and is usually attributed to emission from the hot, inner region of an optically thick and geometrically thin disk, and the hard component can extend up to 200 keV and is attributed to the Comptonization of soft photons by energetic electrons (thermally or nonthermally distributed) in the region. Iron Kα line emission has been detected around 6.4 keV (e.g., Wilms et al., 1999; Feng et al., 2001). The line probably originates in the fluorescent emission of cold iron atoms in the accretion disk, which is illuminated by the hard X-ray source.

Black hole candidates are known to exhibit transitions between various X-ray states. Based upon the presence or absence of the soft component at ~1 keV, the luminosity and spectral slope of the emission at higher energies, and the different shapes of the noise components in the PSD, five distinct X-ray states have been reported, namely the "Off state", the "low/hard state" (LS), the "intermediate state" (IS), the "high/soft state" (HS), and the "very high state" (VHS) (see Fig.2.7). The canonical X-ray properties that are observed in different spectral states are summarized in the Tab. 2.1. The following description of the different spectral states is based on that given by Esin et al. (1998).

Systems in the low/hard state have hard power-law spectra with photon index Γ ~1.4–1.9, exponential cutoff around 100 keV, and no (or only weak) evidence of a soft thermal component. The luminosity is generally below ~0.1 $L_{\rm Edd}$. The power spectrum shows strong band-limited noise with a typical strength of 20%–
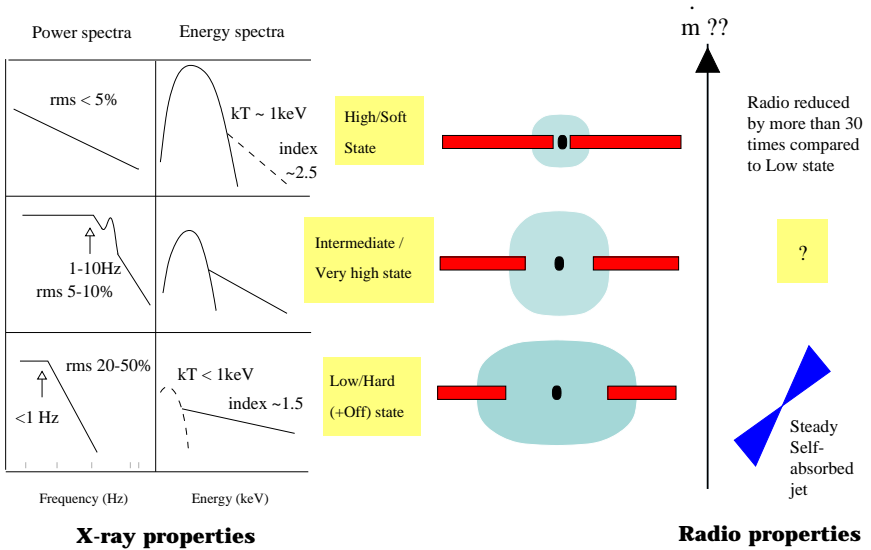
Figure 2.7: BH spectral states, as classified by their X-ray spectral and timing properties, and the physical interpretation and relation to radio emission (Fender, 2002).

50% rms and a break frequency below 1 Hz. Modeling the Low/Hard state favors an accretion disk which is truncated at some distance (typically inferred to be ~100 Schwarzschild radii) from the central black hole, around which a Comptonizing corona exists (Poutanen & Coppi, 1998). In addition, the radio emission that is observed in the hard state indicates the presence of a continuous outflow which is emitting synchrotron radiation at radio wavelength (Fender, 2001a). This X-ray properties and the model geometry of the hard state are summarized in the lower part of Fig. 2.7.

High/soft state spectra are dominated by a blackbody component with a characteristic temperature ~1 keV. At higher energies, high-state spectra show a power-law tail, softer than in the low-state (Γ ~2.2–2.7), but often extending to beyond 500 keV without an obvious turnover. The high/soft state is generally more luminous that the low/hard state, with L_X ~0.2–0.3L_{Edd}. The short-term variability associated with this emission component is generally less strong than that of the hard state, as low as a few percent relative rms amplitude. The typical soft state power spectrum shows an f^{-1} power law extending down to below 0.001 Hz. The whole soft state picture is summarized on the upper part of Fig. 2.7. In the high/soft state thermal emission from the accretion disk dominates the X-ray spec-

Table 2.1: Comparison of different X-ray states (Kong et al., 2000)

X-ray state	Energy spectrum	Power spectrum	Flux 2–10 keV[a]
'Off'	PL, $\Gamma \sim$ 1.5–2	<26% rms	< 1
LS	PL, $\Gamma \sim$ 1.5–2	$\sim$ 25–50% rms	1–13
IS	US + PL, $\Gamma \sim$ 3.5	7 % rms	15
HS	US + weak PL, $\Gamma \sim$ 2–3	few % rms	70–80
VHS	US + PL, $\Gamma \sim$ 2.5	1–15% rms, 3–10 Hz QPO	200

[a] in units of 10^{-10} erg cm^{-2} s^{-1}

PL power-law component, US ultra soft component

trum, and there is no radio emitting outflow. This state has been modeled with a multi-temperature accretion disk with an inner radius near the marginally stable orbit (Mitsuda et al., 1984; Wilms et al., 2001).

Intermediate state spectra, as the name suggests, are intermediate both in spectral shape and luminosity between the high and low spectral state. Some sources like Nova Muscae and GX 339−4, have also been observed in the very high state with luminosities close to the Eddington limit. This state has similar spectral properties as the high state, but is characterized by higher bolometric luminosity, a more prominent hard tail, stronger variability, and the presence of 3–10 Hz QPO (van der Klis, 1994). Both states show discrete, sometime multiple, radio emission ejection, which has been attributed to instabilities in the accretion disk radius and the coronal contribution. See the middle part of Fig. 2.7 for a picture of the intermediate state/very high state properties.

In addition, all transient BHXBs spend most of their time in a quiescent/off state, characterized by a very low X-ray flux. In this state the extention of the hot plasma is large, but due to the low accretion rate its luminosity is lower than in the low/hard state.

Fig 2.8 presents the basic model components in the different spectral states. The presence of a radiatively efficient corona wherein the base of the compact/jet decreases and its height increases, with increasing flux/softness, might be able to explain a number of the observed spectral-variability correlations (Nowak, Wilms & Dove, 2002).

2.2.3 Long-term variability

X-ray variability on long time scales (from days to years) has been found in many low-mass and high-mass X-ray binaries, but its origin is still an open question (e.g., Priedhorsky & Holt, 1987; Schwarzenberg-Czerny, 1992; Wijers & Pringle, 1999; Ogilvie & Dubus, 2001)

In a small but growing number of bright X-ray binaries a third (or "superorbital") period is present in addition to the usual periodicities. Clarkson et al.
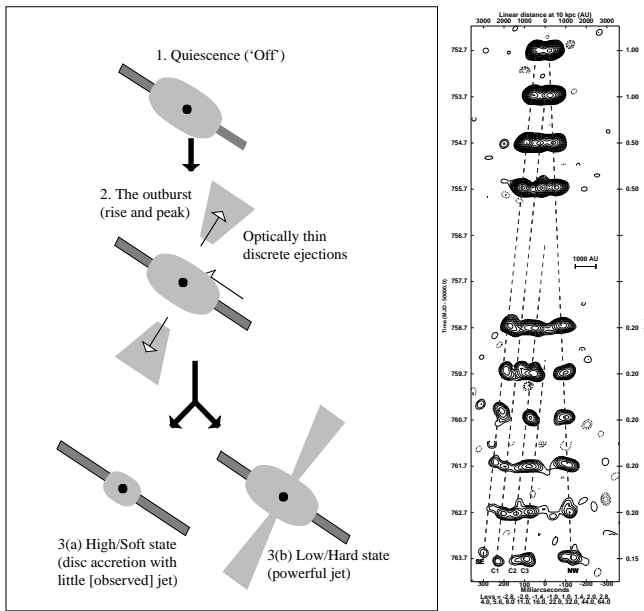
Figure 2.8: *Left*: Geometry in the different spectral States. *Right*: Resolved discrete relativistic ejection from the BH candidate GRS 1915+105 (Fender, 2001b).

(2003b) divided the superorbital variations of bright X-ray binaries into two observational classes, with clear, stable X-ray intensity variations in the ~30–60 day range forming one category (e.g., SMC X-1, Her X-1, LMC X-4), and more quasi-periodic, longer periodicities in the ~50–200 day range forming the other (e.g., Cyg X-2, GX 354−0, X 1916−053, X 1820−30). Modulations in the longer-period class are distinctly "quasi-periodic" in that even long-term monitoring datasets do not yield precise periods in their power spectra, but a broad peak, often superposed on an apparent "red noise" continuum. This superorbital periodicities from both classes are usually interpreted as due to a precessing (possibly warped) accretion disk, with differences in amplitude due to differences in inclination. The different mechanisms proposed to explain the long periods are:

1. The precession of a disk caused by forced precession of a tilted disk by the gravitational field of the companion star (Katz, 1973). In this model the disk is considered to be composed of a sequence of concentric circular rings, tilted with respect to the binary orbital plane (see Priedhorsky & Holt, 1987). The rings behave gyroscopically owing to their rapid rotation. If

they did not interact with each other, the tidal torque would cause each ring to precess retrogradely, about an axis perpendicular to the binary plane, at a rate that depends on the radius of the ring, resulting in a rapid twisting of the disk. However, a fluid disk tends to resit this by establishing an internal torque between neighboring rings. This can be arranged so that the net torque on each ring is such as to produce a single, uniform precession rate, allowing the disk to precess coherently.

2. Precession of a disk that is slaved to a misaligned companion star (Roberts, 1974). In this model the companion star is misaligned and precessing and the accretion disk (fed by the companion) will track the motion of the companion.

3. Precession of the neutron star. Trümper et al. (1986) interpreted changes in the pulse shape of Her X-1 over the 35 d cycle as evidence for free precession of the neutron star, in which the magnetic axis precesses with respect to a fixed angular-momentum vector. This precession of the neutron star may be irregular. Other models include also the coupling of the neutron star magnetic field to the inner regions of the accretion disk (Shakura et al., 1998).

4. Mass transfer feedback induced by X-ray irradiation may also generate the observed long-term periodicities (Osaki, 1985). In this model, X-ray heating of the companion star surface causes further enhancement of the mass accretion rate in a runaway instability.

5. Warped precessing disks due to radiation pressure (Petterson, 1977; Maloney, Begelman & Pringle, 1996; Wijers & Pringle, 1999; Ogilvie & Dubus, 2001). The intense radiation pressure from the central X-ray source drives the disk warp, and tidal forces lead to precession on the observed long-term time scale. The precession causes periodic obscuration of the central source, giving rise to a modulation of the X-ray flux at the precessional period. Such model, have a provision for variations in the precession period. Varying obscuration by the disk (caused by precession), should have the observational consequence, e.g., with increased absorption in the low-intensity phase, a hardening in the spectrum is expected.

6. Tilted and twisted disks due to coronal winds (Schandl & Meyer, 1994)

7. Influence of a third body (Fabian et al., 1986). The tidal torque of a massive companion star can cause the orbital plane of a close pair (the actual interacting binary) to precess.

8. State changes of the accretion disk, which are mainly due to a direct modulation of the mass accretion rate (Wilms et al., 2001).

No clear understanding of the reason behind the observed long-term periodicities stands out among all these possibilities. None of the possibilities mentioned above can explain the long-term periodicity in all the sources. In the high-mass X-ray binaries, the periodicity is generally believed to be related to disk precession, and in the low-mass X-ray binaries another possibility is some type of disk instability or modulation in the mass accretion rate related to or induced by the X-ray radiation (Meyer, 1986).

CHAPTER 3

Time series analysis methods

The search for periodic signals is common in many areas of astronomy. Classical period determination methods are based either on Fourier decomposition analysis or on folding techniques. The first type of methods uses the Fourier transform in combination with deconvolution techniques to deal with the data sampling functions (Deeming, 1975; Lomb, 1976; Scargle, 1982, 1989; Press & Rybicki, 1989; van der Klis, 1989) and will be presented in section 3.1. The second group of methods are based on the analysis of the profiles produced by folding the data over a range of trial periods (Stellingwerf, 1978; Leahy et al., 1983; Davies, 1990, 1991; Larsson, 1996). They are described in section 3.2. Fourier based techniques will, in general, successfully detect one or more combined sinusoidal signals, even if one of them has a low signal-noise ratio. However, they have difficulties in detecting the non-sinusoidal signals that might be present in the data set. On the contrary, folding methods are well suited for detecting non-sinusoidal signals but they tend to fail when two or more periods are present in the data set, especially when the signal-noise ratio is low. Note, however, that many of both kinds of methods are statistically equivalent (Schwarzenberg-Czerny, 1999). Sensitivity of the period detection does depend on the underlying theoretical signal model and the number of the parameters and on the kind of the detected signal, and not so much on the kind of period search analysis (Schwarzenberg-Czerny, 1999).

In order to interpret the local and time-dependent phenomena in the data set two-dimensional time-frequency methods are required. Examples of such methods are the dynamical power spectra (e.g., Wilms et al., 2001) described in section 3.1.2, or the Wavelet decomposition of the light curve (Grossmann, Kronland-Martinet & Morlet, 1989; Szatmáry, Vinkó & Gál, 1994; Foster, 1996) described in section 3.1.3.

Methods to examine the X-ray variability directly in the time domain are presented in section 3.3. On the one hand, the structure function analysis (SF) (Simonetti, Cordes & Heeschen, 1985; Hjellming & Narayan, 1986; Nandikotkur, Sreekumar & Carter-Lewis, 1997; Paltani et al., 1997; Hughes, Aller & Aller,

1992), section 3.3.1, provides a measure of the mean difference in the flux densities as a function of the separation in the sampling interval. On the other hand, the excess pair fraction (EPF) method (Yaqoob et al., 1997; Carson et al., 1998), section 3.3.2, characterizes the source variability on the time scale of the bin size.

Finally, an alternative analysis method in the time domain is presented in section 3.4: the linear state space model (LSSM) which is based on modeling the light curve by an autoregressive process covered by observational noise (König & Timmer, 1997).

All these methods have relatively different scopes and they are, to some extent, complementary.

3.1 Fourier methods

Detection of a periodic signal hidden in noise is frequently a goal in astronomical data analysis. Based on Fourier decomposition of the light curve, Fourier techniques are widely used in timing analysis in astronomy (van der Klis, 1989). This section introduces the mostly used Fourier methods and discusses some of the difficulties in the interpretation of these techniques. For data obtained at uniformly spaced intervals, standard methods of analysis are available, such as Fourier methods based on the Fast Fourier transform (van der Klis, 1989; Press et al., 1986), section 3.1.1. Some difficulties such as the influence of noise processes, the window function, the aliasing effect, the signal detections, and the detector dead time, are discussed in successive sections. The most commonly used method of calculating the spectrum of non-uniformly spaced data is the Lomb-Scargle periodogram analysis (Scargle, 1982; Horne & Baliunas, 1986; Press & Rybicki, 1989), section 3.1.1.4. Finally, two-dimensional time-frequency methods which give information on the possible variable spectral properties of the data are described; the dynamical power spectra (see, for example, Wilms et al., 2001), section 3.1.2, and the Wavelet map (Grossmann, Kronland-Martinet & Morlet, 1989; Szatmáry, Vinkó & Gál, 1994), section 3.1.3

3.1.1 Periodogram or Power Spectrum Density, PSD

Through a discrete Fourier transform (DFT), a light curve can be decomposed into sine wave components in the frequency domain. The jth element of the DFT of a uniformly spaced time series $x(t_k)$, which represents the count-rate, i.e. photon counts per unit of time, with a time spacing Δt at $k = 0, 1, \ldots, N_0 - 1$, where N_0

is the number of points in the time series, is defined as

$$\text{FT}_x(\omega_j) = \sum_{k=0}^{N_0-1} x(t_k)\exp(-i\omega_j t_k) \quad \text{for } j \in [-(N_0/2)\dots(N_0/2)-1] \qquad (3.1)$$

with ω_j representing the angular Fourier frequency $\omega_j = 2\pi f_j$, where $f_j = j/T$ is the normal Fourier frequency for $j = 1,\dots,N_0/2$, and where $T = N_0\Delta t$ is the total time duration of the sequence being transformed. The frequency spacing $\Delta\omega = 2\pi/T$ defines the finest frequency resolution available while maintaining completely independent Fourier amplitudes. The highest frequency for which the Fourier coefficient $\text{FT}_x(\omega_j)$ can be computed is the Nyquist frequency, $\omega_{\text{Nyquist}} = \pi/\Delta t = \pi N_0/T$. Since for most astronomical observations the data points are real numbers, the Fourier transform are symmetric about the Nyquist frequency such that $\text{FT}_x(\omega_j) = \text{FT}_x^*(\omega_j)$ (where the $*$ represents the complex conjugation).

The Fast Fourier Transform (FFT) is a computer algorithm to efficiently compute the DFT, in only $O(N_0 \lg_2 N_0)$ operations, as opposed to the $O(N_0^2)$ operations of a DFT. See, e.g., Press et al. (1986) for a description of sample computer codes of FFT algorithms.

The *periodogram* or *Power Spectrum Density* (PSD) of a time series is defined as the squared absolute value of the Fourier coefficients, multiplied by a normalization constant C

$$P_x(\omega_j) = C\,|\text{FT}_x(\omega)|^2 \quad \text{for } j \in [0\dots(N_0/2)] \qquad (3.2)$$

Due to the symmetric property of the DFT, the periodogram only needs to be defined for positive frequencies. The PSD is used to describe the variability amplitude at different frequencies. A peak with power in excess of the noise distribution power in the PSD indicates the existence of a periodic component in the light curve.

The actual relation between the PSD and the variability process occurring in the time domain is given by Parseval's theorem,

$$\frac{1}{N_0}\sum_{j=-N_0/2}^{(N_0/2)-1} FT_x(\omega_j) = \sum_{k=0}^{N_0-1} |x(t_k)|^2 \qquad (3.3)$$

which states that the integral of the PSD over the whole frequency range is equal to the variability power of the same process in the time domain. In fact, this property is the reason why the quantity $P_x(\omega_j) = C\,|\text{FT}_x(\omega)|^2$ is called *power* density.

Several normalization constants of the PSD, C, have been proposed in the X-ray
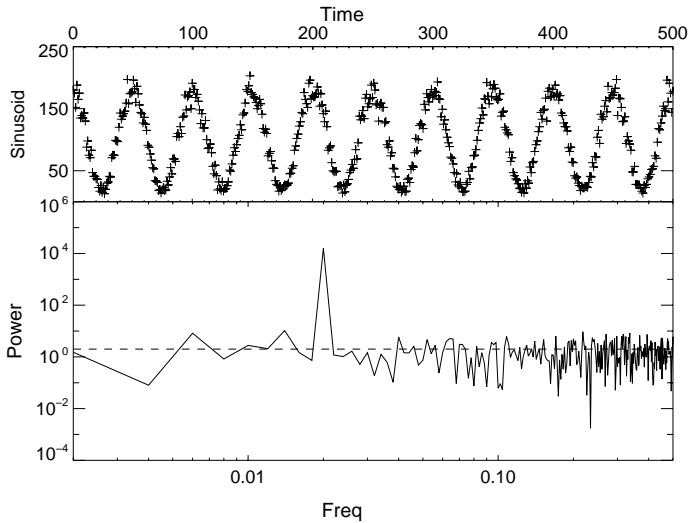
Figure 3.1: *Upper panel*: Test time series composed of one sinusoidal component with a period of 50 and amplitude of 80, plus Poisson distributed random noise. *Lower panel*: Corresponding periodogram in Leahy et al. (1983) normalization shows a clear peak at the corresponding frequency. The dashed line represents the expected power from Poisson fluctuations (see text).

astronomy literature (the notation has been taken from Wilms, 1998):

$$C = \begin{cases} C_{\text{Leahy}} = 2\Delta t^2/N_{\text{ph}} = 2\Delta t/\left(N_0 \langle x \rangle\right) \\ C_{\text{Miyamoto}} = 2\Delta t^2/(N_{\text{ph}} \langle x \rangle) = C_{\text{Leahy}}/\langle x \rangle = 2\Delta t/\left(N_0 \langle x \rangle^2\right) \\ C_{\text{Schlittgen}} = 1/N \end{cases} \tag{3.4}$$

where $N_{\text{ph}} = \sum_{j=0}^{N_0-1} x_j \Delta t$ represents the total number of photons observed, and $\langle x \rangle$ is related to the mean intensity of the source. The C_{Leahy} normalization was proposed by Leahy et al. (1983). If the statistical fluctuations in the time series are Poissonian, then the ensemble averaged power in this normalization is equal to 2 (Leahy et al., 1983; van der Klis, 1989). In the limit of large N_{ph}, P_j is distributed as a χ^2-distribution with two degrees of freedom. This normalization is suitable to derive statistical significance of the variations. C_{Miyamoto} was proposed by Miyamoto, Kimura & Kitamoto (1991). In this normalization, the periodogram in Leahy normalization is divided by the mean count-rate of the source to obtain a count-rate independent periodogram. The integrated periodogram, i.e., the area under the PSD estimated by the periodogram, defines the square of the to-

tal rms variability of the time series, i.e., the fractional amount by which the light curve is sinusoidally modulated (van der Klis, 1995; Nowak et al., 1998). This normalization is suitable to compare among time variations of different sources and also those of the same source at different occasions Miyamoto et al. (1992). $C_{\text{Schlittgen}}$ is mainly used in mathematical time series analysis (Schlittgen & Streitberg, 1995). With this normalization the periodogram depends on the count-rate and on the temporal binning of the data, therefore, absolute measurements of the power are not possible. Fig. 3.1 shows the response of the PSD in Leahy et al. (1983) normalization to a pure sinusoid plus noise signal.

When many separate observations of the same stationary random process are available, one can reduce the variance by calculating a separate periodogram for each time series and then averaging all the values of $P(\omega_k)$ at each ω_k. Or for a long time series, one can split up the original sample of data points into a number of subsamples and treat these separate parts of the original time series as independent experiments (Papadakis & Lawrence, 1993a). Another method of reducing the variance of the periodogram is to smooth, i.e., to estimate the spectral density as a weighted average of neighboring periodogram values (Papadakis & Lawrence, 1993a).

3.1.1.1   Noise processes

Despite the differences between the main types of accretion-powered X-ray sources, a remarkable feature shared by these systems is the presence of aperiodic variability in X-ray light curves. Because of its random character this kind of variability is often referred to as *noise*.

The noise variability is characterized through the study of the broad band behavior of the PSD. A *white noise* process, which represents a sequence of independent Gaussian variables, generates a flat PSD with constant power in the spectrum equal to 2 in the case of the Leahy et al. (1983) normalization. For *red noise* (also called *flicker noise*) processes, the power is decreasing toward the high frequencies, and the PSD is characterized by a power-law distribution, $P(\omega) \propto \omega^{-\alpha}$ (Press, 1978). *Shot noise* processes generate more complicated shapes of the periodogram (Lehto, 1989; Lehto, Czerny & McHardy, 1993). The simplest shot noise, where the light curve is constructed from stochastic series of independent overlapping shots with a single characteristic decay time-scale (Terrell, 1972), produces a red noise type power spectrum at high frequencies with $\alpha = 2$ which flattens to $\alpha = 0$ at low frequencies, i.e., the variability becomes white noise on long time-scales (Uttley & McHardy, 2001).

3.1.1.2 *The window function and the aliasing effect*

For a finite number of data points (equally or unequally samples) the mean value of the periodogram will be equal to the convolution of the true PSD of the stochastic process with the PSD of the sampling pattern, i.e., the *window function* (see Deeming, 1975). One result of this effect is that the observed value of the periodogram at any particular frequency includes contributions from above and below this frequency in the true PSD, the so called "spectral leakage", which complicates the interpretation of the periodogram and can result in spurious features (Deeter & Boynton, 1982). The net effect depends on the curvature of the true power spectrum, as for example with a red noise process the power in the power spectrum will be transferred from low frequencies to high frequencies.

Furthermore, the periodogram of the convolved function is reflected around the Nyquist frequency, ω_{Nyquist}. This causes features with a frequency exceeding ω_{Nyquist} by ω_j (so, located at $\omega = \omega_{\text{Nyquist}} + \omega_j$) to also appear at a frequency $\omega = \omega_{\text{Nyquist}} - \omega_j$, a phenomenon known as aliasing (see van der Klis, 1989). The value of the periodogram at each frequency ω_j is then a combination of the true power spectrum values at ω_j and its aliases , which are defined in the case of evenly spaced data as $2\omega_{\text{Nyquist}} \pm \omega_j, 4\omega_{\text{Nyquist}} \pm \omega_j, \ldots$ (Chatfield, 1989). The periodogram of a set of non-uniform data is far more complex than the spectrum of a set of uniform data, because there are no frequency regions, as there are in the analysis of equally spaced data, in which a period is unambiguously defined. Each true peak in the spectrum gives rise to a number of other peaks (aliases) of various heights, distributed throughout the spectrum.

3.1.1.3 *Signal detection and the effect of the detector dead time*

Astronomical observations rely upon photon-counting instruments. Therefore, measurement errors are often dominated by the statistical uncertainties originating from the Poisson fluctuations of the counts. This translates into a white noise power spectrum component. Any intrinsic variability of the source, resulting either from periodic signal(s) or from noise, must possess significant power above the count statistics white noise component in order to be detected.

Furthermore, time series analysis in X-ray astronomy is complicated by the effects of detector dead time, time during which the detector, when occupied processing an event, cannot process another. This can cause significant departures of power spectra from those with simple Poisson statistics. Several attempts have been made to quantify the effects of detector dead time. A simulation provided an elegant and rather accurate empirical expression for the effect and correction of instrumental dead time on the PSD (van der Klis, 1989). Dead time effects presents in the *XMM*/EPIC pn-CCD has been shown through simulations by Kuster et al.

(1999). Zhang et al. (1995) presents analytical formulae for the power spectra of paralyzable and nonparalyzable dead times. In the paralyzable case, every incident event causes dead time, even if it is no detected, making the dead time "cumulative". In the nonparalyzable case, only a detected event causes the detector to be dead for a period of time. Analytic corrections for dead time effects in the *RXTE*/PCA instrument has been described by Zhang et al. (1996) and Pottschmidt (2002).

3.1.1.4   *Period analysis of unevenly sampled time series*

Because of the nature of observational astronomy, the data to be analyzed are frequently unevenly spaced in time and interrupted by data gaps. This problem affects mainly on long data sets (over days to years), where it is no possible to measured the data continuously due to several effects, e.g., telemetry dropouts, passage through the South Atlantic Anomaly, Earth occultations, or other electronic problems. The PSD method described in section 3.1.1 can only used in the case of evenly time series without gaps. A modified periodogram first presented by Lomb (1976) and formally defined by Scargle (1982) replaces equation 3.2 in the case of unevenly sampled data. The implementation of the method has been discussed by Horne & Baliunas (1986), and is often used in different astronomical applications. For a time series $x(t_i)$ where $i = 0, 1, \ldots, N_0 - 1$, the *modified Lomb-Scargle periodogram* is defined (Scargle, 1982, eq. 10) as

$$P_x(\omega) = \frac{1}{2\sigma^2} \left\{ \frac{\left[\sum_{k=0}^{N_0-1} (\tilde{x}_k) \cos \omega(t_k - \tau) \right]^2}{\sum_{k=0}^{N_0-1} \cos^2 \omega(t_k - \tau)} + \frac{\left[\sum_{k=0}^{N_0-1} (\tilde{x}_k) \sin \omega(t_k - \tau) \right]^2}{\sum_{k=0}^{N_0-1} \sin^2 \omega(t_k - \tau)} \right\} \quad (3.5)$$

where $\tilde{x}_k = x_k - \langle x \rangle$, and $\langle x \rangle$ and σ are the data's mean and variance respectively, ω is the frequency at which the power is computed, and τ the time-offset given by

$$\tan(2\omega\tau) = \frac{\sum_{k=0}^{N_0-1} \sin 2\omega t_k}{\sum_{k=0}^{N_0-1} \cos 2\omega t_k} \quad (3.6)$$

The total variance of the data has been taken as the normalization factor of the periodogram (see Horne & Baliunas, 1986). A fast evaluation of the Lomb-Scargle algorithm reducing the order of operations from $10^2 N_0$ by a factor of $\log N_0$ was implemented by Press & Rybicki (1989). See an example in Fig. 3.2

The Lomb-Scargle periodogram has several useful properties which the usual discrete Fourier transform does not have. For example, the inclusion of the τ term makes the periodogram time invariant, i.e., replacing t_i by $t_i - K$, where K is a constant, does not change $P_x(\omega)$. Furthermore, $P_x(\omega)$ is defined so that if the
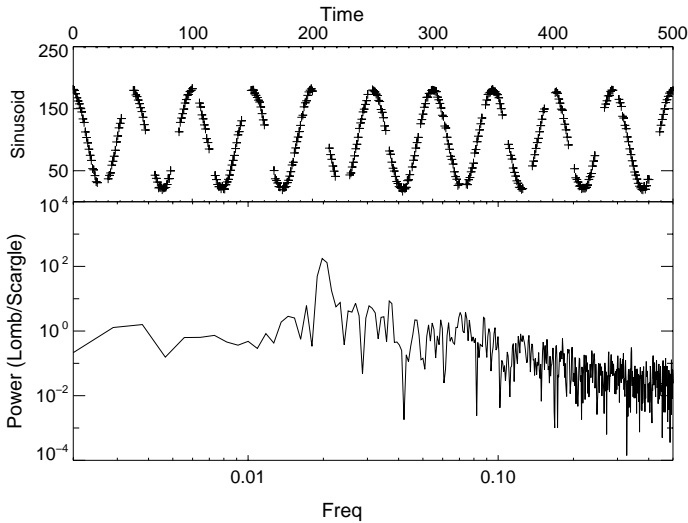
Figure 3.2: *Upper panel*: Same time series as in Fig. 3.1 with some gaps introduced randomly. *Lower panel*: Corresponding Lomb-Scargle periodogram.

signal $x(t_i)$ is purely normally (Gaussian) distributed noise (i.e., white noise), then the power in $P_x(\omega)$ follows an exponential probability distribution:

$$\Pr(Z > z) = 1 - (1 - \exp(-z))^{N_i} \tag{3.7}$$

where N_i is the number of statistically independent frequencies in the periodogram (Horne & Baliunas, 1986, eq. 13),

$$N_i = -6.362 + 1.193N_0 + 0.00098N_0^2 \tag{3.8}$$

This exponential distribution provides an estimate of the probability that a given peak is a true signal, or whether it is the result of randomly distributed white noise. See Fig. 3.1. Such a statistical estimation of a peak in the periodogram is only suitable in the case of a purely white noise dominated signal. With the presence of "colored" continuum PSD components resulting from source noises, a common approach to determine the significance of a peak in the periodogram is by performing Monte Carlo simulations (Horne & Baliunas, 1986). This procedure will be presented in detail in chapter. 4
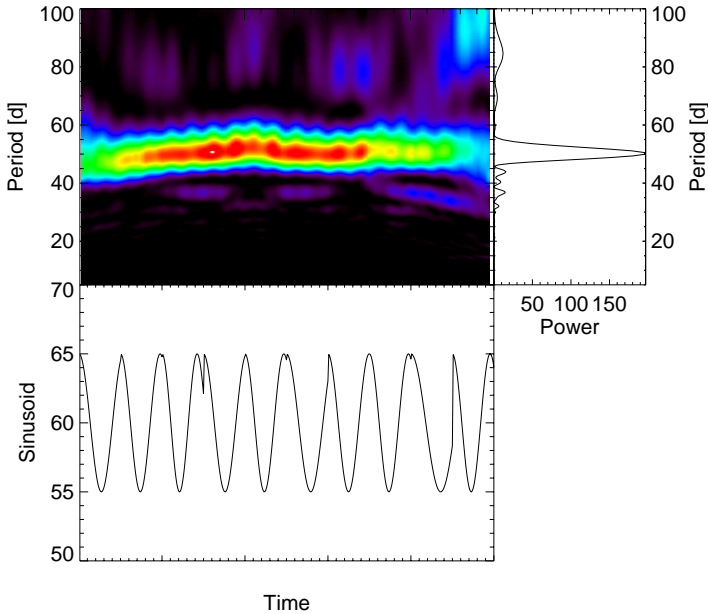
Figure 3.3: *Upper left*: Dynamical power spectra of a test time series composed of one sinusoidal component with random period change from cycle to cycle and a period mean value of 50. *Upper right*: Lomb-Scargle periodogram for the test time series. *Lower left*: Sinusoidal test time series.

3.1.2   *Dynamical power spectra*

To investigate the time evolution of the power spectrum astronomers usually compute the *dynamical power spectra* (sometimes called *spectrogram*, or *dynamical periodogram*) from the time series data (see, for example, Wilms et al., 2001). To compute the dynamical power spectra, individual power spectra, each covering a time interval with M elements ($M \ll N_0$) and then successively shifted through the data with a desired step size, are determined. For each of these slices the Lomb-Scargle periodogram is computed for always the same period range. To ensure that the Lomb-Scargle periodograms are comparable, a normalization is

used such that

$$\frac{\sigma^2}{\mu} = \int_{w_{\min}}^{w_{\max}} \mathrm{PSD}(w)\, dw \qquad (3.9)$$

where $w_{\min}$ and $w_{\max}$ are the minimum and maximum frequency for which the Lomb-Scargle periodogram is computed, σ^2 is the variance, and μ the mean count rate of the slice. The resulting periodogram is then color coded and plotted versus time, with each periodogram being displayed at the mid-time of the light curve for which is was computed, see Fig. 3.3 for an example.

In order to extend the dynamical periodogram to the full length of all the time covered by the data, Gaussianly distributed random date spanning over an interval of $M/2$ elements before and after the light curve are artificially added. Each of these fake data set is chosen to have the same mean and variance of the first and last interval with M elements, respectively, of the actual measured data set.

Although the individual Lomb-Scargle periodograms are obviously not statistically independent, this approach is useful in revealing the long-term trends of the light curve.

3.1.3 Wavelet map

Wavelet decomposition is increasingly being used for astronomical signal processing, in the study of the variability characteristics of a source. The method is based on the decomposition of the signal into multiple channels based on their local frequency content. The Wavelet transform is an intermediate representation between the Fourier and the temporal one.

The Wavelet transform (Grossmann, Kronland-Martinet & Morlet, 1989) is defined as the convolution of the signal of interest with an analysis function, a so-called Wavelet analysis, or shortly, Wavelet. The Wavelet is localized in time and in frequency which therefore allows a local or time-frequency analysis of the signal. A Wavelet coefficient depends on two quantities; the width of the Wavelet $1/w$ and its position τ in the time interval.

The general definition of the Wavelet transform of a signal $x(t)$ is (e. g., Grossmann, Kronland-Martinet & Morlet, 1989)

$$W(w, \tau) = \sqrt{w} \int_{-\infty}^{\infty} x(t) g^*[w(t - \tau)]\, dt \qquad (3.10)$$

where w is the frequency, τ the time-shift, $g^*[w(t-\tau)]$ is the kernel of the transform (the so-called analyzing Wavelet or mother Wavelet; the asterisk means complex conjugate). The actual value of the Wavelet transform at a given (w, τ) point is high if the signal $x(t)$ contains a cycle length of $P = 1/w$ at the time τ, and low otherwise.
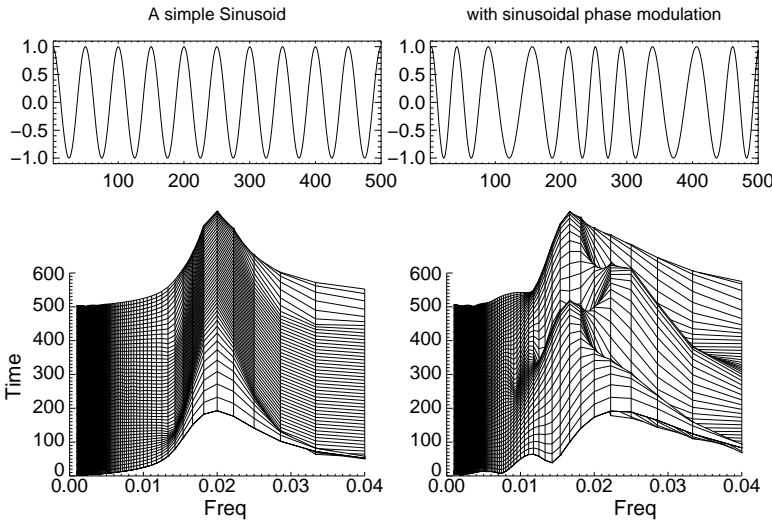
Figure 3.4: Wavelet map of a test time series composed of one sinusoidal component with a period of 50 on the left, and of the same test time series with sinusoidal phase modulation on the right. The upper panels represent the light curves, and the lower panels the corresponding contour Wavelet maps.

A simple Gaussian, the so-called Morlet Wavelet, will be adopted to the kernel function (Szatmáry, Vinkó & Gál, 1994):

$$g^*(x) = \exp\left(-icx - \frac{1}{2}x^2\right) \tag{3.11}$$

where c is the scaling factor which controls the time versus frequency resolution. Usually $c = 2\pi$ (Szatmáry, Vinkó & Gál, 1994). See Scargle (1993) for the application of other types of Wavelet.

The discrete realization of the continuous Wavelet transform defined by Eq. 3.10 inserting Eq. 3.11 can be expressed as

$$W(w, \tau) = w^{1/2}\left[S^2 + C^2\right]^{1/2} \tag{3.12}$$

where

$$S(w, \tau) = \sum_{j=0}^{N_0-1} x(t_j) \sin[2\pi w(t_j - \tau)]e^{-\frac{1}{2}w^2(t_j-\tau)^2} \tag{3.13}$$

and

$$C(w, \tau) = \sum_{j=0}^{N_0-1} x(t_j) \cos[2\pi w(t_j - \tau)] e^{-\frac{1}{2}w^2(t_j-\tau)^2} \tag{3.14}$$

The absolute value of the Wavelet coefficients given by Eq. 3.12 will be referred to as *Wavelet map*. Fig. 3.4 shows two test light curves and the respective Wavelet maps. The one on the left side represents a stable and perfectly sampled sinusoidal signal. In the second one on the right side, a cyclic phase modulation has been introduced to the data set. See Foster (1996) for the response of the Wavelet transform in the presence of unevenly sampled time series. The Wavelet map can also be represented as a color scaled coded diagram, similar to the dynamical periodogram (see for example Fig. 6.15).

3.2 Folding methods

In search for periodicities, additionally to the Fourier methods, a set of techniques based on folding the data modulo a trial period and then grouping the observations according to the phase, are also used. In this technique, a statistic is used to test the resulting profile for uniformity. The folding techniques can be further subdivided into those which examine the variance within a phase bin, i.e. phase dispersion minimization (PDM, e.g., Stellingwerf, 1978), and those which test for uniformity of phase bin means, referred to as epoch-folding (e.g., Leahy et al., 1983)

The technique of folding data to search for periods is particularly useful with X-ray astronomical observations due to the higher sensitivity to non-sinusoidal modulations, which is a characteristic of many X-ray pulsars. Additionally, folding methods provide a useful approach to handling gaps or irregular sampling data sets.

3.2.1 Phase Dispersion Minimization, PDM

Following the notation of Davies (1990), a time series of N_0 observations, x_i ($i = 0, 1, \ldots, N_0 - 1$), folded at a trial period into M phase bins, is considered. The phase length will then defined as $\Delta\phi = P/M$, with P the correspondent trial period. The trial periods, P, are ranging from $P_{\min} = 2T/i_1$ to $P_{\max} = 2T/i_2$, with $i \in [i_2, i_2 + 1, \ldots, i_1]$ and T the total length (including gaps) of the data set. Thus, the frequency spacing is $1/2T$.

Let x_{kj} represent the kth observation in the jth phase bin, and let n_j be the total number of data points in the jth phase bin. If $\langle x \rangle$ is the sample mean, then $\hat{\sigma}^2$ is
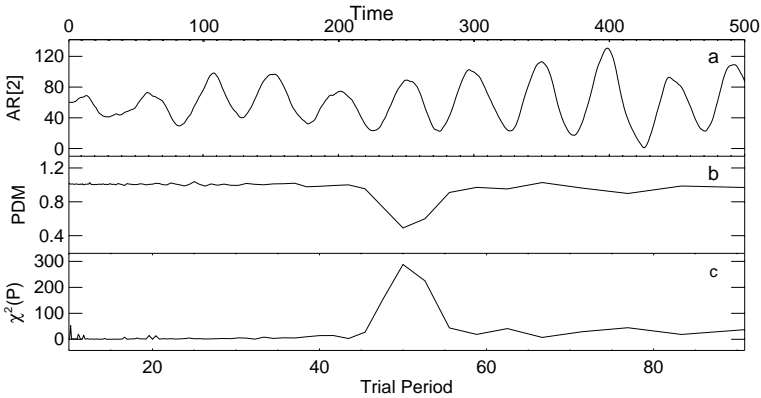
Figure 3.5: *(a)* Test time series of an AR process of order 2, with *P*=50 and $\tau = 100$ (see section 3.4), *(b)* PDM diagram, *(c)* Epoch-folding diagram. Both diagrams show a broad peak around *P*.

the sample variance according to the usual definition

$$\hat{\sigma}^2 = \frac{1}{N_0 - 1} \sum_{i=0}^{N_0-1} (x_i - \langle x \rangle)^2 \tag{3.15}$$

Let $\langle x \rangle_j$ and s_j^2 be the mean and sample variance in the jth phase bin, respectively. A null hypothesis, $\mathcal{H}_0$, based on uniformity across phase will be investigated. $\mathcal{H}_0$ is defined taking the model $x_{kj} = \mu_j + \epsilon_{kj}$, where μ_j is the true mean of the jth phase bin, and ϵ_{ik} represents the measurement errors, which are assumed to be a set of independent random variables with identical mean and variance. The null hypothesis then states that all the μ_j are identical (independent of j), while rejection of $\mathcal{H}_0$ usually implies that the scatter of $\langle x \rangle_j$ is too great to be consistent with a uniform μ_j. In other words, μ_j varies with phase, and this is generally taken to be strong evidence for a periodicity in the data.

Under these assumptions, and following Stellingwerf (1978), the phase dispersion minimization (PDM) test statistic can be written as

$$\Theta^2(P) = s^2/\hat{\sigma}^2 = \left(\frac{1}{\hat{\sigma}^2}\right) \frac{\sum_{j=1}^{M} \left(n_j - 1\right) s_j^2}{N_0 - M} \tag{3.16}$$

for each trial period $P \in [P_{\min}, \dots P_{\max}]$. According to Stellingwerf (1978) $\Theta^2(P)$ should have an F distribution with $(N_0 - M)$ and $(N_0 - 1)$ degrees of freedom. If a periodicity is present, then Θ^2 will be anomalously small and the null hypothesis can be rejected. See Fig. 3.5.b for an example.

3.2.2 Epoch-folding

Considering the same assumptions, and following Leahy et al. (1983) the epoch-folding statistic is defined as

$$\chi^2(P) = \sum_{j=1}^{M} \frac{\left(\langle x \rangle_j - \langle x \rangle\right)^2}{\sigma_j^2} \tag{3.17}$$

for each trial period $P \in [P_{\min}, \dots P_{\max}]$. The term σ_j^2 is the population variance of $\langle x \rangle_j$ (see Bevington & Robinson, 1992, for a definition of population variance and sample variance). Using the assumptions of the null hypothesis this can be taken as $\sigma_j^2 \approx \hat{\sigma}^2 / n_j$ (Davies, 1990), and therefore the equation 3.17 can be rewritten as

$$\chi^2(P) = \frac{1}{\hat{\sigma}^2} \sum_{j=1}^{M} n_j \left(\langle x \rangle_j - \langle x \rangle\right)^2 \tag{3.18}$$

The test statistic $\chi^2(P)$ will have approximately a χ^2 distribution with $M-1$ degrees of freedom. A high $\chi^2(P)$ value ($\gg M-1$) will signal the presence of a periodicity for which the significance can be estimated from the $\chi^2_{(M-1)}$ distribution (Larsson, 1996; Schwarzenberg-Czerny, 1997). See Fig. 3.5.c for an example of the epoch-folding analysis.

Davies (1990, 1991) showed that these two folding techniques are essentially the same. Therefore, I will only use the epoch-folding techniques in the search of periodicities in the rest of this Thesis.

3.3 Time domain methods

3.3.1 Structure function analysis, SF

The *structure function* (SF) introduced by Simonetti, Cordes & Heeschen (1985), is a tool commonly used in time-series analysis in astronomy (e.g., Bregman et al., 1988; Hughes, Aller & Aller, 1992; Lainela & Valtaoja, 1993; Nandikotkur, Sreekumar & Carter-Lewis, 1997; Paltani, Courvoisier & Walter, 1998; Kawaguchi & Mineshige, 1998). It provides a method of quantifying time variability without the problems of windowing, aliasing, etc., that are encountered in the traditional Fourier analysis techniques and therefore is a good tool for time series with data gaps.

The general definition of structure functions are given by Simonetti, Cordes & Heeschen (1985). In the case of a finite evenly sampled discrete time series $x(t_i)$,

with $t_i = i \cdot \Delta t$ for $i = 0, \ldots, N_0 - 1$, the first order structure function (often simply referred to as the "structure function" or "SF") is estimated using the expression:

$$\mathrm{SF}_x(\tau) = \frac{1}{N(\tau)} \sum_{i=0}^{N_0-1} [x(t_i + \tau) - x(t_i)]^2 \qquad (3.19)$$

which represents the average take over all measurements separated by lag τ (i.e., $x(t_i)$ and $x(t_i + \tau)$) with $N(\tau)$ being the number of such pairs. The SF expresses a curve of growth of variability with time-lag, τ (Nandikotkur, Sreekumar & Carter-Lewis, 1997).

To approximate this relationship in the case of an unevenly sampled light curve, where the time series is given by $x(t_j)$ with t_j arbitrary for $j = 1, \ldots, N_0$, the SF is estimated in a bin of width δ for a lag τ using the relation:

$$\mathrm{SF}_x(\tau, \delta) = \frac{1}{N(\tau, \delta)} \sum_{(i,j) \backslash \tau - \delta/2 < t_j - t_i < \tau + \delta/2} [x(t_j) - x(t_i)]^2 \qquad (3.20)$$

where $N(\tau, \delta)$ is the number of pairs $[t_i, t_j]$ that satisfy the relationship $\tau - \delta/2 < t_j - t_i < \tau + \delta/2$ (see Paltani et al., 1997).

For a non-variable object, the SF is constant and gives an estimate of the standard deviation of the white noise introduced by the measurement. For an "ideal" process of a variable object, the characteristic shape of the SF versus the time-lag, τ, consists of three well differentiated parts, as can be seen in Fig. 3.6: (i) a plateau at small time-lags, with a value corresponding to twice the variance of the measurement noise ($2\sigma_{\mathrm{noise}}^2$), (ii) a plateau at large time lags (longer than the longest correlation time scale called T_{max}) , with a value of twice the variance of the fluctuations ($2\sigma_{\mathrm{signal}}^2$), and (iii) a intermediate monotonic rise between the two plateaus which exhibits a power-law, whose dependence can be expressed as $\mathrm{SF}_x(\tau) \propto \tau^\beta$. The parameter β is an indication of the nature of the memory associated with the processes and the distribution of power across the frequencies. If $0 < \beta < 1$, then the process has a short memory and if $1 < \beta < 2$, then the process has a long memory. $\beta = 1$ implies that the observations are uncorrelated. The slope of $[\log(SF_x(\tau)) - \log(\tau)]$ plot gives the value of β. Its logarithmic slope depends on the nature of the intrinsic variation of the source. The other important parameter in the structure function analysis is the maximum time scale T_{max}, which gives the time-lag when the structure function reaches the upper plateau. It can be interpreted in two ways: it is the maximum time scale of correlated behavior or alternatively the minimum time scale in the distribution of response times (see Hughes, Aller & Aller, 1992, for details).

From an ideally structure function (Fig. 3.6) the characteristic time scales can be determined (from the time-lag at which the curve flattens) and some information about the nature of the intrinsic variation of the source (from the slope of
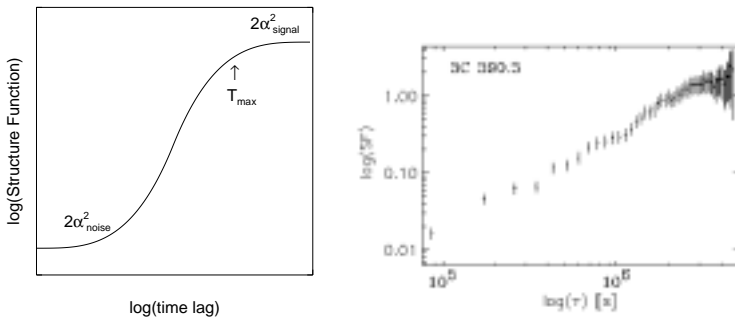
Figure 3.6: *Left panel*: Sketch of the "ideal" SF for a time series with measurement noise. *Right panel*: SF of the AGN 3C 390.3, which resembles the behavior expected from an ideal stationary random process with a smooth increase until a plateau state is reached at ~25–30 days (Gliozzi, Sambruna & Eracleous, 2003, Fig. 2).

the "power-law" portions of the curves). These quantities can be compared from source to source or from one class of sources to another. To facilitate the estimate of when the long time-lag occurs, it is advisable to normalize the structure function with $\sigma^2_{\mathrm{signal}}$ (Hughes, Aller & Aller, 1992).

However, in some cases the structure function deviates quite significantly from the ideal. Note that the structure function at large lags is not a good representation of the sample because of the few number of pairs that contribute the computation. At long time-lags, the structure function will therefore often undergo a rapid rise, fall, or oscillation. The SF should not be considered to be well defined there, and only the region at shorter time-lags should be used (Hughes, Aller & Aller, 1992). An empirical rule can be used in the calculation of the structure function taking $N(\tau) \geq$ "minimum" and $\tau \leq T/2$, where T is the duration of observation (Nandikotkur, Sreekumar & Carter-Lewis, 1997).

Some other types of behavior exhibited are (Hughes, Aller & Aller, 1992): (i) Sources displaying no plateau at long time-lags; the characteristic time scale might be longer than is detectable by the current time base of the data, and the longest time-lag available sets a lower limit on the characteristic time. (ii) Sources with a third plateau at intermediate time-lag; the existence of this plateau might indicate the interplay of two different processes that give rise to the observed variability. (iii) Sources with a very irregular structure function; in general, variations dominated by one or a few large outbursts, or variations that are more or less periodic, will have such behavior reflected in the structure function. A periodicity or

pseudo-periodicity in the flux will show up as an oscillation in the structure function whereas a significant global rising trend in the dataset shows up as a sharp rise in the structure function at larger lags.

The structure function and power spectrum are both related measures of the distribution of power with time scale and gives similar information, but the structure function has advantages if the data are non-periodic or data points are unevenly distributed in the time domain. A simple correspondence between power laws in the Fourier analysis and the structure function analysis can be established. Observed PSD generally show a power-law decline which is proportional to $f^{-\alpha}$. Generally, the SF has a power-law index, β, which is relates to α by $\alpha = \beta + 1$ in the limit of infinite and continuous data points (Hughes, Aller & Aller, 1992). On the other hand, when we analyze long light curves, we find one critical frequency (f_{break}) under which the PSD flattens and one time scale T_{max} over which the SF flattens. These frequency and time scale are related to each other by $T_{\text{max}} \approx (2\pi f_{\text{break}})^{-1}$.

3.3.2   Excess pair fraction, EPF

The Excess Pair Fraction (EPF) method is another method of analysing time series with data gaps for variability time scales, and has been introduced by Yaqoob et al. (1997) (the following description is based on this publication). In this method, the time-series is binned at a bin-width δ and the number of counts in each bin is found. The EPF is defined as a function of the bin size δ. For each bin size we count the total number of adjacent pairs of *nonempty* bins and compute the fraction of those pairs in which the number of counts in the two bins differ by at least the sum of the square roots of the counts. In other words, if we observe C_i counts in the first bin of a pair, for the second bin to contribute to the fraction it must have C_{i+1} counts which satisfy the condition

$$|C_i - C_{i+1}| \geq \alpha \left(\sqrt{C_i} + \sqrt{C_{i+1}} \right) \tag{3.21}$$

where C_i is the number of counts in the ith bin and α is usually taken to be 1 (Carson et al., 1998). This has the solution that C_{i+1} must *not* lie inside the range $1 + C_i \pm 2\sqrt{C_i}$. The second bin is used as the first bin of the next pair tested and so on. The resulting fraction is EPF(δ). For a given δ, EPF(δ) is fundamentally a function of the total number of counts per bin. The error bars are obtained from the square root of the number of bin pairs contributing to EPF(δ) divided by the total number of bin pairs tested.

This definition of EPF is equivalent to saying that in the Gaussian limit, the counts in each bin of a pair must be separated by at least the sum of their standard deviations. The method allows the measurement of bin-to-bin variability within
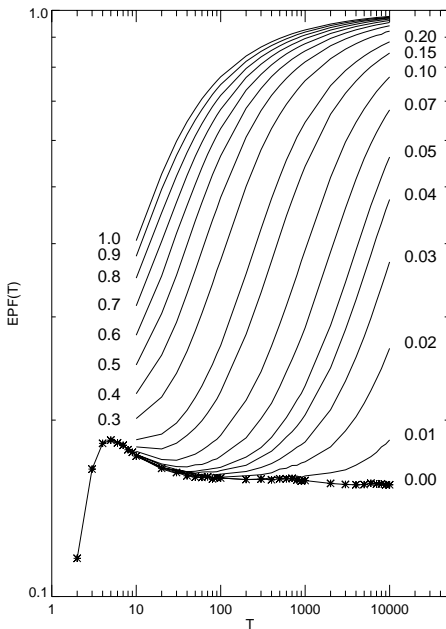
Figure 3.7: Excess pair fraction, EPF(T), calculated from simulated Poisson distributed time series with mean count rate of $1s^{-1}$ using 10^6 bin pairs (Yaqoob et al., 1997). For each simulation, the mean number of counts in each bin is $T(1 + f\eta)$, where η is a uniform random deviate between -1 and $+1$ and f represents a fractional variability parameter, i.e., the maximum bin-to-bin fluctuation in the mean count rate. The curves are shown for several values of f in the range 0.0–1.0 (a value of 0.0 corresponds to a constant source).

a time series. For example, if a source showed significant variations on a δ_0 time scale but not longer term trends, then EPF(δ_0) would be larger than EPF(δ) for $\delta > \delta_0$. Fig. 3.7 shows the EPF of several simulations of Poisson processes with different bin-to-bin variations. For a constant source, EPF is almost constant. As shown in this figure, EPF can be extremely sensitive to variability. Fig. 3.8 shows on the left side two realistic simulations of EPF, one for a pure constant source and one for a constant source with sinusoidal modulation. Note that the periodicity is also present in the EPF, having a minima at times equal to the period and its harmonics. On the right side of Fig. 3.8 a real example of an astronomical light curve is presented. Both examples have been taken from Yaqoob et al. (1997).

It is possible to fit the EPF with a power-law model like $w \propto \delta^\Gamma$. Note that Γ is related to the power-law index of the power spectrum, α, by $\Gamma = -(1 + \alpha)$.

The statistical significance of any intrinsic variability within time series with data gaps can be calculated by comparing the calculated EPF(δ) with the EPF(δ) obtained from a simulated, constant source with Poissonian fluctuations with the same mean count rate as the original source. In deriving the relation between Poisson source EPF curve, the counts in each of the 10^6 bin pairs used are taken from a Poisson distribution, and a normalized count rate of $1\,s^{-1}$ is used. A Poisson
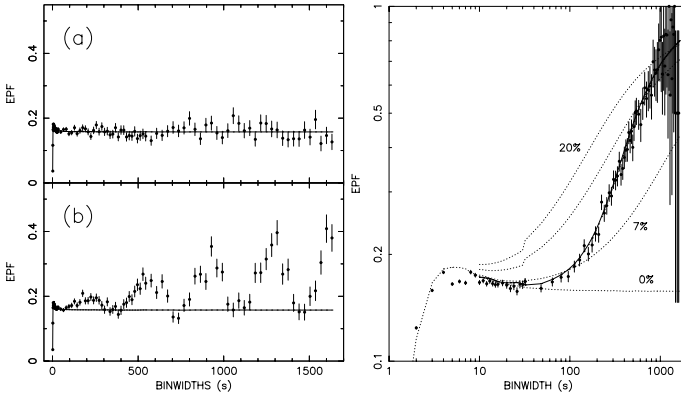
Figure 3.8: *Left panel*: Excess pair fraction, EPF(δ), calculated from simulations of a source with mean count rate 1.0 counts s^{-1}. *(a)* Case for a constant source. *(b)* Same source with a 3% sinusoidal modulation and a period of 367 s (Yaqoob et al., 1997, Fig. 2). *Right panel*: EPF(δ) calculated from an *ASCA* observation of MCG–6–30–15 taken in 1994 July. The dotted lines show the predicted EPF (see Fig. 3.7) for $f = 0\%$ (constant source), 7%, and 20%, where f is the maximum bin-to-bin variation in the count rate of the source (Yaqoob et al., 1997, , Fig. 4).

constant source tends to a constant value of the EPF in the limit of large statistics (a theoretical value of 0.159 was found by Carson et al., 1998). Direct comparison of this curve with real data simply requires dividing this Poisson curve by the appropriate real mean count rate. If the background noise were non-Poissonian and we wished to attach statistical significances to any variability in the signal, we would have to replace the EPF curve described above with an EPF curve that mimics the behavior of the background.

The maximum theoretical bin size which can be tested for variability is $T/2$, with T the total length of the time series. Spurious variability due to data binning is eliminated by rejecting bins containing gaps (Yaqoob et al., 1997; Carson et al., 1998). Due to the nature of the data analyzed in this work, the number of the selected bins are very small, making this method not suitable for our analysis purposes. Therefore, it will not be used in the rest of this thesis.

3.4   *Modeling with autoregressive processes*

An alternative approach to characterize the temporal behavior of the astronomical sources is the description of the observed time series using stochastic models

directly in the time domain. This class of method are based on autoregressive processes (AR) which were first introduced by Yule (1927) and have been able to reproduce a wide variety of observed temporal phenomena (e.g., Scargle, 1981). They are based on the assumptions that a given discrete time series $x(t)$ can be considered as a sequence of correlated random variables. The AR model expresses the temporal correlations of the time series in terms of a linear function of its past values plus a noise term. The fact that $x(t)$ has a regression on its own past terms gives rise to the terminology *autoregressive process*. A time series is thus a realization of the stochastic process or, more precisely, the observation of a realization of the process during a finite time interval. Actual physical processes can often be well represented by an AR model with a small number of parameters defining the stochastic differential equations of the system dynamics (Scargle, 1981).

An AR process of order p (AR[p]) is defined by:

$$x(t_j) = \sum_{i=1}^{p} a_i x(t_j - i \cdot \Delta t) + \epsilon(t_j), \quad \epsilon(t_j) \propto N(0, \sigma_\epsilon^2) \tag{3.22}$$

where the time series $x(t_j)$ is sampled at discrete times t_j with time resolution Δt, and the noise component $\epsilon(t)$ is a Gaussian random variable with mean 0 and variance σ_ϵ^2. In an AR time series, for each t_j the value of the random variable $x(t_j)$ is correlated with the values of the process at earlier times. This correlation is decreasing with increasing time differences between two elements of the time series.

With an AR fit describing the time series dynamics, the temporal correlation can be expressed by a stochastic superposition of different relaxators (with relaxation times τ) by damped oscillators (with relaxation times τ and periods P) or their superposition depending on the order p of the AR[p] process (Honerkamp, 1994) . These temporal correlations are characterized by the dynamical parameters a_i. This parameter values have to be restricted for the process to be stationary (Honerkamp, 1994). For a first order process this means $|a_1| < 1$, for a second order process: $\left| a_1 \pm \sqrt{a_1^2 + 4a_2^2} \right| < 2$. The relaxation time τ of the system is determined for an AR[1] process from a_1 by

$$\tau = -\frac{1}{\log \|a_1\|} \tag{3.23}$$

In the case of a damped oscillator for an AR[2] process the parameters, the period P and the relaxation time τ, respectively, are related by:

$$a_1 = 2 \cos\left(\frac{2\pi}{P}\right) e^{-1/\tau} \tag{3.24a}$$

and

$$a_2 = -e^{-2/\tau} \tag{3.24b}$$

See the upper panel in Fig. 3.5 for an example of an AR[2] process.

For a given time series the parameters a_i can be estimated, e.g., by the Durbin-Levinson- or Burg-algorithm (Honerkamp, 1994). By statistical testing it is possible to infer whether a model is compatible with the data.

In astronomical observations the observational noise which is caused by a measurement (i.e., photon statistic, particle background) has to be considered because it disturbs the temporal structures of the system-light curve. A generalization of the AR processes, which takes observational noise into account, is the linear state space model (LSSM).

3.4.1   Linear state space model, LSSM

LSSM analysis is a mathematical method to model stochastic time series in the time space which generalizes the AR processes by explicitly modeling observational noise (Gantert, 1989). Several applications to astronomical data can be found in the literature (König & Timmer, 1997; Pottschmidt et al., 1998; Band, König & Chernenko, 1998).

A LSSM is defined with two equations; the system or dynamical equation for the intrinsic system light curve (Eq. 3.25a) and the observation equation for the measured light curve (Eq. 3.25b). The latter describes the observed light curve $y(t_j)$ for $j = 1, \ldots, N_0$ by explicitly considering the influence of the observational noise $\eta(t_j)$ on the system light curve. Thus an LSSM is expressed through

$$\vec{x}(t_j) = A \cdot \vec{x}(t)_{j-1} + \vec{\epsilon}(t_j) \quad \vec{\epsilon}(t_j) \sim N(0, Q) \tag{3.25a}$$

$$\vec{y}(t_j) = C \cdot \vec{x}(t_j) + \vec{\eta}(t_j) \quad \vec{\eta}(t_j) \sim N(0, R) \tag{3.25b}$$

This definition is a multivariate description, which means that the $AR[p]$ process is given as a p-dimensional AR[p] process of order one, with a $p \times p$ matrix A that determines the dynamics. This matrix contains the dynamical parameters a_i, $i = 1, \ldots, p$, in the first column. The terms $\vec{\epsilon}(t_j)$ and $\vec{\eta}(t_j)$ represent the Poissonian dynamical noise with covariance matrix Q and the Poissonian observational noise with variance R respectively. The observation $\vec{y}(t_j)$ is formulated as a linear combination of the random vector $\vec{x}(t_j)$ and $\vec{\eta}(t_j)$ for $j = 1, \ldots, N_0$. The matrix C relates to the unobservable dynamics to the observation. Since astronomical observations are one dimensional time series, the matrix C is represented by the vector $\vec{C} = (c, 0, \ldots, 0)$.
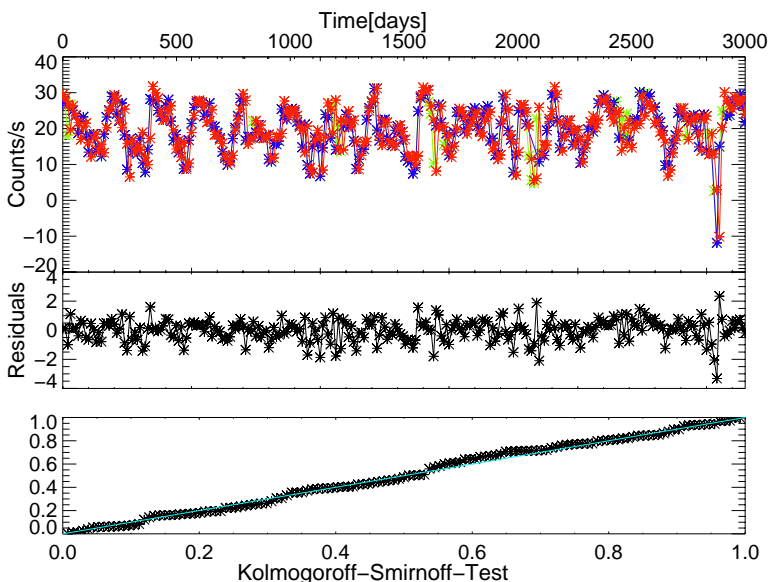
Figure 3.9: *Upper panel*: *RXTE*/ASM X-ray light curve of the source 4U 1820-30 (blue points), with gaps filled with white noise (green points), and the best LSSM fit which corresponds to an AR[2] process (red points). *Middle panel*: Residuals between the estimated light curve $y(t_j)$ and the observed one $x(t_j)$. *Lower panel*: Kolmogorov-Smirnov test which compares the residuals with the white noise null hypothesis.

In the case of an AR[2] process, the corresponding LSSM[2] model is defined by

$$\begin{pmatrix} x_1(t_j) \\ x_2(t_j) \end{pmatrix} = \begin{pmatrix} a_1 & 1 \\ a_2 & 0 \end{pmatrix} \begin{pmatrix} x_1(t_{j-1}) \\ x_2(t_{j-1}) \end{pmatrix} + \begin{pmatrix} \epsilon(t_j) \\ 0 \end{pmatrix} \quad (3.26a)$$

$$\begin{pmatrix} y(t_j) \\ 0 \end{pmatrix} = \begin{pmatrix} c & 0 \\ 0 & 0 \end{pmatrix} \begin{pmatrix} x_1(t_j) \\ x_2(t_j) \end{pmatrix} + \begin{pmatrix} \eta(t_j) \\ 0 \end{pmatrix} \quad (3.26b)$$

where the system noise $\epsilon(t_j)$ and the observational noise $\eta(t_j)$ are modeled by Poissonian noise components, and c is a constant normalization factor. See Fig. 3.9 for an example.

The estimation of the parameters in LSSMs is more complicated than for AR processes (see König & Timmer, 1997, and references therein). The parameters of an LSSM[p] fit are estimated using a maximum likelihood procedure; a set of parameters is derived, for which the probability of observing the measured light

curve $y(t)$ is at maximum. Those parameters are obtained using the expectation-maximization algorithm (Honerkamp, 1994). The method is iterative, starting from a set of initial values. In the expectation step, the Kalman filter is applied, which allows to estimate the unobservable system-light curve $x(t_j)$ by using the observed light curve $y(t_j)$ and a given set of LSSM parameters. In the next step the likelihood function is maximized, taking the estimated $x(t_j)$ into account and providing a new set of parameters. The results of this iterative procedure are best estimates for the LSSM[p] parameters and for the intrinsic system light curve. To quantify the order, p, of the hidden AR process the Kolmogorov-Smirnov Test (KS) is used (Honerkamp, 1994; König, 1997). This test compares the residuals between the estimated light curve $y(t_j)$ and the observed one $x(t_j)$ with the white noise null hypothesis. See lower panel in Fig. 3.9.

The length and time resolution of light curves, which are analyzed by LSSMs, have to be chosen considering the following requirements (König, 1997): (1) the duration of the light curve has to be several times the relaxation time scale (at least 5 times longer), and (2) the bin time has to be well below the relaxation time scale (at least 10 times smaller).

For the application of this procedure in the presence of gaps in the observed light curve a "gap"-filling process has to take place. The gaps are filled with white noise with the same mean and rms as the original time series in order to create a continuous time series. This procedure is repeated several times to guarantee stability and to derive error bars of the parameters in the presence of gaps.

Significance of period detection

This chapter is restricted to the two most common methods for variability analysis of astronomical sources; periodogram analysis (often called power spectrum density analysis, PSD) and epoch-folding ($\chi^2(P)$). A description of these methods have been given in chapter 3. In both methods the detection of a periodic signal is claimed if the PSD or $\chi^2(P)$ value at the period of interest is significantly above the values of the testing statistics surrounding this period. Since the method to estimate the significance of possible periods is the same in both cases, I will refer to that *power diagram*, PD, as a common term for both the PSD and the $\chi^2(P)$ technique.

Traditionally, the detection of periodic signals through peaks in the sample power diagram has been carried out either by eye, in all those cases in which the peak amplitude is so large that it is self-evident, or by ruling out (at a given confidence level) that a peak originates from an underlying white noise. The latter technique implicitly assumes that the power diagram does not possess any conspicuous "colored" components above the white noise. Were the X-ray light curve evenly sampled and dominate by pure white noise, the significance can be easily determined from the statistical properties of the power diagram (see chapter 3 and references therein). Indeed, the very presence of "colored" continuum power diagram components resulting from source variability noise makes the detection of significant peaks in the power diagram a difficult statistical problem. In general, establishing whether or not a sample peak originates from a periodic modulation requires an evaluation of the peak significance with respect to the local continuum of the sample power diagram, which in turn, can be dominated by the aperiodic variability of the source. In this chapter, I present a technique for detecting peaks in the power diagram arising from periodic modulation in the presence of "colored" power diagram components. This technique is based on Monte Carlo simulations following the algorithm presented by Timmer & König (1995) and the method described by Benlloch et al. (2001b). The approach involves simulating many light curves that match the real data in sampling time, count rate, and vari-

ance, and comparing their power diagrams to the power diagrams of the real data. For a discrete peak in an observed power diagram to be significant, it must have greater power than nearly all of the simulations at that frequency.

4.1   *Generating simulated light curves*

How the Monte Carlo light curves are produced is critical, if the significance level of any peak seen in a noise power diagram is to be determined. Usually, an inverse Fourier transformation is performed on a model PSD to give the simulated light curves. The popular "phase randomization" method (Done et al., 1992), determines the Fourier amplitude from the square root of the power-law shaped PSD and assumes the Fourier phase to be uniformly distributed in $[0, 2\pi[$. There are two reasons why this method can give statistically wrong results. First, since this procedure chooses a deterministic amplitude for each frequency and only randomizes the phases, all simulated light curves thus exhibit a trend caused by the dominating lowest frequency. Secondly, note that the periodogram of a noisy light curve must obey the usual periodogram statistics: the PSD follows approximately a χ^2 distribution with two degrees of freedom, χ_2^2, i.e., the standard deviation of each PSD point is of the same magnitude as the PSD value itself such that the periodogram is fluctuating wildly (see, e.g., van der Klis, 1989). "Phase randomization" does not take into account this randomness of the periodogram according to the χ_2^2 distribution and therefore the uncertainty of the related distribution of the estimated periods is significantly underestimated. In other words, noise PSDs have a larger scatter than those obtained from "phase randomization". This is important since these outliers could be interpreted as periodic or quasi-periodic oscillation, QPO, which in reality result from the statistics of the noise process.

Since "phase randomization" does not produce light curves with the correct noise statistical characteristics and leads to overestimation of the significance of QPO detections, we must seek a better algorithm for producing simulated light curves. Timmer & König (1995) proposed such an algorithm (used also by Green, McHardy & Done, 1999) which allows randomness both in phase and in amplitude, producing the desired χ_2^2 distribution in the periodogram. It will be explained in detail in the following. As an illustration, three simulated examples of red noise light curves with significance levels obtained from the Monte Carlo simulations are displayed in Fig. 4.1. We also display the significance levels (which will be explained in section 4.2) obtained with "phase randomization" to indicate that these levels are in fact much smaller than the correct levels and therefore overestimate the significance of an apparent period.

To simulate the light curve, we first specify a PSD model which we wish to

test the data against. To determine the shape of the PSD model, we apply the "response method" of Done et al. (1992) and Green, McHardy & Done (1999), where simulations of light curves of known power spectrum (following the algorithm of Timmer & König, 1995) with the same mean, variance, and sampling characteristics as the observed data, are used as a means of investigating the form of the intrinsic power spectrum. For each trial form of the intrinsic power spectrum, 1000 random simulations of light curves with that form of power spectrum, scaled to the original data and with the same uneven sampling are produced. The multiple independent power spectra of these light curves are combined to give a mean simulated power spectrum and the error on the power at each frequency bin is derived from the rms spread in the multiple values of the simulated power at that frequency. This model power spectrum with errors is then compared to the observed power spectrum using the χ^2 statistic (see Done et al., 1992, for an in depth explanation). Varying the parameters and normalization of the model periodogram, the best χ^2 fit determines that PSD model which best describes the observed data.

Once we have chosen a PSD model, we generate the Fourier frequencies at which the PSD is to be computed

$$\omega_i = \frac{2\pi i}{\Delta t N_0} \tag{4.1}$$

where N_0 is the total number of points of the final light curve, $i = 0, 1, \ldots, N_0/2$, and Δt is the resolution of the light curve. Then, the PSD-value for each ω_i using the user-defined function is computed. To generate the light curve from this simulated PSD the real and imaginary parts of the Fourier transform of the simulated PSD, FT, will be determined from

$$\Re\mathrm{FT}(\omega_i) = \alpha_1 \cdot \sqrt{\mathrm{PSD}} \tag{4.2}$$

$$\Im\mathrm{FT}(\omega_i) = \alpha_2 \cdot \sqrt{\mathrm{PSD}} \tag{4.3}$$

where α_1 and α_2 are Gaussian distributed random numbers. The branch for the negative Fourier frequencies is then computed from the above $\mathrm{FT}(\omega_i)$ using the standard relations for the Fourier transform of a real variable ($\mathrm{FT}(\omega_j) = \mathrm{FT}^*(\omega_j)$ where the asterisk denotes complex conjugation). The simulated light curve is constructed by applying the inverse Fourier transform to the FT, i.e., converting the frequency domain into the time domain, and by renormalizing the light curve to the desired mean count rate and variance.

Note that this approach does not yet take the observational sampling of the desired light curve into account, but generates light curve values for equally spaced times $t = i\Delta t$ with $i = 0, 1, \ldots, N_0\Delta t$. In simulations of real observations, the time

resolution, Δt, of the observation should be first determined and a light curve with that Δt will be simulated. To ensure that the light curve accounts for variability on time scales longer than the observed light curve (including a red noise leak contribution if necessary, see chapter 3.1.1.2) one very long segment of length $n \times T$, with T the total duration of the observed light curve, $T = N_0 \Delta t$, is simulated. A light curve of duration T is then drawn at the starting time from this time series and then resampled as the original light curve, by determining all gaps present in the observation and removing these time intervals from the simulated data. This approach produces a simulated light curve with a sampling which is usually close to but not identical to the sampling of the observation (differences between the simulated and the observed light curve sampling can occur at the edges of the gaps, where bins might get ignored or added to the simulated light curve due to roundoff errors).

Finally, we note that Poisson noise introduces additional "observational noise" in the measured light curves and it must be added to the simulated light curves after the inverse Fourier transform. For each time bin, the number of observed photons is drawn from a Poisson distribution with its mean given by $r(t)\Delta t$, where $r(t)$ is the simulated count rate and Δt is the bin-width. For data with new instruments such as *XMM-Newton*, with a high signal to noise ratio, this latter step can be ignored if the source is bright enough. For earlier instruments such a simplification of the Monte Carlo algorithm is not possible. We note that in earlier work the low signal to noise of the data would result in the observational noise dominating the simulated light curves. Then, the PSD statistics asymptotically approach the χ_2^2 distribution for low source count rates. As a result, the error made by employing phase randomization and thus the overestimation of the period significance would be less in this case than with newer, source dominated, data of a high signal to noise ratio.

4.2   *Significance levels*

When studying a feature in a power diagram, PD ($\chi^2(P)$ or PSD), we can ask two different questions: (1) What is the significance of a QPO peak at a given (predefined) frequency (the "local significance" of the QPO), and (2) what is the significance of a QPO feature seen in a given frequency range (the "global significance" of the QPO). These are very different questions, as we have more knowledge about the QPO in the "local significance" case (we do know its frequency), but for "global significance", we are only interested in whether any feature *somewhere* in the interesting frequency range is significant or not. A formula for determining the significance of a peak in the PSD or in $\chi^2(P)$ for noisy light curves have
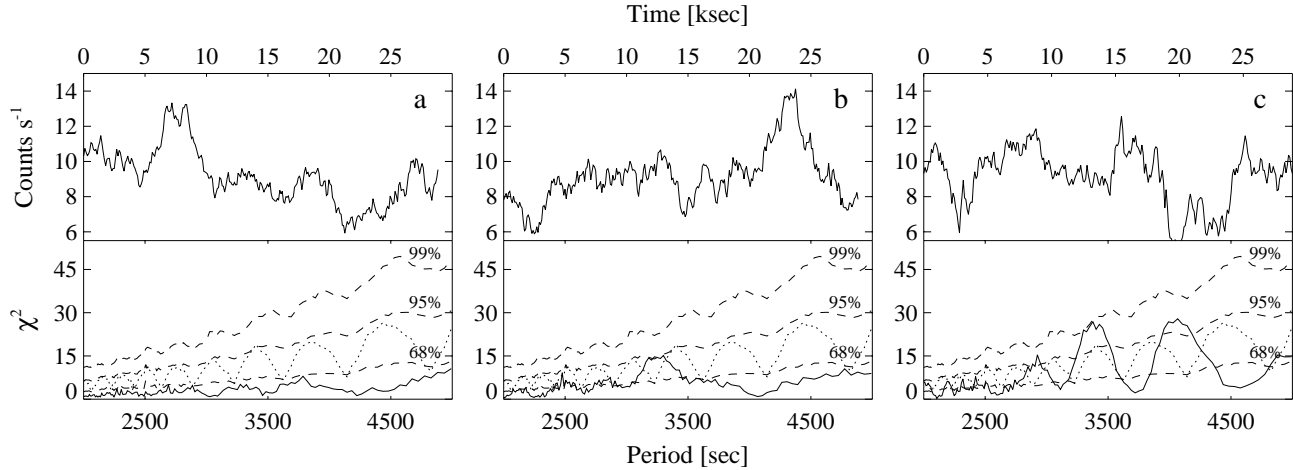
Figure 4.1: Three examples of typical red noise light curves for a process with an $f^{-1.9}$ spectrum binned to a resolution of 100 s using the method described by Timmer & König (1995). *Upper panels*: Simulated red noise light curves. *Lower panels*: $\chi^2(P)$ curves from epoch-folding (solid line) of the corresponding simulations. The dashed lines represent the 99%, 95%, and 68% "local significance" levels (see text for definition) obtained for a sample of 5000 Monte Carlo simulations. The dotted line represents the 99% significance level obtained with the "phase randomization" method, which overestimates the significance of the peaks in the $\chi^2(P)$ curves. Note that the presence of one or more peaks in the $\chi^2(P)$ curve is far from unusual for red noise light curves.

been presented by us in (Benlloch et al., 2001b). We use the common approach of Monte Carlo simulations (see Horne & Baliunas, 1986) where a large number ($\gtrsim$1000) of light curves with the same statistical properties and the same temporal sampling as the original light curve are generated following the method presented in the last section and their PD is computed.

To obtain the "local significance" of an observed peak at the frequency of interest, we first calculated the PD of each of the Monte Carlo realizations. For each trial frequency, we then computed the distribution of the PD values at this trial frequency from all realizations. One then determines the statistical distribution of the resulting power diagram value at the frequency of interest. A deviation of the measured PD from the noise PD is significant if it is above a certain threshold determined from this distribution. Typically, threshold values of 99% or even 99.9% are used (Bevington & Robinson, 1992). We usually used the 99%, 95%, and 68% "local significance" levels (see Fig. 4.1).

For the "global significance", a similar approach is used. Since we are looking at PD values determined at different frequencies, one has to take the noise character of the data and window effects into account. Instead of directly using PD values, more robust tests can be devised by first dividing the computed individual PD values by the average $\langle PD \rangle$, obtained by averaging the PD curves of the simulated light curves. To determine the "global significance" of the maximum peak of an observed light curve, we compare this value to the distribution of $\xi_{\max} := \max \{PD/\langle PD \rangle\}$ from the simulated light curves. Here, the maximum is to be taken over the frequency range of interest. We would consider an observed peak as likely due to a physical effect only if it is above the 99% threshold determined from the distribution. The maximum peaks present in the red noise light curves of Fig. 4.1b and c have a "global significance" of 61% and 80% respectively. Similar global tests apply to the distribution of the 2nd or 3rd largest PD value, but we do not use them here. See section 5.2 for an example with real data of determining the "local" and "global significance" of a putative QPO present in an X-ray observation of the AGN Mrk 766.

Active Galactic Nuclei

Variations at all wavelength are a common characteristic in Active Galactic Nuclei, AGN (see Peterson, 2001, for the most recent review). The variations appear to be aperiodic and have variable amplitude. In the X-ray band, they show large amplitude, rapid variability (on time scales of < 1 day) which has been taken as evidence that the X-rays come from very close to the central black hole (Rees, 1984; Marshall, Warwick & Pounds, 1981). However, the mechanism producing such variations remains unresolved. X-ray variability on long time scales from years down to days has also been reported (see Kawaguchi & Mineshige, 1998, and references therein). Presumably long-term variability is caused by changes in the global accretion rate, although there is as yet no consensus on how the variability is produced. AGN have also been found to have spectral variability, which usually contains broad emission lines varying both in flux and in profile. Over time scales of months and years, the changes can be very dramatic, but on shorter time scales they are more subtle. See Mushotzky, Done & Pounds (1993) for an excellent review of the X-ray spectra and time variability of AGN. Also in chapter 2.1 of this thesis the basic characteristics of AGN X-ray variability are summarized.

In this chapter, I will present the data analysis of two well known AGN, Cen A and Mrk 766. The data and analysis have already been published in Benlloch et al. (2001a,b). The data stems from different satellites, and also the purpose of the analysis is different. In the case of Cen A, we report the analysis from a ~110 ks of X-ray observations of Cen A carried out with the Proportional Counter Array (PCA) and the High Energy X-ray Timing Experiment (HEXTE) instruments on Rossi X-ray Timing Explorer (*RXTE*) during three monitoring campaigns between 1996 and 2000. Timing and spectral analysis are presented, on short and long time scales. In the case of Mrk 766 we discuss the presence of a claimed QPO of about 4200 s in a 29 ksec *XMM-Newton* observation of May 20, 2000.

5.1   Cen A

At a distance of 3.5 Mpc (Hui et al., 1993), Centaurus A (NGC 5128) is by far
the nearest AGN. Cen A is a giant double-lobed radio source usually classified
as a low luminosity Fanaroff & Riley (1974) Class I radio galaxy, a misdirected
BL Lac object (Morganti et al., 1992), a Seyfert 2 object (Dermer & Gehrels,
1995), and a radio-loud AGN viewed from the side ($\sim 70°$) of the jet axis (Ebneter
& Balick, 1983). Even though the nucleus is heavily obscured (in part by the
famous dust-lane that is seen to cross the galaxy, see Fig. 5.1), Cen A is one of the
brightest extragalactic X-ray sources in the sky and the only AGN where a high
quality spectrum from 0.5 keV to 1 GeV can be obtained (Steinle et al., 1998).
This makes it a valuable laboratory to test our understanding of the high-energy
processes occurring within AGN. A recent comprehensive review of Cen A is
given by Israel (1998).

Previous observations have shown Cen A to have highly complex X-ray/gamma-
ray properties (Turner et al., 1997a; Döbereiner et al., 1996; Feigelson et al., 1981;
Schreier et al., 1979) with multi-temperature diffuse flux, a spatially resolved jet
in radio and X-rays (Kraft et al., 2000; Morganti et al., 1999), and a nuclear com-
ponent with complex low energy absorption and a photon index of ~ 1.7. Iron
K-shell absorption and fluorescent line emission at ~ 6.4 keV with an equivalent
width of ~ 100 eV have been observed (Turner et al., 1997a). One unusual spec-
tral feature of Cen A is that there is no evidence for a strong Compton reflection
component (Woźniak et al., 1998, found $\Omega/2\pi < 0.15$). This implies there is little
cold, Thomson-thick material in the close vicinity of the AGN that reflects X-rays
into our line of sight. Taken together with the iron line equivalent width, this re-
sult is consistent with transmission of the primary flux through the line-of-sight
absorber and viewing the accretion disk nearly edge-on. On the other hand, the
lack of a reflection component is at odds with the "Unified Model of AGN" (e.g.,
Krolik, 1999, chapter. 12), where Seyfert galaxies do show significant reflection
components (Smith & Done, 1996).

Here we presented results of three observations performed by the *RXTE* – one
of 10 ks in 1996 August, one of 74 ks in 1998 August and one of 25 ks in 2000
January (Benlloch et al., 2001a). Preliminary results from the 1996 August ob-
servation, using earlier versions of the response matrix and background models,
have been presented by Rothschild et al. (1999). We re-analyzed these data using
newer and improved PCA response matrices and background models, and present
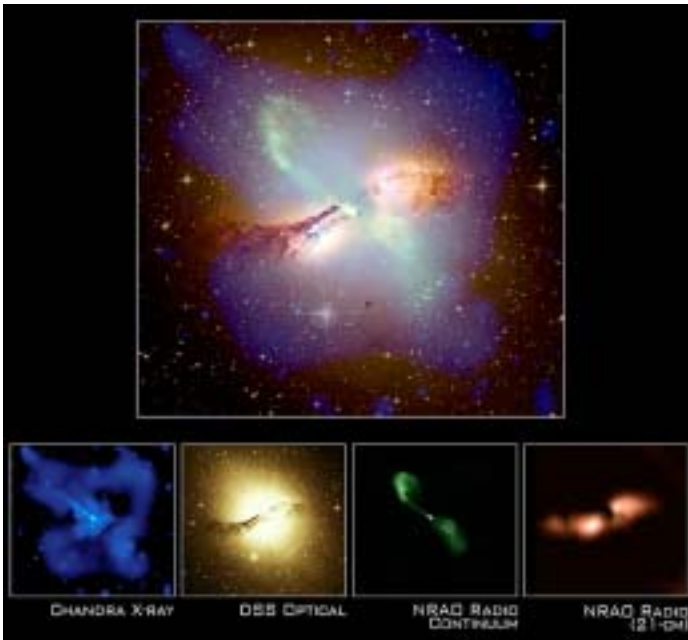results on all three observations.

Figure 5.1: A composite X-ray (blue), radio (pink and green), and optical (orange and yellow) image of the galaxy Centaurus A. `http://chandra.harvard.edu/photo/2002/0157/index.html`.

5.1.1 RXTE *observations and data reduction*

There are two pointed instruments on-board *RXTE*, the Proportional Counter Array (PCA) and the High Energy X-ray Timing Experiment (HEXTE). *RXTE* observed Cen A for a total of ~110 ks over the last five years. An observation log is given in Table 5.1. The PCA light curves are shown in Fig. 5.2.

The PCA consists of a set of five co-aligned xenon/methane (with an upper propane layer) proportional counter units (PCUs) with a total effective area of ~7000 cm^2 . The instrument is sensitive in the energy range from 2 keV to ~100 keV (Jahoda et al., 1996). As the response matrix is best calibrated between ~2 and 20 keV, we will restrict our analysis to this energy range. To increase the signal to noise ratio we chose only the data from the top xenon layer. Background subtraction of the PCA data was performed using the "faint source model". To reduce the uncertainty of the PCA background model, we ignore data measured in the 30 minutes after South Atlantic Anomaly (SAA) passages. Furthermore, data were
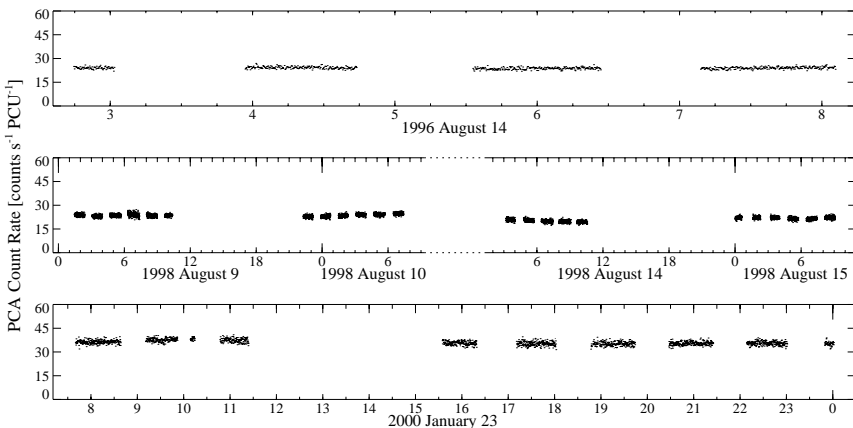
Figure 5.2: Background-subtracted *RXTE*/PCA light curves of Cen A for the three *RXTE* monitoring campaigns in the years 1996 (upper panel), 1998 (middle panel) and 2000 (lower panel). The data have a resolution of 16 s and are plotted versus Universal Time (UT) in hours on the given date.

not accumulated at times of high electron contamination as expressed by a certain ratio of veto rates in the detectors, the so-called "electron ratio". We excluded times during which the "electron ratio" was larger than 0.1 in at least one of the detectors. We accounted for the remaining uncertainty in detector calibrations by including a systematic error of 1% in the data. See Wilms et al. (1999) for an in-depth discussion of the PCA calibration issues.

HEXTE consists of two clusters of four NaI(TI)/CsI(Na) phoswich scintillation counters that are sensitive in the range 15–250 keV (Rothschild et al., 1998). Its total effective area is ~1600 cm^2. Background subtraction is done by sequential rocking of the two clusters on and off of the source position to provide a direct measurement of the background during the observation. Thus, no background model is required. HEXTE data between 20 keV and 200 keV were used. To ensure good statistical accuracy the spectrum was rebinned for fitting, and no systematic errors were incorporated in the HEXTE data.

The standard data from both instruments were used for the accumulation of spectra and light curves with 16 s time resolution. To extract spectra and light curves, we used the *RXTE* analysis software in FTOOLS 5.0. During part of the observations some PCUs were turned off, and we took this into account when we added all good PCU data together and combined all background spectra. The total PCA response matrix was the average of the respective estimates for each

Table 5.1: Details of the *RXTE* monitoring campaigns of Cen A

Numb.	Obs. Date	Exposure	Count Rate
	(ymd)	(sec.)	(counts s^{-1} PCU^{-1})
1.	1996, Aug 14	10528	24
2.	1998, Aug 9–15	73984	22
3.	2000, Jan 23	24880	36
	total ~109.5 ks		

(The count rate is the mean of the 2–20 keV PCA background subtracted count rate)

individual detector combination, weighted by the fraction of photons measured during the time that such combination was active. For HEXTE we used the standard response matrices dated 1997 March 20, treating each cluster individually in the data analysis.

On-board *RXTE* there is a third scientific instrument, the All-Sky Monitor (ASM, Levine et al., 1996). The technical features of this instrument will be described in detail in chapter 6.1. The overall energy range of the ASM is 1.5–12 keV which is telemetered in three energy channels (1.3–3.0 keV, 3.0–5.0 keV, and 5.0–12.2 keV). Fig. 5.3b shows the *RXTE*/ASM counting rate for Cen A from the beginning of the *RXTE* mission, rebinned in 14 d bins; the arrows denote the times when the PCA/HEXTE monitoring campaigns were made. We used the "Data by dwell quick-look results" provided by the *RXTE*/ASM team, available from MIT ASM Light curve Overview Web pages. We took only flux solutions for which $\chi^2_{\mathrm{red}} < 1.2$, with a background estimated between 1 and 10 counts s^{-1} (Levine et al., 2000) and with a full dwell-exposure time (i.e., 90 s) .

Also shown in Fig. 5.3c are the 20–100 keV count rates from the BATSE instrument on board the Compton Gamma Ray Observatory (*CGRO*) averaged over two week intervals from 1991–1999 (data provided by C. Wilson, priv. comm.). BATSE consists of eight identical NaI(Tl) scintillation detector modules located at the corners of *CGRO*. Sources are detected using the Earth occultation technique. During each *CGRO* orbit, the Earth is seen by BATSE to sweep across a band in the sky extending ~35° above and below the orbit plane. As each source enters into (exits from) occultation by the Earth, count rates in the source-facing detectors decreases (increase) according to the source intensity.

5.1.2 Spectral analysis

The PCA and HEXTE data were fit simultaneously using XSPEC v. 11.0q (Arnaud, 1996). The spectrum was modeled by a heavily absorbed power law plus a
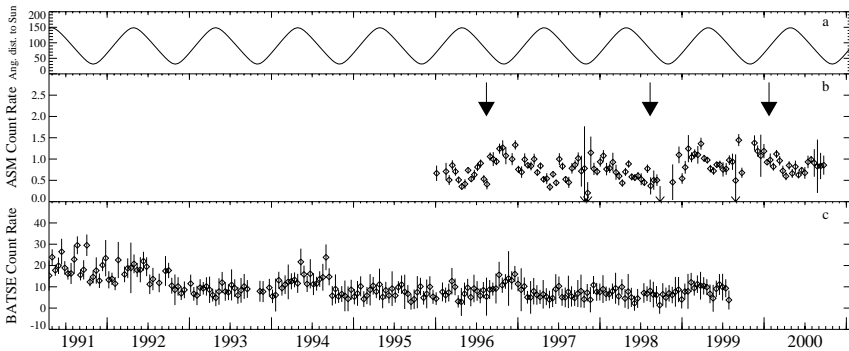
Figure 5.3: *(a) Angular distance between the Sun and Cen A. (b) ASM counting rate for Cen A from the beginning of the RXTE measurements, rebinned in 14 d bins. The RXTE PCA/HEXTE monitoring campaigns are indicated by the arrow. (c) BATSE counting rate for Cen A from the beginning of the CGRO measurements, rebinned in 14 d bins.*

Gaussian emission line model, of the form

$$N_{\mathrm{ph}}(E) \quad = \quad A_{\mathrm{Det}}\left[\mathrm{e}^{-\sigma_{\mathrm{ISM}}(E)N_{\mathrm{H}}}A_{\mathrm{PL}}E^{-\Gamma} + \frac{A_{\mathrm{Line}}}{\sqrt{2\pi\sigma^2}}\mathrm{e}^{-\frac{(E-E_{\mathrm{Fe}})^2}{2\sigma^2}}\right] \tag{5.1}$$

To account for the uncertainty in the effective areas of the three detector systems (the PCA and the two HEXTE clusters), we included their relative normalizations, A_{Det}, as a fit parameter, setting the PCA normalization to unity. For the photoelectric absorption of the interstellar medium, σ_{ISM}, we used the photoelectric absorption cross section of Morrison & McCammon (1983) where N_{H} is the equivalent hydrogen column. The fit parameters of the photon power law are Γ the photon index and A_{PL} the power law norm (ph $keV^{-1}\,cm^{-2}\,s^{-1}$ at 1 keV). To model the iron line component a Gaussian line profile was added where E_{Fe} is the line energy, A_{Line} the total ph $cm^{-2}\,s^{-1}$ in the line, and σ the Gaussian line width. As preliminary fits with the iron line width as a free parameter resulted in widths narrower than the spectral resolution of the PCA, we fixed the line width to $\sigma = 0.2\,\mathrm{keV}$.

The spectral model was fitted to each data set separately (the 1996, 1998, and 2000 separated spectra) and to the three data sets simultaneously (the joined spectrum). Table 5.2 provides fitted parameters and their associated uncertainties. Our adopted simple spectral model (Eq. 5.1) provides a fully acceptable fit in each case. Note that we assume that the iron line is not absorbed by the intervening material. This physically implies that the reprocessing region in which the Fe line is produced is outside the absorbing line of sight, and thus, the high absorp-

Table 5.2: Best Fit Spectral Parameters for the 1996, 1998 and 2000 data set fitted separately (Separated spectra) and for the three data sets fitted simultaneously (Joined spectrum).

	Separated spectra			Joined spectrum		
	1996	1998	2000	1996	1998	2000
N_{H}	11.30(14)	9.41(28)	7.87(27)	10.66(18)	09.15(19)	8.70(19)
Iron line:						
E_{Fe}	6.56(16)	6.47(8)	6.27(9)	6.49(7)	6.45(8)	6.29(11)
A_{Line}	4.36(74)	3.97(63)	5.46(98)	5.34(62)	4.28(54)	3.82(87)
EW	144(26)	142(27)	120(26)	177(24)	154(22)	82(20)
Power-law:						
Γ	1.92(15)	1.90(2)	1.82(2)	1.88(1)	*1.88*	*1.88*
A_{PL}	0.135(2)	0.114(4)	0.150(6)	0.122(3)	0.108(2)	0.173(4)
Detector norm.:						
$A_{\mathrm{Det_A}}$	0.90(6)	0.92(3)	0.92(3)	*0.90*	*0.92*	*0.92*
$A_{\mathrm{Det_B}}$	0.88(9)	0.90(3)	0.92(3)	*0.88*	*0.90*	*0.92*
$F_{(2-10\,\mathrm{keV})}$	2.28(4)	2.21(4)	3.60(6)	2.28(3)	2.21(3)	3.58(3)
χ^2_{red}	0.75	0.51	0.40	0.78	*0.78*	*0.78*
d.o.f.	64	77	60	209	*209*	*209*

E_{Fe}: line energy. A_{Line}: Line normalization (ph $cm^{-2}\,s^{-1}$ in the line). The Gaussian line width was fixed at $\sigma = 0.2\,\mathrm{keV}$. EW: line equivalent width. Γ: Photon index of the power-law. A_{PL}: Power-law norm (ph $keV^{-1}\,cm^{-2}\,s^{-1}$ at 1 keV). $F_{(2-10\,\mathrm{keV})}$: Flux at the energy range of 2 to 10 keV in units of ph $cm^{-2}\,s^{-1}$. $A_{\mathrm{Det_A}}$: Ratio of HEXTE to PCA Normalization for Cluster A. $A_{\mathrm{Det_B}}$: Ratio of HEXTE to PCA Normalization for Cluster B. The uncertainties are 90% for one parameter ($\Delta\chi^2 = 2.7$), and are shown in units of the last digit shown. Parameters in italics were frozen.

tion column is very near the X-ray emission region at the core of the AGN. This assumption only affects the inferred flux of the line and its computed equivalent width.

For all three observations, the energy of the iron line, ~6.4 keV, indicates that the emission is from at most weakly ionized material. It is either possible, (1) that the Fe-line emitting material lies directly along our line of sight, and could thus be associated with matter producing the observed N_{H}, or (2) that the Fe-line emitting material is caused by fluorescent emission of a larger spatial region. In the former case, i.e., the emission of line photons from within our line of sight, we would expect the line flux to be correlated with N_{H}. Within the uncertainty of the fit parameters, such a correlation is not found, as there is no variability in the line flux with observation while N_{H} varies. Such a constancy of the line flux is only possible if the line emission originates outside of our line of sight, for example within the torus. Here, the line strength would not correlate with the variation of N_{H}. Furthermore, we would also not expect a correlation with changes of
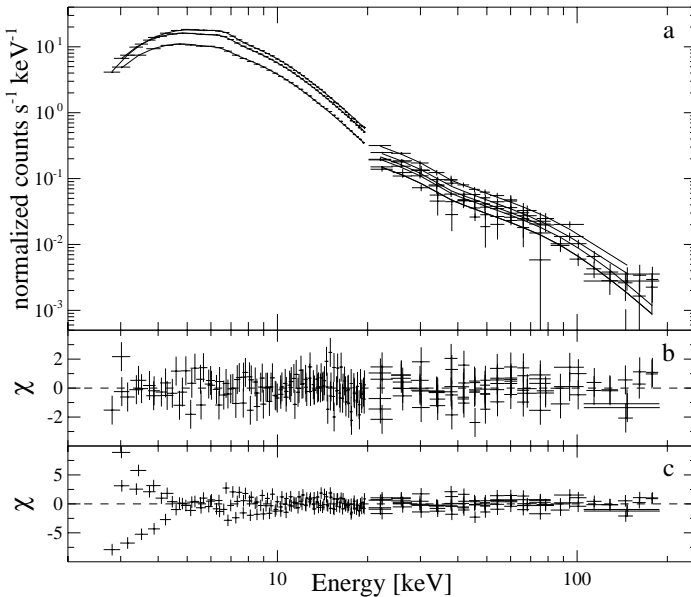
Figure 5.4: *(a)* Best fit joined spectrum for an absorbed power law plus Gaussian emission line with $\sigma = 0.2\,\mathrm{keV}$. See Table 5.2, joined spectrum, for the exact values of the fit parameters. See text for explanations. *(b)* Residuals to the fit in terms of σ with error bars of size one. *(c)* Residuals to the fit with coupled spectral parameter for the three *RXTE* observations.

the source flux since these would be smeared out on the light travel time scale, which can be several years. Note that the equivalent width of the line decreases between the observations. This decrease, however, is purely due to the factor of 1.6 increase in the continuum flux over the observations. Finally, we note that our conclusion, that the Fe-line emitting material lies outside of our direct line of sight, is consistent with estimates for the line strength caused by the absorbing material alone, which predict that < 20% of the line flux is caused by fluorescence in the absorbing material (see section 5.1.4).

Apart from the changes in the power law normalization (+11% with respect to 1996) and in the N_{H} (−30% with respect to 1996) there is no significant changes of the spectral parameters between the three observations. In passing, we note that the same holds also true when analyzing the spectra observed during each individual orbit. No significant variation of the spectral parameters was found within each monitoring observation.

As the spectral parameters remain roughly constant between the observations, it is possible to further constrain the shape of the spectral continuum by fitting all data simultaneously. We first attempted to fit all the data with a single model by coupling all spectral parameters (with the exception of the power law flux) for the three data sets. Our fit to this model had strong residuals in the region below 10 keV (see Fig. 5.4c), clearly indicating the variation in N_{H}. The fit corroborates that the shape of the underlying power-law continuum might be constant. We therefore modeled the combined spectrum using a model where all parameters were allowed to vary freely with the exception of the photon index, which was held fixed for the three data sets. The fitted parameters for this fit are listed in Table 5.2 (joined spectrum), a plot of the spectral model and its residuals is shown in Figs. 5.4a and 5.4b. The good χ^2 of this fit indicates that Γ can indeed be assumed to be constant for the three observations.

In order to test for the presence of a Compton reflection component, a power law plus Compton component (XSPEC model `pexrav`, Magdziarz & Zdziarski, 1995) fit was performed to both, the individual observations and the joined data with a single power law index. The 2σ upper limit for the reflection component, $\Omega/2\pi$, expressed as the ratio of the solid angle for primary flux scattered into our line of sight to an infinite slab, was found to be 0.09, 0.09, 0.08, and 0.05 for the observations in 1996, 1998, 2000, and joined, respectively, assuming an inclination angle of $70°$. This result clearly implies that no significant reflection features are present, confirming the earlier *CGRO* and *RXTE* results (Rothschild et al., 1999; Kinzer et al., 1995).

We also tested the *RXTE* data for the presence of a spectral break at higher energies, using an exponentially cutoff model (XSPEC model `cutoffpl`). The best fit model gave a cutoff-energy with a lower limit of 500 keV and provides an equally adequate fit to the data as the straight power law ($\chi^2_{\mathrm{red}} = 0.65$). This result is consistent with *CGRO*/OSSE data, where a cutoff energy of 300 keV or higher was found (Kinzer et al., 1995). We would not be sensitive to a break of $\Delta\Gamma = 0.5$ at 150 keV, as reported by Steinle et al. (1998), due to limited statistics above 150 keV.

To summarize, the *RXTE* spectrum of Cen A can be best described by a heavily absorbed power law extending above 200 keV and an iron line from cold matter. A significant width to the iron line was not required, and therefore it was taken to be narrow ($\sigma = 0.2$ keV). No significant measurements of a steepening in the power law at high energies was detected. A Compton reflection component was not required to fit the data with $\Omega/2\pi \leq 0.05$.

A bright X-ray transient , 1RXH J132519.8−430312, was detected by Steinle, Dennerl & Englhauser (2000) during *ROSAT*/HRI observations in July 1995 2.′5 south-west to the nucleus of Cen A. Parallel multi-wavelength observations from

radio to γ-ray of Cen A were made (Steinle et al., 1999) and no counterpart was found in the optical images. Unfortunately, no spectral information is available from the observations, and only indirect information can be derived from the BATSE and OSSE instruments, which provide evidence that the transient emits mainly at soft X-rays. Steinle, Dennerl & Englhauser (2000) suggested the transient could be an X-ray binary located in Cen A. Assuming a power-law spectrum with photon index 1.5 and a $N_{\rm H} = 8 \times 10^{20} \, {\rm cm}^{-2}$, and taking the *ROSAT*/HRI average count rate of $0.033 \, {\rm counts \, s}^{-1}$ obtained by Steinle, Dennerl & Englhauser (2000), we estimate a *RXTE*/PCA count rate of $0.36 \, {\rm counts \, s}^{-1} \, {\rm PCU}^{-1}$ (using the PIMMS tool supported by HEASARC). This represents $< 2\%$ of the measured Cen A PCA count rate, and therefore no significant contribution of the transient source (if it is supposed to be turned on) on the *RXTE* observations is expected. This is also confirmed by the spectral behavior of the data, where no excess softness is presented in the spectral fit (see Fig. 5.4).

5.1.3 Timing analysis

Variability is one of the well known features of Cen A and is observed in all wavelength regimes from radio to γ-rays (Abraham, Kaufmann & Botti, 1982; Turner et al., 1992; Terrell, 1986; Bond et al., 1996; Kinzer et al., 1995). At X-ray wavelengths, Cen A is known to be highly variable on time scales of years, months, and days (Jourdain et al., 1993; Baity et al., 1981). This variability can be split into two main components (Jourdain et al., 1993): (1) long-term trends which last for years and define the state of the source and (2) short-term flares of a few days which are superposed on the long-term component.

5.1.3.1 Short-term variability

To characterize the short-term variability of Cen A during the PCA/HEXTE observations we performed a standard χ^2-test for the light curves on different time scales. A reduced χ^2_ν value was computed for each stream of data to test for variability against the null hypothesis that the flux remains constant:

$$\chi^2_\nu = \frac{1}{\nu} \sum_{i=1}^{n} \frac{(c_i - \langle c \rangle)^2}{\sigma_i^2} \tag{5.2}$$

where c_i is the observed count rate at each time interval i, σ_i the respective Poisson error, $\langle c \rangle$ the mean count rate during the observation, n is the number of time bins, and $\nu = n - 1$ is the number of degrees of freedom. For a non variable source we expected $\chi^2_\nu \sim 1$. No variability within the measurement errors over time scales of days or less was detected for all the pointing observations of *RXTE*. Variations of

10% in the mean flux were detected over time scales of ~5 d during observation 2 (see Fig. 5.2, middle panel).

Fourier techniques were also used for the analysis of the long 1998 observation. An average power spectral density (PSD) using time segments of ~22 min duration was calculated. This duration was the longest time span for which enough time segments without gaps were available to compute a PSD. The analysis was performed for the PCA background subtracted data from 4 to 40 keV, where the data is source dominated. No excess variability above the Poisson level was seen (see Fig. 5.5), confirming the result of the χ^2 test in this frequency.

To compare the Cen A variability with previous studies of Seyfert Galaxies (Markowitz & Edelson, 2000; Turner et al., 1997b; Nandra et al., 1997) we extracted the 2–10 keV light curve of the 1998 monitoring campaign and computed the normalized "excess variance", $\sigma^2_{\rm rms}$ (for a detailed discussion of the definition see Turner et al., 1999; Nandra et al., 1997):

$$\sigma^2_{\rm rms} = \frac{1}{n \langle c \rangle^2} \sum_{i=1}^{n} \left[(c_i - \langle c \rangle)^2 - \sigma_i^2 \right] \tag{5.3}$$

We find $\sigma^2_{\rm rms} = 4.3(9) \times 10^{-3}$. Previous studies have found a clear decrease of $\sigma^2_{\rm rms}$ with the intrinsic X-ray luminosity of both Seyfert 1 and Seyfert 2 galaxies (consistent also with the time-domain results of König, Staubert & Wilms, 1997, and with Green, McHardy & Lehto 1993). Our result for Cen A is a factor of ~10 smaller than that expected from the Seyfert correlations (Turner et al., 1997b; Nandra et al., 1997) for the intrinsic (i.e., unabsorbed) X-ray luminosity of Cen A (log $L_{\rm X,\,2\text{-}10\,keV} \simeq 41.7$ cgs). Such a low $\sigma^2_{\rm rms}$ is typically only expected for Seyfert 2's with log $L_{\rm X}$ ~43 cgs (see Turner et al., 1997b, Fig. 2), although the scatter in these data is large. We conclude that the short-term variability of Cen A is on the low side of that observed in comparable Seyfert galaxies.

5.1.3.2 Long-term variability

To study the long-term variability of Cen A, and to place our pointed observations within the context of the overall behavior of the source, we used data from the *RXTE*/ASM and *CGRO*/BATSE all sky monitors (see Fig. 5.3).

Fig. 5.3b indicates apparent fluctuations in the ASM flux at the end of each year coinciding with the closest angular separation between the sun to Cen A (Fig. 5.3a). This variability is due to scattering of solar X-rays off the ASM collimator onto the ASM detectors and is not due to source flux variations (Remillard, priv. comm.).

The BATSE count rate is shown in Fig. 5.3c and does not display the variability seen in the ASM. Thus, we conclude that the Cen A flux appears to have varied
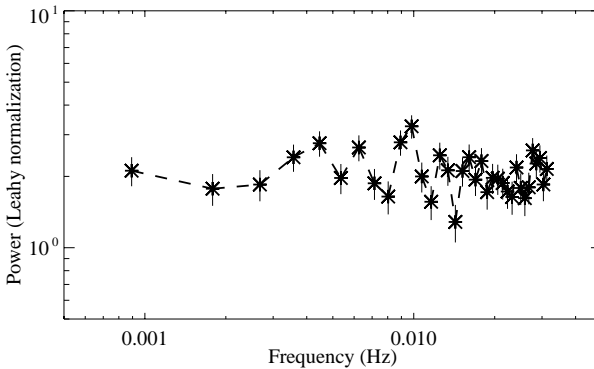
Figure 5.5: Averaged power spectral density (PSD) in Leahy et al. (1983) normalization of the PCA background subtracted source data. A PSD value of 2 corresponds to pure Poisson noise.

by less than a factor of two during the four years of the *RXTE* mission. BATSE data extending back to 1991 indicate that the same conclusion can be drawn back to at least mid-1992. Cen A was a factor of two brighter in the BATSE data from mid-1991 to mid-1992.

5.1.4   Conclusions

We have presented analysis of three *RXTE* monitoring campaigns of Cen A, totaling ~110 ks. This analysis reveals no significant short-term temporal variability on time scales from weeks or less, and a relatively simple spectrum in the 2–200 keV range. The best fit spectral model consists of a heavily absorbed primary flux and a narrow emission line from cool iron. The iron line flux remained stable at $\sim 4.5 \times 10^{-4}$ photons $\mathrm{cm}^{-2}\,\mathrm{s}^{-1}\,\mathrm{keV}^{-1}$ for unabsorbed flux and $\sim 5.3 \times 10^{-4}$ photons $\mathrm{cm}^{-2}\,\mathrm{s}^{-1}\,\mathrm{keV}^{-1}$ for absorbed flux.

The 2–10 keV flux was the same in 1996 and 1998, and increased by 60% in 2000. This implies that the line emitting region is not very close (greater than light days?) to the region containing the primary flux generation. This is consistent with the lack of a significant reflection component contribution to the overall flux. We conclude that the Fe line does not originate close to the central X-ray source, although a strong Fe line is observable. Possible sources of the Fe line flux would then be a molecular torus surrounding the source (similar to Seyfert 2 galaxies) or the dust lane. To test the latter hypothesis we have used a Monte Carlo code to compute the iron line flux emerging from the back of a slab of neutral material with $N_{\mathrm{H}} = 7 \times 10^{22}\,\mathrm{cm}^{-2}$ that is irradiated by the unattenuated continuum

spectrum of Cen A. The equivalent width of the line resulting from the absorbing material is $< 30\,\text{eV}$ so that most of the contributing Fe line photons do not come from the absorbing region. In agreement with Grandi et al. (2000) and Woźniak et al. (1998) this leaves us with the conclusion that the Fe line originates within material of a large column outside of the line of sight, for example in the postulated molecular torus. Our conclusion is also confirmed by the presence of no correlation between the variability behavior of N_H and the iron line flux, since N_H varied with observation and the line flux does not. The N_H could originate at the edge of the accretion disk and thus its variability might be due to small changes in the disk structure, while the iron line material lies outside the line of sight.

The lack of a reflection component in radio-loud active galaxies poses a problem for unification models of AGN. There are several ways in which a reflection-free AGN spectrum could be produced. First, the reflecting cold material could be removed from the inner regions by being "swept up" by the radio jet. For Cen A, there are indications that such a mechanism might be at work. In a recent interpretation of Hubble Space Telescope images taken with WFPC2 and NICMOS, Marconi et al. (2000) notice an evacuated channel produced by the jet between the nucleus and the first bright knot of the jet. A second possibility might be that the inner regions of the accretion disks of radio-loud AGN are not neutral, but strongly ionized. The source for the ionization could be radiation of the radio-jet, or the accretion disk structure could deviate from that of a simple accretion disk, and be, e.g., advection dominated (the latter is improbable, however, because of to the appreciable X-ray luminosity of the source). Lastly, it could also be possible that the production site of the primary X-rays is not within an accretion disk but within the base of the jet itself, such that the covering factor of any cold material present close to the central black hole is small. Observationally, this last interpretation has been advocated by Kinzer et al. (1995) in the analysis of *CGRO*/OSSE data from Cen A, where the energy dependence of the high energy cutoff of the power-law with source flux is interpreted in terms of a changing maximum energy of a nonthermal electron distribution that would be expected in the jet.

5.2 *Mrk 766*

Mrk 766 (NGC 4253) is a bright ($L_{2-10\,\text{keV}}$ ~few $10^{43}\,\text{erg}\,\text{s}^{-1}$) and nearby ($z = 0.0129$) narrow line Seyfert 1 galaxy observed through a relatively small Galactic column of $\sim 1.8 \, 10^{20}\text{cm}^{-2}$. It shows strong and rapid variability in his X-ray flux, as well as variability in the slope of their power-spectra continua (Leighly et al., 1996; Page et al., 2001). Mrk 766 displays a strong soft excess and broad features in the 1 keV spectra, which have been attributed to absorption in an ionized inter-
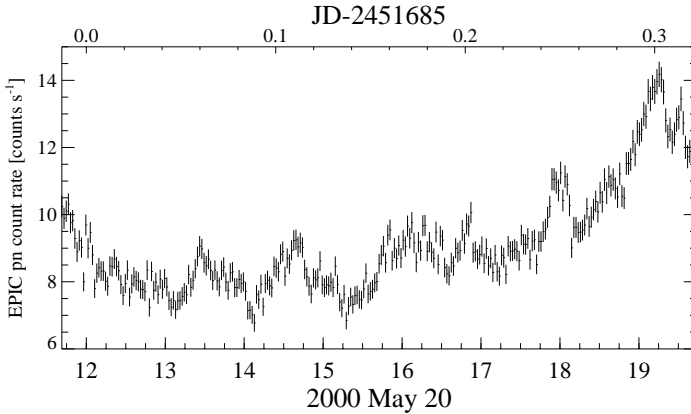
Figure 5.6: *XMM-Newton* EPIC-pn light curve of Mrk 766 for the 0.2–2 keV band with a resolution of 100 s.

stellar medium at some distance from the central massive black hole. The profile of the broad fluorescent Fe Kα line observed at 6–7 keV can be explained as due to the effects of relativistic motions an gravitational redshift in a disk surrounding the central black hole (Tanaka, Nandra & Fabian, 1995)

Mrk 766 was observed by *XMM-Newton* on 20th May 2000 during revolution 0082 and lasted ~60 ks. As result of the analysis of this observation a QPO in the range of 4200 s was claimed by Boller et al. (2001). Here we re-analyse the Mrk 766 *XMM-Newton* light curve and apply the "significance level" methods outlined in the previous chapter to the putative QPO. We find that the QPO claimed in Boller et al. (2001) has in fact low statistical significance (Benlloch et al., 2001b).

5.2.1   XMM-Newton *data extraction*

We concentrate on data from the European Photon Imaging Cameas, EPIC-pn, instrument (Strüder et al., 2001) which was operated in the small window mode during the observation. We extracted source photons from a circle of 9.5 pixels radius centered on the source (detector coordinates (37.5,54)). For the background, data from an off-axis position (18,17.5) extracted with a circle of then same radius were used. The time range of the light curve was chosen to be consistent with the approach of Boller et al. (2001) and results in an exposure time of 29 ksec. After background subtraction, we corrected the measured count-rates as is appropriate for the ~71% live-time during the 5.7 ms readout cycle of the pn-CCD (Kuster
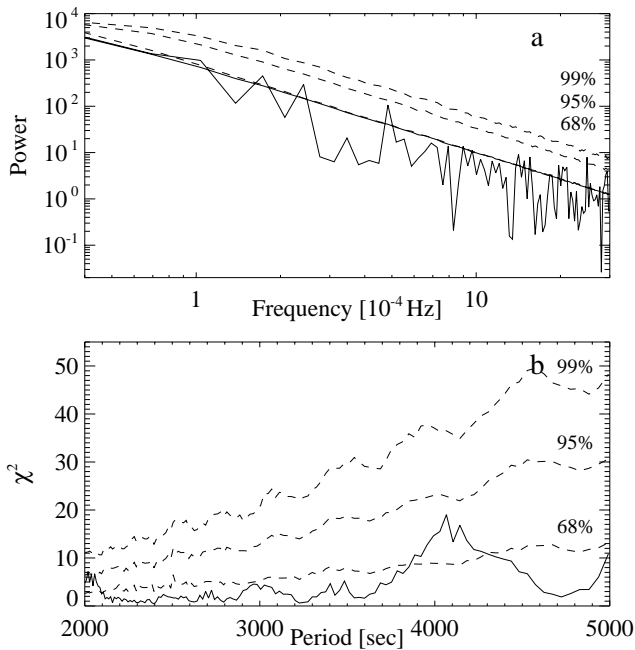
Figure 5.7: *(a)* PSD in Leahy et al. (1983) normalization and best power-law fit using the Done et al. (1992) method (continuous lines) and, *(b)* $\chi^2(P)$ curve (continuous line) of the *XMM* Mrk 766 light curve of Fig. 5.6. The set of dashed lines in both panels represent in ascending order the 68%, 95%, and for 99% "local significance" levels for a set of 5000 Monte Carlo red noise simulations with $\beta = 1.9$.

et al., 1999). Fig. 5.6 displays the resulting light curve.

5.2.2 Light curve analysis

We display the PSD and the $\chi^2(P)$ curves in Fig. 5.7 (the frequency range is 0.4×10^{-4} Hz to 30×10^{-4} Hz with 57 independent frequencies, the period range is 2000–5000 s with 132 test periods). A peak at a period of ~4200 s (corresponding to a frequency of ~ 2.5×10^{-4} Hz) that is consistent with the period claimed by Boller et al. (2001) is seen. In order to determine the significance of the peaks seen in Fig. 5.7, we computed significance levels using the methods outlined in section 4.2.

Before we can perform these simulations, we need to determine the shape of the PSD. For this purpose, we apply the "response method" of Done et al. (1992)
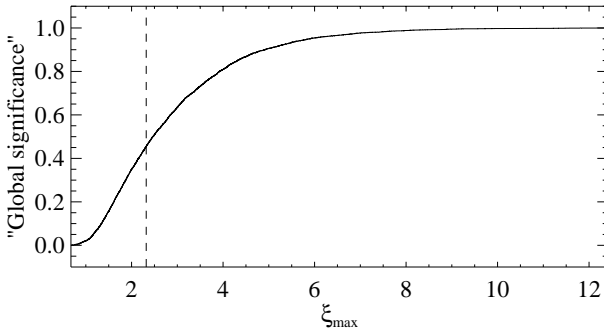
Figure 5.8: Probability distribution of the ξ_{max} values (see text for definition) from the 5000 red noise simulated light curves in the 2000–5000 s period range. The "global significance" indicates the probability of finding a light curve with a maximum peak with a value greater than the correspondent ξ_{max} value. The dashed line marks the position of the ξ_{max} value of the 4200 s feature in Mrk 766 in the 2000–5000 s period range. The "global significance" of this peak corresponds to a value of 45%.

and Green, McHardy & Done (1999) (see chapter 4) Varying the slope and normalization of the model periodogram, the best χ^2 fit gives a slope of $\beta = 1.9$, and a normalization determined by the variance of the original *XMM* light curve (χ^2/dof = 17.89/55). This low value indicates that the observed PSD is fully consistent with a power law and that no additional components, such as a QPO, are required.

Unfortunately, the short duration of the observation gives poor constraints on the PSD shape. Methods complementary to testing the consistency of the PSD with a power law should be used. We therefore simulated the desired 5000 light curves from a $f^{-1.9}$-PSD, with 29000 s of duration using a sampling interval of 100 s, a mean count rate $\mu = 9.15$ counts s^{-1}, a light curve variance $\sigma^2 = 2.46$ counts^2 s^{-2}. Examples of such simulated red noise light curves are shown in Fig. 4.1.

To obtain the "local significance" of the peak at ~4200 s , we calculated $\chi^2(P)$ and the PSD of each of the 5000 Monte Carlo realizations. For each trial period, we then computed the distribution of the $\chi^2(P)$ and PSD values at this trial period from all realizations. These distributions were used to determine the 99%, 95%, and 68% "local significance" levels using the method described in chapter 4.2. Our results are shown in Fig. 5.7. The peak at ~4200 s claimed as QPO by Boller et al. (2001) is below the 95% significance curve.

We also applied the "global significance" test to the Mrk 766 light curve for the period range from 2000 s to 5000 s. Fig. 5.8 shows the probability distribution of ξ_{max}, which corresponds to the probability of finding a red noise light curve with

a normalized maximum peak value less than or equal to the corresponding ξ_{max} value. For Mrk 766, the putative QPO peak lies at the 45% mark. In other words, ~50% of the simulated red noise light curves show peaks that are more significant than the peak observed in Mrk 766. We conclude that the observed 4200 s "QPO" in Mrk 766 may be an artifact of the red noise process and not the result of a physical process.

As we mentioned above, the value of β determined from the observations is rather uncertain. However, our result is independent of the specific value of β: Simulations with β values ranging from 1 to 2, i.e., over the typical β range seen in AGN, yielded similar results.

Conclusion: The "local significance" test based on this method shows that the 4200 s feature in Mrk 766 is not significant at the 95% level. This statement holds for both, PSD and $\chi^2(P)$ analysis (Fig. 5.7). The "global significance" of the 4200 s feature is 45%, i.e., higher peaks in the 2000–5000 s period range are found in roughly half of all simulated light curves. Thus, the presence of a peak in a red noise $\chi^2(P)$ or PSD is far from unusual. The 4200 s peak is attributable to a random occurrence due to the red noise character of AGN data.

CHAPTER 6

X-ray Binaries

The data bases from long-term X-ray scanning experiments, such as those obtained by *Vela 5B* (1969–1979), the All Sky Monitor on *Ariel 5* (1974-1980), the Burst and Transient Source Experiment (BATSE) aboard *CGRO* (1991–2000), and the All Sky Monitor (ASM) on *RXTE* (since 1996), have provided opportunities for studying long-term variations in cosmic X-ray sources. Long-term variability on time scales $\gtrsim 10$ d of galactic X-ray binaries is a widespread phenomenon. Such variations are the key in answering questions about the structure of accretion disks, the presence of third bodies, intrinsic variations due to changing mass accretion rates, and the nature of transient sources. Up to now, however, the cause for this variability remains unclear.

In some sources, such as Her X-1 or LMC X-4, the observed X-ray modulation is at a fairly constant frequency and is clearly due to a periodic covering of the X-ray source by a warped and precessing accretion disk. In these cases the geometry of the accretion disk is fairly well known, however, even here the physical reason for the warp and precession is unknown. Reasons that have been discussed are the torque exerted by X-ray driven accretion disk winds (Schandl & Meyer, 1994) or the free precession of the NS and the coupling of the neutron star magnetic field onto the inner regions of the accretion disk (Shakura et al., 1998). Others cite the strong radiation pressure from the central X-ray source onto the outer disk as the cause for the warping (Maloney, Begelman & Pringle, 1996; Maloney, Begelman & Nowak, 1998; Ogilvie & Dubus, 2001). In some sources, the long-term changes in the X-ray luminosity have been associated with state changes of the accretion disk, which are mainly due to a direct modulation of the mass accretion rate, $\dot{M}$ (Wilms et al., 2001). One way to modulate $\dot{M}$ would be the evaporation of the outer parts of the accretion disk via an X-ray driven wind (Begelman, McKee & Shields, 1983; Shields et al., 1986). Some other possible scenarios like mass transfer feedback, companion star precession, neutron star precession, or a triple system are explained in section 2.2.

In this chapter, I present results from a program aiming to study the long-time

behavior of a larger sample of X-ray binaries. Our goal is to identify observational signatures in order to constrain physical causes of the variability. Such a program has recently become feasible with the availability of data from the ASM on *RXTE* (Levine et al., 1996). This instrument has been monitoring the entire sky for X-ray sources since 1996 February.

The ASM light curves show a wide variety of phenomena. Different long-term behaviors such as stable and non stable periods, temporary periods or just stochastic behavior are present. I have collected a list of 27 low and high mass X-ray binaries (LMXB & HMXB) monitored with the ASM and studied their long-term variability. I present the detailed long-term variability study for six of these sources (Cyg X-1, Aql X-1, GX 339−4, 4U 1705−44, 4U 1957+115 and SMC X-1) and summarize the results of the other 21 sources.

6.1   RXTE/*ASM and data analysis*

The *RXTE*/ASM instrument consists of three Scanning Shadow Cameras (SSCs) mounted on a motorized rotation drive. Each SSC contains a position-sensitive proportional counter (PSPC) that views the sky through a slit mask. Each SSC is sensitive in the energy range of 1.3–12.2 keV, with on-axis effective areas of $\sim$10 cm^2, $\sim$30 cm^2, and $\sim$23 cm^2 at 2, 5, and 10 keV, respectively, and with a $6° \times 90°$ field of view (FWHM).

The ASM is operated so as to obtain series of 90 second exposures, called "dwells", during which the orientations of the SSCs remain fixed. The drive assembly rotates the structure holding the 3 SSCs every $6°$ for the dwells so that large portions of the sky are eventually scanned during each orbit of the spacecraft. Accessible sources are typically scanned 5 to 15 times over the course of a day. A more extensive description of the instrument and data analysis may be found in Levine et al. (1996).

Light curves in three energy bands — 1.3–3.0, 3.0–5.0, and 5.0–12.2 keV — as well as over the whole ASM band are publically available from the NASA Goddard Space Flight Center (GSFC) in the *RXTE* guest observer facility web site: `http://heasarc.gsfc.nasa.gov/docs/xte/xte_1st.html`. The "definitive one-dwell" data for solutions for which $\chi^2 < 1.2$ have been used in this work.

The time series analysis methods presented in chapter 3 have been applied to the ASM light curves with the purpose of characterizing the long-term variability behavior of each source. The data have been binned such that good statistics is achieved. In the case of period detection, the 68%, 90%, 95%, 99%, 99.9% significance levels (chapter 4.2) have also been determined from a simulation sample of 5000 white noise light curves. This temporal study is sometimes complemented

with a spectral analysis of the source comparing the light curves of the three ASM
energy bands.

During the analysis of the light curves some systematic periods can be present
due to sampling and background problems of the *RXTE*/ASM instrument. This
will be presented in detail section 6.1.1.

6.1.1   Instrumental effects

Special care should be taken in the search for periodicities with the ASM light
curves, since some systematic periods can be present in the data. This kind of
systematic periods are not necessarily always present in each ASM data set. The
influence of such a contamination depends on the long time behavior of the light
curve and/or on the angular distance between the corresponding object and the
Sun.

On the one hand, the data can be contaminated by a periodic signal that is gen-
erated by passages through the South Atlantic Anomaly (SAA), due to the strong
modulation in the background at this period. The expected values of such artifi-
cially induced periods are in the range of 1 year. Also, a peculiar signature with
a period of around 180 days (which corresponds to 1/2 years) can be found in
the ASM light curves. Comparing each individual light curve with the sampling
modulation of the angular distance between the object and the sun, it is some-
time possible to find, just with the naked eye, a relation between the flux and this
angular distance. Fitting a sinusoid to the data, we found that both sinusoidal
curves (the fit and the sinusoidal shape of the Sun angular distance curve) are
often anti-correlated (shifted by a phase of 0.5), and in these cases the modula-
tion around 180 days is also present in the periodogram analysis (see the case of
1E 1740.7−2942 in section 6.8, other examples are also present in this section).
Some ASM background model affected by the X-ray radiation from the Sun back
scattered from the Earth might be responsible to this feature. Similar trends show
up on year time scales usually on sources with secular drifts (with time scale of
years), combined with sampling modulations (P =365 d) caused by the sun cross-
ing near the source position (Remillard, priv. comm.). If the trend lasts over all
the ASM history, 8 years until now, then one usually sees a false period in the
higher-frequency beat, i.e., by $f = 1/365$ days $\pm$ 1/8 years. If the time trend has
short-lived ramp, false features can be founded at $f \sim 1/365$ days $\pm$ 1/time trend.

Furthermore, due to the monitoring pointing of the satellite, some sampling pat-
tern can occur repetitively each day, producing the appearance of a period around
24 hours in the data. Having a long-term secular trend in the light curve, produces
the appearance of a false period at 24 hours $+\delta$, where δ is something reasonably
small, i.e. $\delta \sim 24$ hours$/T$ where T is the time scale of the long-term trend. This
is an artifact produced by a beating between the sampling period of the satellite

and the secular trend in the light curve (Remillard, priv. comm.). See section 6.4, the case of GX 339-4, for a example which shows such effect.

6.2 Cyg X-1

The black hole candidate Cyg X-1 is one of the brightest X-ray sources in the sky at energies > 20 keV. It consists of a compact object orbiting the blue supergiant star HDE 226868, with an orbital period of 5.6 days (Brocksopp et al., 1999). The supergiant is thought to emit a stellar wind, as is typical for high-mass stars. The X-ray properties of Cyg X-1 have been considered as canonical signatures of black hole candidates. Especially important are the source X-ray transitions from the low/hard state via the intermediate state into the high/soft state. Two different behaviors in the hard state have been observed, a "quiet hard state" and a "flaring hard state" characterized by the presence of frequent intermittent X-ray flares. Pottschmidt et al. (2003) interpret these flares as "failed" transitions from the hard to the soft state, where the transition is stopped before the soft state is reached, and called it "failed state transitions". It has been noted by Özdemir & Demircan (2001) that the long-term periodicities of the source are seen to be distorted by the presence of the high/soft state and failed state transitions.

Previous studies of the long-term variablity of Cyg X-1 have shown several long periods:

- A period of 294 days was proposed by Priedhorsky, Terrell & Holt (1983) based on the *Vela 5B* (3–12 keV) and *Ariel 5* (3–6 keV) X-ray data covering a period of 11 years between 1969 and 1980. It was also confirmed in the optical region (Kemp et al., 1983, 1987). The period was attributed either to the precession of the accretion disk or to a third body orbiting around the system.

- Kemp et al. (1983) showed a strong modulation in their optical PSD of about 425 days with no outstanding counterpart in the X-ray power spectra. Using X-ray data from *Ginga*/ASM Kitamoto et al. (2000) reported a broad peak around 200–250 days and pointed out that the highest point (207 days) in this broad peak is approximately half the modulation founded by Kemp et al. (1983). The cause of this long-term periodicity was not discussed.

- Results of UBV observations from Lyutyi (1985) between 1975–1982 revealed a period of ~79 (or 39.5 days), but these periods were not confirmed (Kemp et al., 1987).

- More recent measurements, based on 20 months of radio emission starting
  at 1996, found a 150 day signature associated loosely with the soft X-ray
  flux (Pooley, Fender & Brocksopp, 1999). Multiwavelenght (optical, radio,
  and hard and soft X-ray) observations between 1996 and 1998 by Brock-
  sopp et al. (1999) confirmed the presence of this modulation, which they
  suggest is caused by precession and/or radiative warping of the accretion
  disk. Kitamoto et al. (2000) found also the presence of a ~150 day peri-
  odicity by using *Ginga*/ASM data obtained between 1987 and 1991. The
  most recent evidence for the 150 day period has been presented by Özdemir
  & Demircan (2001) by analyzing *RXTE*/ASM data between 1996 and 1999.
  To avoid the distortion of the periodicities in the original data introduced by
  the high/soft state and the failed state counts, they truncate visually the light
  curve at 30 cps.

Here we perform a similar analysis as Özdemir & Demircan (2001) of the
RXTE/ASM light curve, excluding data from the high/soft state and failed state
transitions, taking a definition of the spectral states based on the spectral and tim-
ing characteristics of the data obtained by *RXTE*/PCA.

On the basis of the variability from the *RXTE*/ASM light curve, Zdziarski et al.
(2002) discerned three main spectral states. Using the definition of a photon
power-law index, Γ, based on the ratio of the energy fluxes in the power-law spec-
trum, they classified the states under the conditions $\Gamma_{(3-12\,\text{keV})} > 2.4$ for the soft
state, < 2.1 for the hard state, and $\Gamma_{(3-12\,\text{keV})} = 2.1 - 2.4$ for an intermediate state.

In our analysis, we use the ASM data range from November 1997 to July 2001,
where the variability properties of Cyg X-1 are well understood, permitting us
a good determination of the spectral state of the source. Our time interval cor-
responds to the *RXTE*/PCA monitoring time range used by Pottschmidt et al.
(2003), who analyzed the variability properties of Cyg X-1 described in terms
of the power spectral density, the Fourier-frequency dependent X-ray time lags,
and the parameters of a simple spectral model based on a power-law plus a multi-
temperature disk-black body component. They analyzed data obtained with the
PCA during several pointed *RXTE* observation programs between 1997 and 2001.
We use the values of the time lags and the photon index to determine the state
status of the source. The time lags from Pottschmidt et al. (2003) were deter-
mined between the 2–4 keV and 8–13 keV ranges, averaged over the 3.2–10 Hz
frequency band. The photon index, Γ, corresponds to the power-law component
of the X-ray photon spectrum model in the energy rage of 2–20 keV. We interpo-
late the fit parameter values obtained from this PCA pointed observations within
the time range from the ASM light curve between December 10, 1997 and July
13, 2001, corresponding to MJD 50793.244 and 52103.849. We then define the
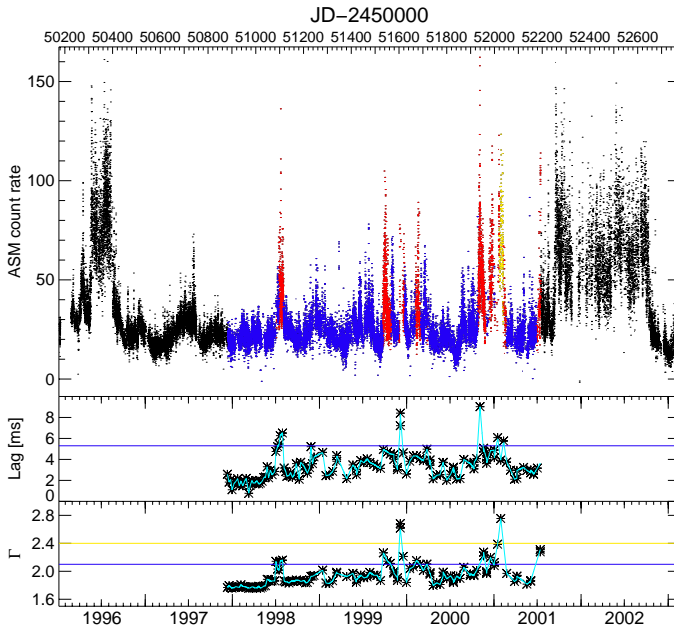
Figure 6.1: Cyg X-1 ASM light curve and temporal variability of the source using the photon index and X-ray time lag fit-parameters from Pottschmidt et al. (2003). The colors represent the different states of the source: yellow corresponds to the soft state, red to the failed state transitions and blue to the hard state. The horizontal lines in the lower panels represent the thresholds of the state status criteria (see text).

states by the conditions

$$
\begin{cases}
\text{soft state} = \Gamma > 2.4 \quad \text{and} \quad \text{lag} < 5.3\,\text{ms} \\
\text{failed state transition} = 2.1 \leq \Gamma \geq 2.4 \quad \text{and} \quad \text{lag} \geq 5.3\,\text{ms} \\
\text{hard state} = \Gamma < 2.1
\end{cases}
\tag{6.1}
$$

The upper panel of Fig. 6.1 represents all the *RXTE* history of the 1.3–12.2 keV ASM light curve. The analyzed ranges are plotted in colors; yellow corresponds to the high/soft state, red to the failed state transitions and blue to the hard state. Cyg X-1 spends most of its life in the low/hard state as indicated by the high density of blue points. In the lower panels of Fig. 6.1 the photon index and the
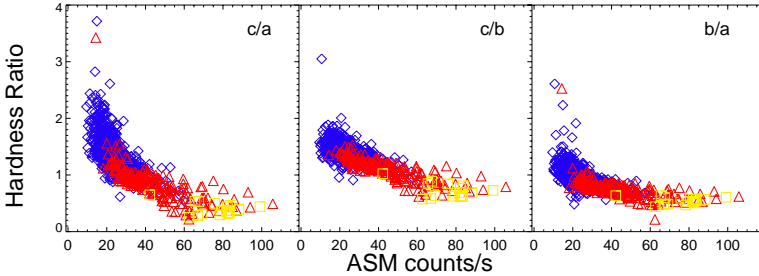
Figure 6.2: ASM color-intensity diagram as the hardness ratio versus the ASM intensity range (1.2–12.2 keV). The hardness ratios are defined as c/a, c/b, and b/a, where $a = (1.3–3.0\,keV)$, $b = (3.0–5.0\,keV)$, and $c = (5.0–12.2\,keV)$ are the different energy bands of the ASM color light curves. The symbols and colors represent the different states of the source: yellow square corresponds to the soft state, red triangles to the failed state transitions and blue diamonds to the hard state.

time lag values taken from Pottschmidt et al. (2003) are plotted.

We produced three hardness ratios by dividing the intensity of the different bands of the ASM data in the following way: c/a, c/b, and b/a, being $a = (1.3 − 3.0\,keV)$, $b = (3.0 − 5.0\,keV)$, and $c = (5.0 − 12.2\,keV)$ the ASM color light curves. Color-intensity diagrams, Fig. 6.2, are obtained by plotting the hardness ratios versus the total intensity band (1.3–12.2 keV) of ASM. The different states are clearly separated in the hardness ratio versus intensity diagram. During the periods of high count rate the spectra become softer and the source moves to the lower right bottom of the color-intensity diagrams, whereas as the intensity decreases the spectra becomes harder and the source moves to the left upper bottom.

A PSD for all the ASM energy range is plotted in Fig. 6.3, as well as the PSD of the different energy bands of ASM. For the hard state data (blue light curve in Fig. 6.1) the PSD is plotted in Fig. 6.4.

The periodogram of the 7 day binned light curve contains a broad peak above the 99.9% FAP level at ~420 days (see Fig. 6.3). This peak is distorted by "failed state transitions", as can be seen when the "failed state transitions" are removed (Fig. 6.4). The periodogram of the truncated data shows the strongest peak at ~150 days and also a clearly less significant ~400 day peak. The 294 day modulation reported previously (Priedhorsky, Terrell & Holt, 1983) is not present in the Lomb-Scargle periodogram from the hard state data, however, it is seen when epoch-folding the data (Fig. 6.5). The ~294 day modulation may be a sideband of the ~150 day period. Also a modulation in the form of a broad peak between
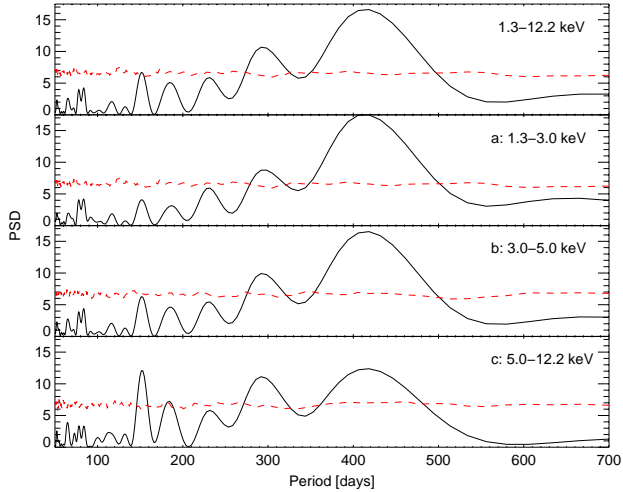
Figure 6.3: PSD from the ASM Cyg X-1 data corresponding to the PCA monitoring time range indicated in Fig. 6.1 (see text for explanations). It has been calculated for the different ASM energy ranges. The red dashed lines represent the 99.9% "local significance" levels for a set of 5000 Monte Carlo white noise simulations.
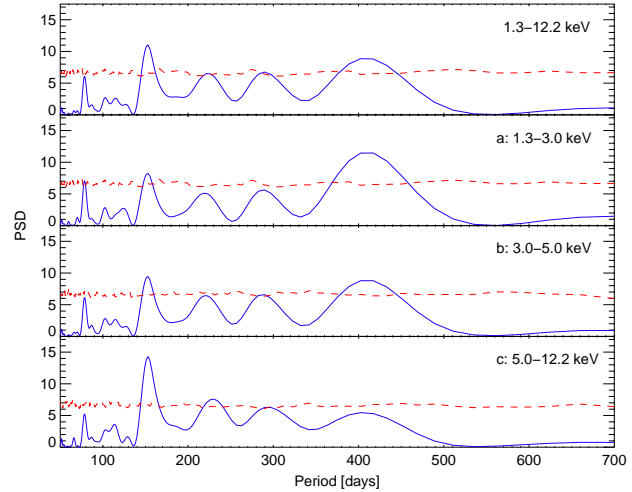
Figure 6.4: The same as Fig. 6.3 but only for the hard state of Cyg X (see text for a definition of hard state)
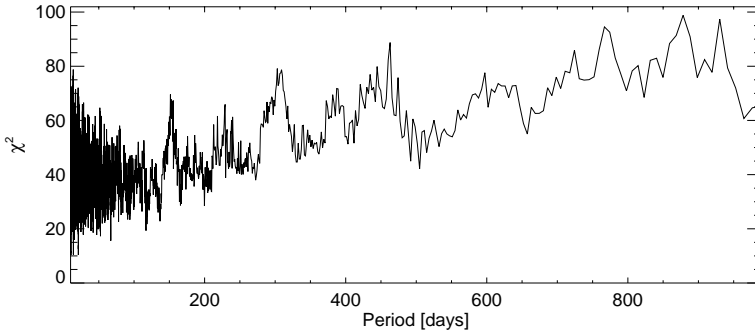
Figure 6.5: Epoch-folding from the hard state of Cyg X-1.
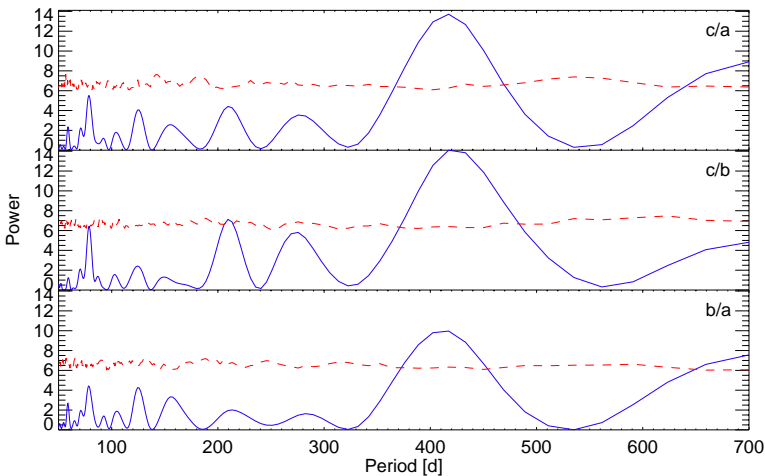
Figure 6.6: PSD from the hard state of Cyg X-1 hardness ratios defined as c/a, c/b, and b/a, where $a = (1.3 - 3.0\,\mathrm{keV})$, $b = (3.0 - 5.0\,\mathrm{keV})$, and $c = (5.0 - 12.2\,\mathrm{keV})$ are the different energy bands of the ASM color light curves. The red dashed lines represent the 99.9% "local significance" levels for a set of 5000 Monte Carlo white noise simulations.

200–250 days is seen in all the cases, but become only slightly significant in the PSD of the hard state data in the energy range 5.0–12.2 keV.

Note that the PSD of the hardness ratio present in Fig. 6.6 shows also a broad significant peak around ~420 days, and no peak at 150 or 300 days. That could be evidence that the 150 day period corresponds to intensity variations of the source
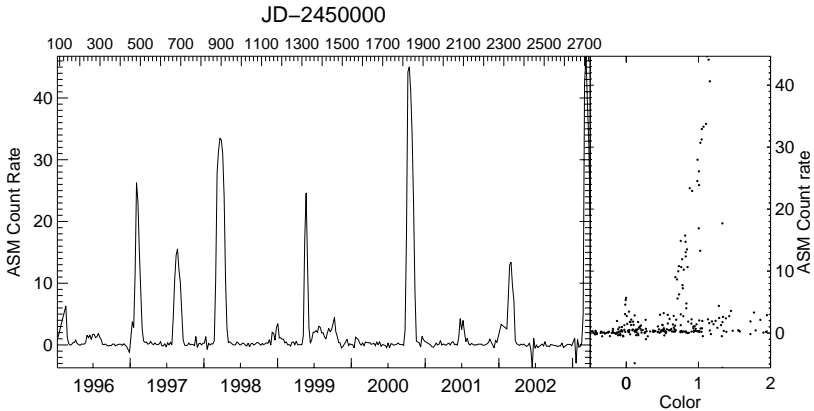
Figure 6.7: *Left*: 15 day binning ASM light curve of Aql X-1. *Right*: The correlation of the 5.0-12.2 keV/1.3-3.0 keV count rate ratio with the total ASM count rate.

flux and the ~420 day modulation to spectral variations which should link together with the failed spectral transitions. There is not enough statistics to confirm this hypothesis, due to the short duration of the studied light curve. More data will be needed to study the variability of the state transitions. A period on the ~150 day time scale is probably due to precession and/or radiative warping of an accretion disk, as suggested by Brocksopp et al. (1999).

6.3 Aql X-1

Aql X-1 is a soft X-ray transient (SXT) LMXB that shows regular X-ray outbursts (see Fig. 6.7). It is believed to contain a neutron star as indicated by its type I X-ray burst (Czerny, Czerny & Grindlay, 1987). From the observed 549 Hz oscillations of X-ray flux during one of its X-ray burst, its NS is believed to be spinning at a period of either 1.8 or 3.6 ms (Zhang et al., 1998). The strength of its magnetic field is believed to be quite weak, as inferred from the lack of any detectable pulsed X-ray flux in its persistent emission (Zhang, Yu & Zhang, 1998, and references therein). Aql X-1 was recently classified as an atoll source (Reig et al., 2000). The secondary star V1333 Aql of spectral type K6−M0 is likely to fill its Roche-lobe. The system is located at an estimated distance of 4–6.4 kpc. The orbital period is ~19 hr (Chevalier & Ilovaisky, 1991).

Aql X-1 has been observed to exhibit three types of X-ray spectral states. Close to the outburst maximum, the X-ray spectrum is soft. Sporadic observations dur-

ing the early part of the outburst decay showed that when the luminosity drops below $\sim 10^{36}$ ergs s^{-1}, the spectrum changes to a much harder power-law component. In the quiescence at a level of $\sim 10^{33}$ ergs s^{-1}, the spectrum is considerably softer and again dominated by the blackbody component. Usually the source is in its quiescent state. The X-ray burst source Aql X-1 displays X-ray variability on all time scale. Within intervals of months to years, it shows long-term outbursts which have an unstable periodicity with recurrent periods of 125 and 309 days. The outbursts of Aql X-1 are generally characterized by a fast rise (5–10 days), followed by a slow decay (30–70 days). The outbursts of the SXTs are suggested to be due to the thermal instability in the accretion disk, similar to that in dwarf novae (van Paradijs, 1996). The conditions in the disk of the SXT are affected by the presence of the central source (the neutron star in Aql X-1), which acts as an irradiating source during outburst and modifies the disk structure.

Several long-term studies have been done for this source:

- Priedhorsky & Terrell (1984b) analyzed data obtained by the 3–12 keV detector on the *Vela 5B* satellite covering 1969 and 1976. The seven outbursts from 1969 to 1975 had a mean separation of 426±117 days. Time series analysis suggested an underlying cycle of 122–125 days for the non-regular eruptions. The mayor outbursts were observed at separations of 2, 3, 4, or 6 times the fundamental cycle. They interpreted the 122–125 day time scale as a disk precession cycle (precession due to the precession of a tilted disk), by analogy to Her X-1. The outbursts were proposed to be most likely caused by an episode of enhanced accretion onto the compact object. They argued that an outburst commences if the critical density threshold to cause a disk instability would be exceeded when the mass transfer rate to the disk is near maximum for a periodically modulated mass transfer rate due to some type of mechanism. The mass transfer rate could be modulated by intrinsic activity in the companion star, or perhaps be gated by the changing aspect of a precessing accretion disk.

- Kitamoto et al. (1993) presented the results of the periodicity analysis of 4.5 yr (1987–1991) of data observed with the ASM on-board *Ginga* and of 10 yr (1969–1979) of data accumulated by the *Vela 5B* satellite. They found a long-term outburst periodicity of 309 days with the *Vela* data set, which was not observed by the *Ginga* data set. However, with this last data set they confirm the 125 day fundamental cycle founded by (Priedhorsky & Terrell, 1984b). They conclude that the mechanism for the Aql X-1 outburst was not related to some rigid periodic mechanism such as orbital motion or precession; the flaring event must be related to some unstable periodic mechanisms. As candidates for the unstable periodic phenomenon they
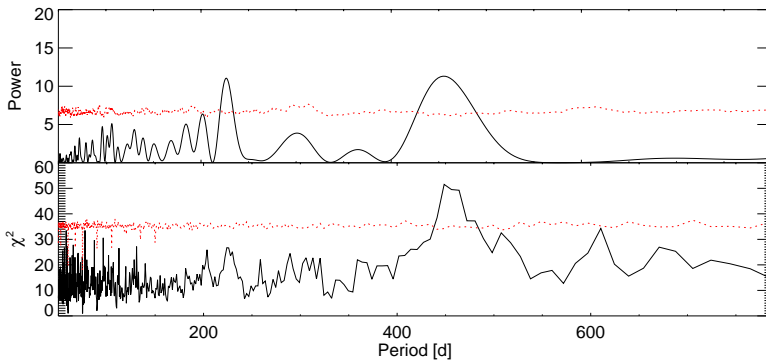
Figure 6.8: *Top*: Lomb-Scargle periodogram of the ASM Aql X-1 light curve. *Bottom*: epoch-folding periodogram. The red dashed lines represent the 99.9% "local significance" levels for a set of 5000 Monte Carlo white noise simulations.

proposed some type of activity associated with the companion star or an accretion disk instability. Furthermore they observed a linear relationship between both the peak intensity and the total energy of the flare and the time since the start of the previous flare, which was consistent with the release from a draining reservoir of an accretion disk.

- Shahbaz et al. (1998) found a delay between the IR and X-ray rise times, and interpreted this as the signature of an "outside-in" outburst, in which a thermal instability in the outer disk propagates inward. They suggested that an ADAF region was created at the end of the previous outburst. This ADAF region would appear as a hole in the inner accretion disk, thereby causing the X-ray–IR delay when the system starts its next outburst.

- Recently Šimon (2002) presented an analysis of the long-term activity of Aql X-1 with data from the period 1996–2001 observed with the ASM on board *RXTE*. Using the method of $O - C$ residuals, they resolved that variation on the recurrence time are large, but generally not chaotic. The prevailing value is 211 days but the evolution of the recurrence time showed several large jumps. Although the respective outbursts differ in both their duration and the maximum intensity, their rising and decay branches display notable similarities. The rising branches are exponential. The slope of the decay is broken in some events, with the final phase having a steeper slope and being roughly linear. They argued that just the inner disk is irradiated during outburst and that viscous heating plays a big role and discuss

the observed outbursts in terms of the thermal instability model.

Using all the available ASM data from 1996 to 2003 May, we find a time scale of ~226 days (see Fig. 6.8) which might be consistent with the underlying period of Priedhorsky & Terrell (1984b) (since $2 \times 122 \simeq 226$). A modulation of about 450 days (equivalent to the 436 days of Priedhorsky & Terrell, 1984b) is also present (see the broad peak in both panels of Fig. 6.8). The correlation of the 5.0–12.2 keV/1.3–3.0 keV X-ray color with the total ASM count rate (Fig. 6.7, right panel) hints at a hardening of the X-ray spectrum as the system declines into quiescence. A possible interpretation for this spectral behavior and the outbursts is a thermal instability in the outer disk which propagates inward (Shahbaz et al., 1998).

6.4   GX 339−4

Although one of the earliest proposed black hole candidates (Samimi et al., 1979), GX 339−4 remains one of the most inaccessible objects to direct measurement of system parameters because of a higher level of X-ray activity; even when the X-rays are at their faintest, the companion star remains undetectable. The emission all the way from radio through gamma-ray wavelengths is probably completely dominated by the accretion flow and it shows strong correlations between the energy bands. Its black hole candidacy is established by its Cyg X-1-like X-ray variability and multiple states. It has been observed in the soft/high, hard/low, off (which is considered to be a weak low state), quiescent, and very high X-ray states. It is an unusually "steady" low-mass X-ray binary since it is almost always X-ray active spending most of the time in the low/hard state like a faint persistent source. At present, there is only a indirect estimation of the dynamical mass of ~5.8 $M_\odot$ (Hynes et al., 2003), which also supports the black hole candidacy. The source exhibits aperiodic and quasi-periodic modulations on time scales spanning milliseconds to years, and over a wide range of wavelengths.

Several orbital periods have been proposed on the basis of both photometric and spectroscopic observations; Corbet et al. (1987) estimated a $P_{orb} > 0.5$ d during the high state in 1984–1986, Callanan et al. (1992) proposed 0.62 d during the low state in 1987, Soria, Wu & Johnston (1998) suggested twice the period of 14.8 hours during the high state in 1998, and Cowley & Schmidtke (2002) proposed a period of 0.7 d during the low state in 1999. Recently Hynes et al. (2003) report the detection of sharp N III emission components associated with the irradiated companion star and yielded the estimate of a new orbital period of ~1.7 d.

In the search of a trace of the orbital period in the ASM light curve we first
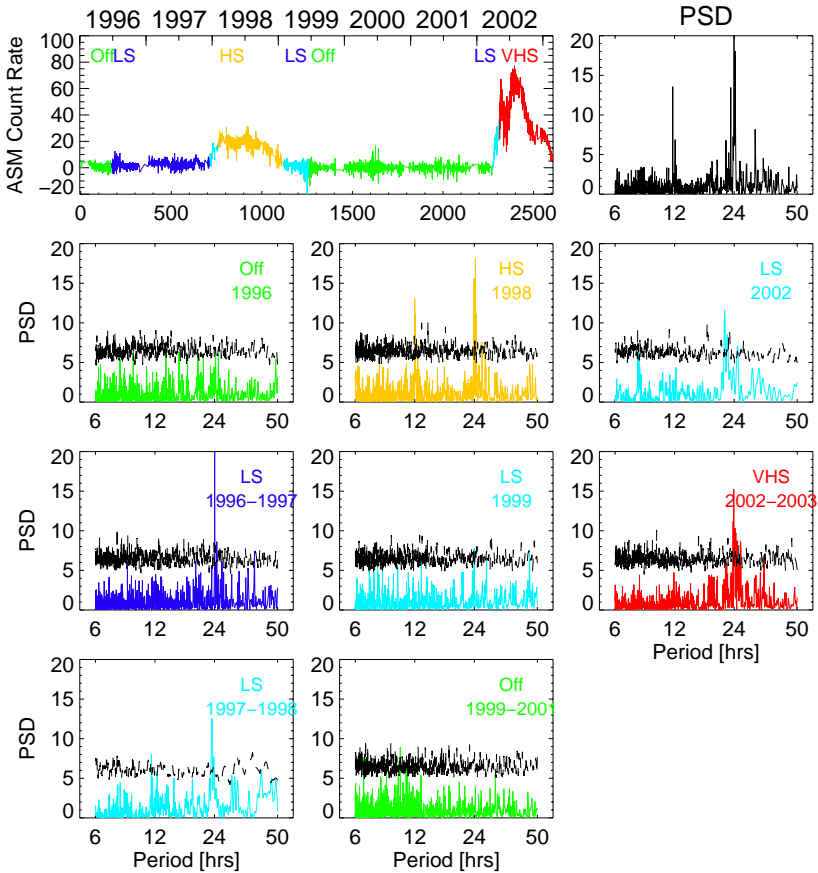
Figure 6.9: *Upper panel:* ASM GX 339−4 light curve with a resolution of 15 min on the left (the time units are presented in days on the lower axis and in years on the upper axis) and the corresponding PSD of all the light curve on the right side. *Lower panels:* individual PSDs during each spectral state, as represented by different colors: green: off state (Off), blue: low state (LS), cyan: also low state, but between transitions from low to high and vice-versa, orange: high state (HS), and red: very high state (VHS). The black curves represent the 99.9% "local significance" levels for a set of 5000 Monte Carlo white noise simulations.

binned the light curve with a resolution of 15 minutes and analyzed all the data and the data of each spectral state separately. Excluding the off states, a peak around 24 hours is clearly present in all the PSDs (see Fig. 6.9). The significance
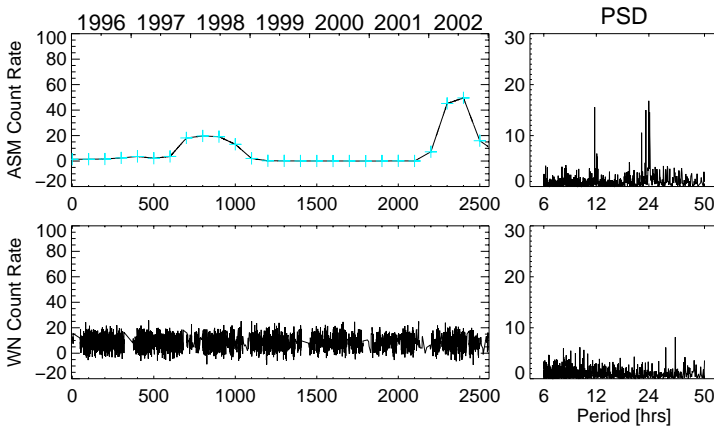
Figure 6.10: *Upper panels*: smoothed ASM GX 339−4 light curve derived from the original ASM GX 339−4 light curve with a resolution time of 240 days (blue crosses), by interpolating between points (black line) to obtain the same sampling pattern as with 15 minutes resolution and the corresponding PSD . *Lower panels*: simulated white noise light curve with a resolution of 15 min and the same sampling as the ASM GX 339−4 light curve, and the corresponding PSD.

of this peak is > 99.9% under the assumption of a dominantly underlying white noise process in the light curve. We were at first alerted and thought to have found a period in the light curve associated with all spectral states of the sources except in the off state (which represents a no or very weak detection of the source). But an in-depth study of the light curve have shown that this 24 hours modulation represents, in fact, the beating between the sampling pattern and the long-term secular trend of the light curve, and not a real period in the GX 339−4 light curve. This modulation comes from the fact that *RXTE* does a lot of daily monitoring, as explained in section 6.1.1.

To check this fact, we first created a smoothed version of the ASM light curve binning the original light curve with a resolution of 240 days. Simulated light curves were created based on this smoothed version with the same sampling as the original light curve, interpolating between points of the smoothed light curve to obtain the same sampling pattern and resolution as the 15 min resolution ASM light curve in Fig. 6.9. See the resulting smoothed light curve in Fig. 6.10 upper panel. We then performed the same period search analysis as in the original light curve. A peak is also present at 24 hours in the PSD of the smoothed light curve (left side in upper panel of Fig. 6.10). That is a telling sign that this modulation is
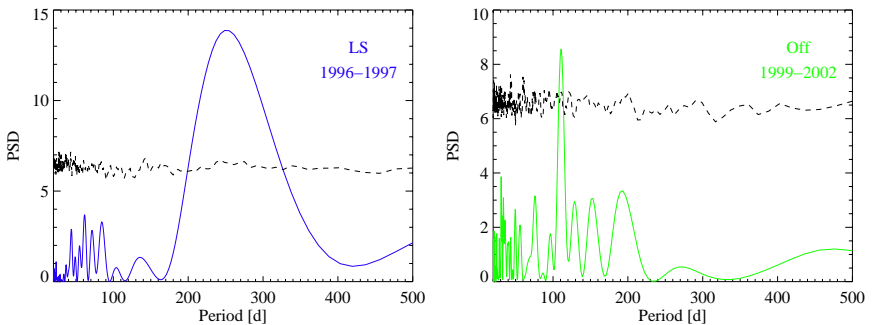
Figure 6.11: PSD of the ASM GX 339−4 light curve with a resolution of 7 days for the LS between 1996 and 1997 at the left panel and the Off state from 1999–2002 at the right panel. The black curves represent the 99.9% "local significance" levels for a set of 5000 Monte Carlo white noise simulations.

an alias of the sampling pattern. In this plot we also show a simulated white noise light curve with the same sampling as the 15 min resolution ASM light curve and the corresponding period search analysis (see Fig. 6.10, lower panels). Although the simulated light curve has the same sampling pattern as the original light curve, this PSD does not show the modulation. This can be explained due to the absence of a long-term trend in the white noise light curve. In the case of the power in the periodogram is shifted from low to high frequencies. In the case of white noise, it is a flat periodogram, and shifting power from the low frequencies to the sampling period does not have an effect on the shape of the periodogram (which will remain flat). Significant power at low frequencies is needed to be shifted into the sampling period, so only light curves with long-term secular trends will clearly show the sampling period. That explains why the period was not present in the PSD of the off state of the source (see Fig. 6.9) which can be represented as a white noise process.

On long time scales from months to years, GX 339−4 shows a broad 240 day modulation considered as a characteristic time scale (Nowak, Wilms & Dove, 1999; Kong et al., 2002). This modulation is present in the ASM data from the LS between 1996 and 1997 (Fig. 6.11, left). Including the flat-topped HS from 1998 or the last VHS in the periodogram analysis would dominate the PSD and mask the 240 day peak. Analyzing the long Off state from 1999 to the start of 2002 a weak but significant peak is present in the PSD at ~120 days, which is half of the 240 day characteristic time scale (Fig. 6.11, right). This period could be an alias of the 240 day characteristic time scale.

The observed time scale is comparable to that expected from radiation pressure-

driven warping instability (Pringle, 1996). But a pure warped, precessing disk model would invoke only inclination angle effects, and that is unlikely be the case for GX 339−4 due to his low inclination (it must lie below 60°, Cowley & Schmidtke, 2002). As noted by Nowak, Wilms & Dove (1999), the observed long-term variability of GX 339−4 could be due to a combination of a quasi-steadily precessing disk at large radii with coronal structure changes on small radii. If this is the case, X-ray irradiation can give rise to a precessing disk as mentioned by Kong et al. (2002), and it might even explain the LS/HS transition of the source. Therefore, it is possible that such quasi-periodic oscillation might actually be a characteristic precursor to the LS/HS transition.

6.5   4U 1957+115

The LMXB 4U 1957+11 is one of the less well studied possible black hole candidates even though the nature of the compact object is still not entirely clear. Evidence for 117, 235 and 352 day periods has been reported by Nowak & Wilms (1999), where the ASM data available until 1998 November were analyzed. Analysis of all ASM data until 2000 May (Benlloch et al., 2001c) revealed other features in the periodogram, in which a strong peak at ∼194 days and a double peak at ∼280 days were present. Wijnands, Miller & van der Klis (2002) used all the ASM data available until 2001 January, and showed multiple peaks above 100 days present in the Lomb-Scargle diagram. The most significant peak was the one at 250–260. Looking at the Lomb-Scargle diagrams obtained by Nowak & Wilms (1999) and Wijnands, Miller & van der Klis (2002), and the dynamical periodogram (Fig. 6.12, Upper left panel) we find evidence for a possible change of the period from ∼300 days at the start of the ASM mission to ∼250 days. Two other significant periods are also present in the data, one at ∼190 days, and a predominant one in the last years of ∼133 days. This last period is consistent with that presented by Nowak & Wilms (1999) in the first years of the ASM light curve. All these results strongly suggest that the long-term variability behavior of 4U 1957−11 is much more complicated than one simple period, and furthermore, no completely stable periods are present in the system.

In the color light curve defined as the ratio between the 5–12.2 keV and the 1.3–3.0 keV ASM band (see Fig. 6.13) a period of ∼194 days is present. The softening of the ASM light curve at a period of ∼2 × 194 days support the geometrical model presented by Nowak & Wilms (1999) in which inclination effects due to a precessing accretion disk are the cause for the long-term variability. In this model, during the softening phases, a central, point-like corona responsible for the hard flux is hidden by the outer parts of the disk. We note, however, that the orbital
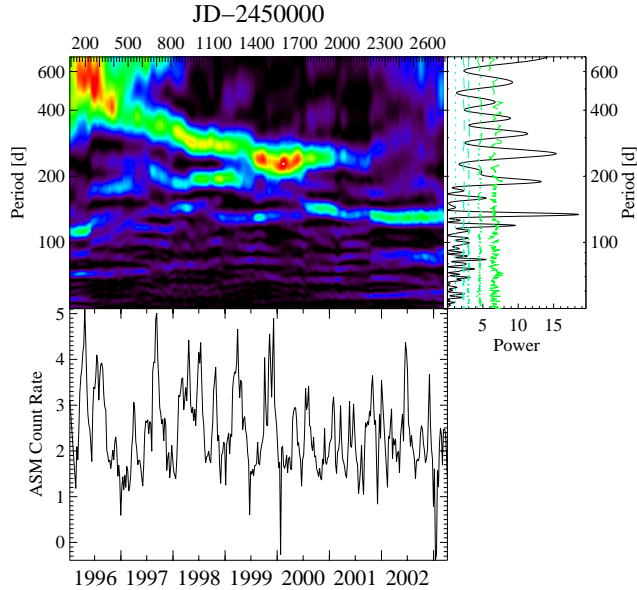
Figure 6.12: *Upper left*: Dynamical periodogram of 4U 1957+115. *Upper right*: Lomb-Scargle periodogram. The set of dashed lines represent in ascending order the 68%, 90%, 95%, 99%, and 99.9% "local significance" levels for a set of 5000 Monte Carlo white noise simulations. *Lower left*: ASM light curve.
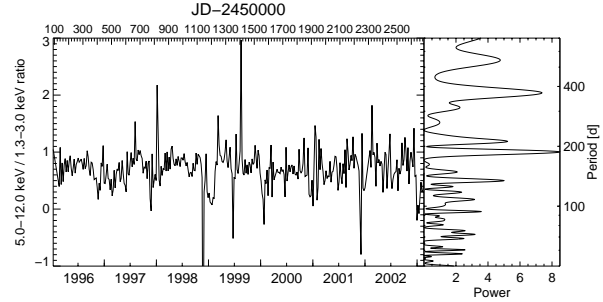

Figure 6.13: *Left*: Color light curve of 4U 1957+115 defined as the ratio between the 5–12.2 keV and the 1.3–3.0 keV ASM count rate. *Right*: Lomb-Scargle periodogram of the color light curve.

parameters for 4U 1957+11 place the source in a regime where a strong warp of the disk is difficult to maintain (Ogilvie & Dubus, 2001). On the other hand, based on *RXTE*/PCA spectral data, Wijnands, Miller & van der Klis (2002) suggested that the long-term variability of the source is most likely due to variations in the mass accretion rate onto the compact object, and not due to a precessing accretion disk.

6.6   SMC X-1

The eclipsing binary pulsar SMC X-1 is a massive X-ray binary system with an orbital period of 3.89 days decaying on a time scale of 10^5 yr (Levine et al., 1993). A high-low state variation with a quasi-periodic cycle of ~60 days was first reported by Gruber & Rothschild (1984) after a series of observations with *HEAO 1* during 1977–1978. This variation was confirmed in the long-term monitoring data from the *RXTE* and *CGRO* observatories (Zhang et al., 1996; Wojdowski et al., 1998; Clarkson et al., 2003a; Ribó et al., 2000), and was also noted that it was not steadily, varying between 50 and 60 days. The superorbital period is believed to be the consequence of a precessing, warped accretion disk. This disk is presumed to periodically occult the X-rays from the central source, thereby creating a modulation in the X-ray light curve. Wojdowski et al. (1998) argued that no intrinsic source variations could be responsible for the 60 day modulation, and they showed that periodic occultation of the pulsar by the rim of a warped accretion disk, precessing under the gravity of the giant companion was consistent with the observations. Ribó et al. (2000) suggested that the variation of the superorbital period might itself be periodic. The dynamical power spectra in Fig. 6.14 shows the 40–60 day variations. As noted by Clarkson et al. (2003a), it seems to vary in a coherent, apparently almost sinusoidal way (see Fig. 6.15), although the ASM light curve is statistically not long enough to confirm this hypothesis. Clarkson et al. (2003a) confirmed that the precessing, warped accretion disk must be responsible for the superorbital variations, and suggested that the influence of the warp may be felt not only through varying occultation, but through varying accretion at the neutron star boundary layer, permitted because the disk precession is not steady but quasi-steady. An interaction of warping modes can then give rise to the varying superorbital period.

It is interesting to note that the characteristic frequency of the variability, i.e., the peak of the wavelet decomposition, correlates with the source flux. This correlation is seen, e.g., in Fig. 6.15, where we plot the wavelet decomposition in frequency space with the ASM source flux (determined from 315 d long light curves). Such a behavior is reminiscent of the correlation of the time variation of
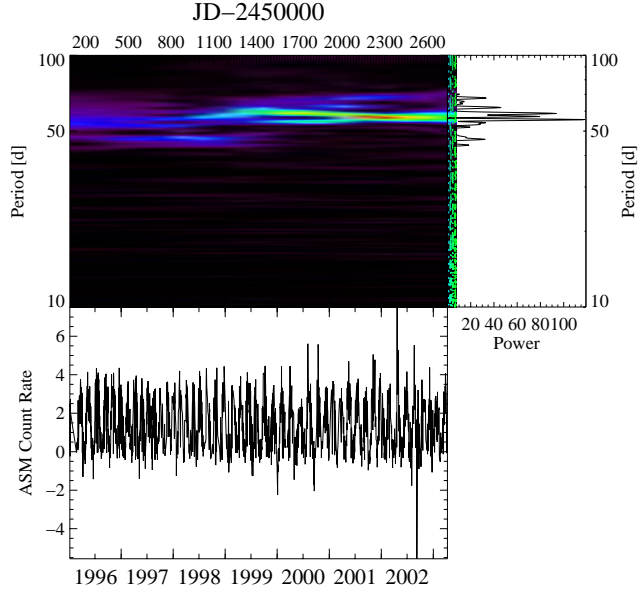
Figure 6.14: *Upper left*: Dynamical periodogram of SMC X-1. *Upper Right*: Lomb-Scargle periodogram. The set of dashed lines represent in ascending order the 68%, 90%, 95%, 99%, and 99.9% "local significance" levels for a set of 5000 Monte Carlo white noise simulations. Lower left: ASM light curve.
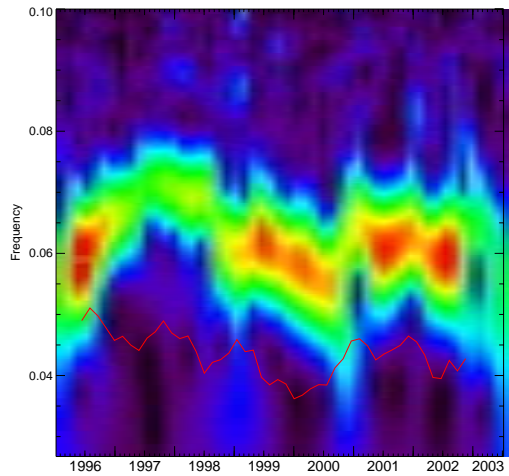

Figure 6.15: SMC X-1 Wavelet diagram. The red line represents the ASM source flux (determined from 315 d long light curves) scaled by a factor of 0.03.

the 35 d turn-on period in Her X-1 with source flux (Staubert, Schandl & Wilms, 2000). It is likely that the increased source flux corresponds to an increased mass accretion rate, $\dot{M}$. The correlation between the X-ray flux and the disk precession thus implies that increased mass accretion rates (i.e., an increased overall mass of the accretion disk) lead to an increase of the accretion disk precession frequency.

6.7   4U 1705−440
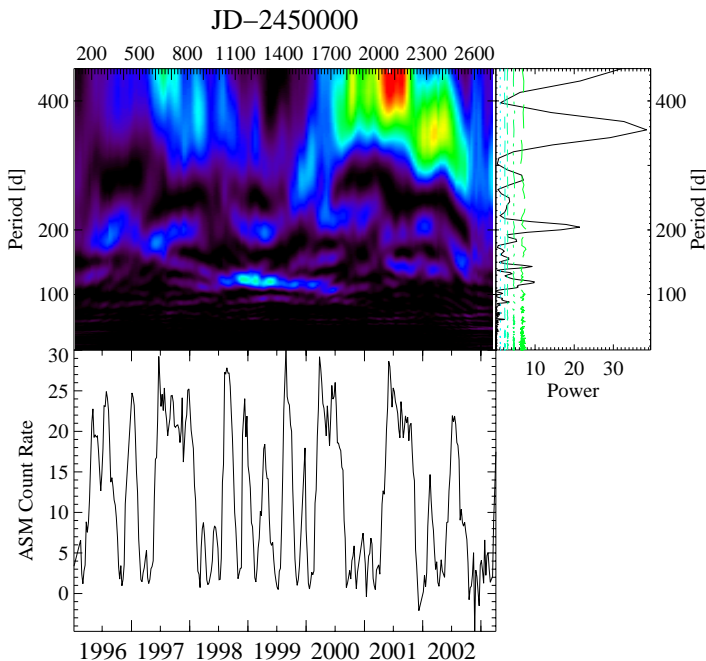
Figure 6.16: *Upper left*: Dynamical periodogram of 4U 1705−44. *Upper right*: Lomb-Scargle periodogram. The set of dashed lines represent in ascending order the 68%, 90%, 95%, 99%, and 99.9% "local significance" levels for a set of 5000 Monte Carlo white noise simulations. *Lower left*: ASM light curve.

4U 1705−44 is a bright LMXB with a neutron star classified as an atoll source. It is reported to be highly variable on short time scales (25% in 2 hr) and persistently bright. This source exhibits type I X-ray bursts and other aperiodic variability that appear to be correlated with the intensity state (Langmeier et al., 1987;

Langmeier, Hasinger & Trümper, 1989). Its different source states are supposed to reflect changes in its mass accretion rate. The thermonuclear flash model has been found to be suitable to explain the observed properties of the X-ray bursts. Furthermore Priedhorsky (1986) found a possible 222.8 day period utilizing data of the *Vela 5B* satellite. We found a significant period of ~200 days which is consistent with the *Vela 5B* period. A second peak at ~119 days was clearly more significant between 1998 and 2000 (see the dynamical periodogram, Fig. 6.16). This might be due to a change in the underlying period by a factor of ~0.5 during this years. Another broad modulation of ~355 days is also present in the data (see Fig. 6.16), this has become dominant in the last years.

To prove the veracity of these periods, several smoothed versions of the ASM light curve (as we have done for the case of GX 339−4) were produced with resolutions between 50–400 days. The PSD diagrams of these light curves show that the periods are not due to the beating between the sampling period and the long-term trend of the light curve.

6.8   *The* RXTE/*ASM sample*

In this section I present a summary of the results of the remainder of the analyzed sources which are listed in table 6.1. For each source I give a brief description of the nature of the system, and then present the main results of the long-term variability analysis together with the corresponding plots.

Table 6.1: Table of sources studied

Source	Compact object	X-ray binary classification
LMC X-3	BH	HMXB
1E 1740.7−2942	BH	LMXB
GRS 1758−258	BH	LMXB
GRS 1915+105	BH	LMXB
Cen X-3	NS	HMXB
GX 301−2	NS	HMXB
LMC X-4	NS	HMXB
2S 0114+650	NS	HMXB
4U 1907+097	NS	HMXB
EXO 2030+375	NS	HMXB, Be/X-ray binary
A 0535−668	NS	HMXB, Be/X-ray binary
4U 1145−619	NS	HMXB, Be/X-ray binary
GRO J1944+26	NS	HMXB, Be/X-ray binary
Cyg X-2	NS	LMXB
GX 13+1	NS	LMXB
GX 354−0	NS	LMXB
4U 1820−303	NS	LMXB, X-ray burster
XB 1916−053	NS	LMXB
Cyg X-3	?	HMXB
4U 1700−377	?	HMXB
4U 1908+075	?	HMXB

6.8.1 *LMC X-3*
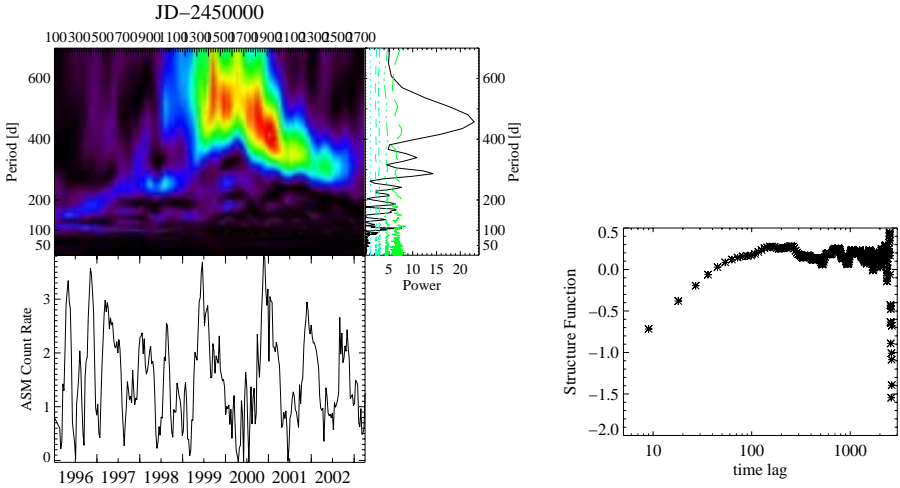
LMC X-3 is a HMXB with P_{orb} = 1.7 days seen in the optical range and with several X-ray long-term periodicities – 104, 169, 216 days with *RXTE*/ASM, 105, 214, 328 with *Ginga*/ASM (Paul, Kitamoto & Makino, 2000), ~100, ~160, ~190, and ~240 days with *RXTE*/ASM (Wilms et al., 2001) – demonstrating the absence of any stable long period. Earlier, a 198 day period was reported with *HEAO 1* and *Ginga* (Cowley et al., 1991). Boyd & Smale (2002) showed that the long-term excursion times between X-ray minima are related to each other by rational fractions, suggesting that there is a natural underlying clock in the system that sets a time scale, be found to be 10.594 days, and the excursions are simple multiples of this time scale. *Left*: the dynamical periodogram shows periods around ~454, 287, 336, 242, 106 days. The set of dashed lines represent in ascending order the 68%, 90%, 95%, 99%, and 99.9% "local significance" levels for a set of 5000 Monte Carlo white noise simulations. *Right*: the SF diagram shows a characteristic time scale of 70 days.
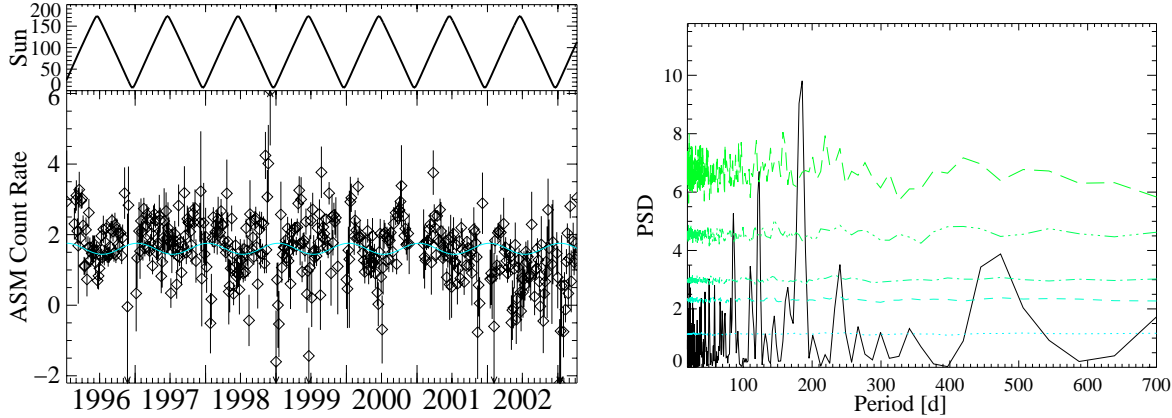
1E 1740.7−2942 is a BH in the galactic center region with P_{orb} = 12.73 days found with *RXTE*/PCA data and a superorbital modulation of ∼600 days found with *CGRO*/BATSE (Smith, Heindl & Swank, 2002), which is one of the longest seen. *Left*: 9 day binned light curve and sun angular distance. *Right*: the corresponding Lomb-Scargle periodogram. The set of dashed lines represent in ascending order the 68%, 90%, 95%, 99%, and 99.9% "local significance" levels for a set of 5000 Monte Carlo white noise simulations. We found only a suspicious ∼180 day period, perhaps a period influenced by the sampling modulation caused by the solar crossing near the source position (see section 6.1.1 for an explanation).

6.8.3 *GRS 1758−258*
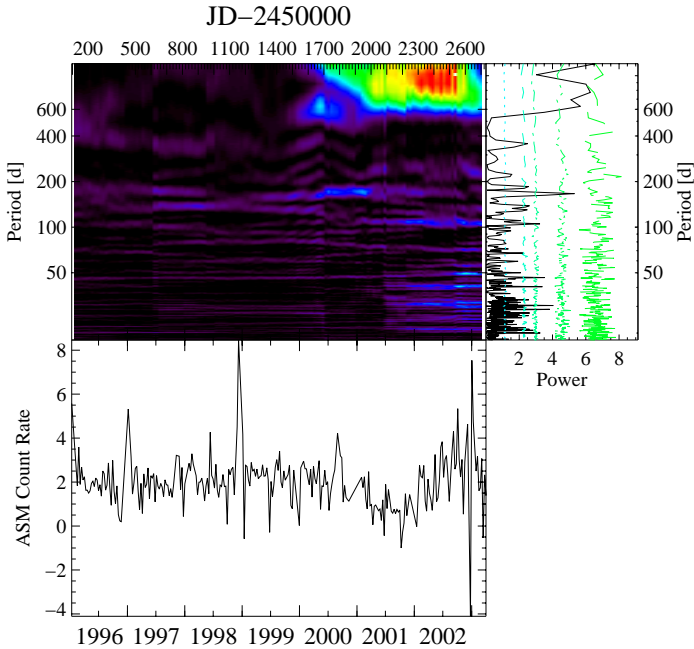
GRS 1758−258 is a LMXB with P_{orb} = 18.45 days found with *RXTE*/PCA data. A superorbital modulation of ~600 days has been suggested by Smith, Heindl & Swank (2002) with *CGRO*/BATSE data. The dynamical periodogram of the *RXTE*/ASM data does not show any period in the range of 10 to 1000 days. The set of dashed lines represent in ascending order the 68%, 90%, 95%, 99%, and 99.9% "local significance" levels for a set of 5000 Monte Carlo white noise simulations.

6.8.4 *GRS 1915+105*
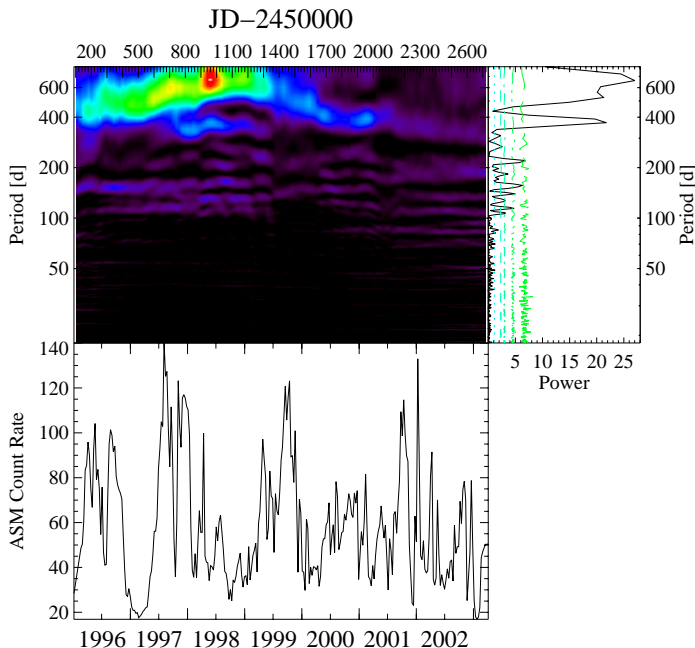
GRS 1915+105 is the LMXB with the most massive stellar black hole known. It shows a P_{orb} of 33.5 days (Greiner, Cuby & McCaughrean, 2001). A 12–17 day time scale was found with *RXTE*/ASM data over the period from 1996 February 20 to 2002 April 12 (Greenhough et al., 2003). Recently, a 590 day long-term periodicity has been reported (Rau, Greiner & McCollough, 2003). The dynamical periodogram does not show the 33.5 day period, but on the other hand, peaks around 370 days and 2×370 days are present. The set of dashed lines represent in ascending order the 68%, 90%, 95%, 99%, and 99.9% "local significance" levels for a set of 5000 Monte Carlo white noise simulations. The SF analysis does not confirm the 12–17 day time scale.

6.8.5 Cen X-3
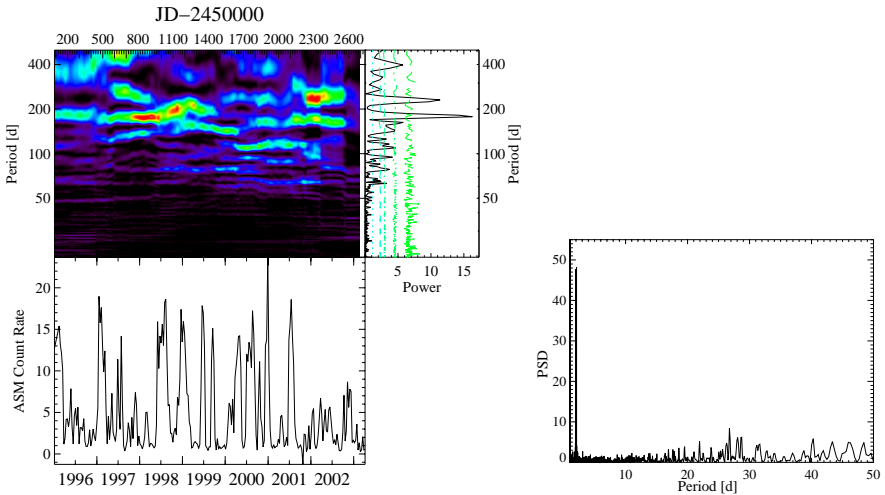
Cen X-3 is a HMXB with a NS and $P_{orb} \sim 2.1$ days (Nagase et al., 1992). A characteristic time scale of ~120–165 days was suggested by Priedhorsky, Terrell & Holt (1983) which may represent a precession of an accretion disk. Periods in the range of 26.6 days (Chester, 1978), 43 days and 200 days (Holt et al., 1979) have also been proposed but not confirmed in later observations. *Left*: 10 day binned *RXTE*/ASM light curve show two significant peaks at ~180 and ~230. The set of dashed lines represent in ascending order the 68%, 90%, 95%, 99%, and 99.9% "local significance" levels for a set of 5000 Monte Carlo white noise simulations. *Right*: The periodogram of the 1 day binned light curve shows the 2.08 day binary period.

6.8.6   GX 301−2

JD−2450000
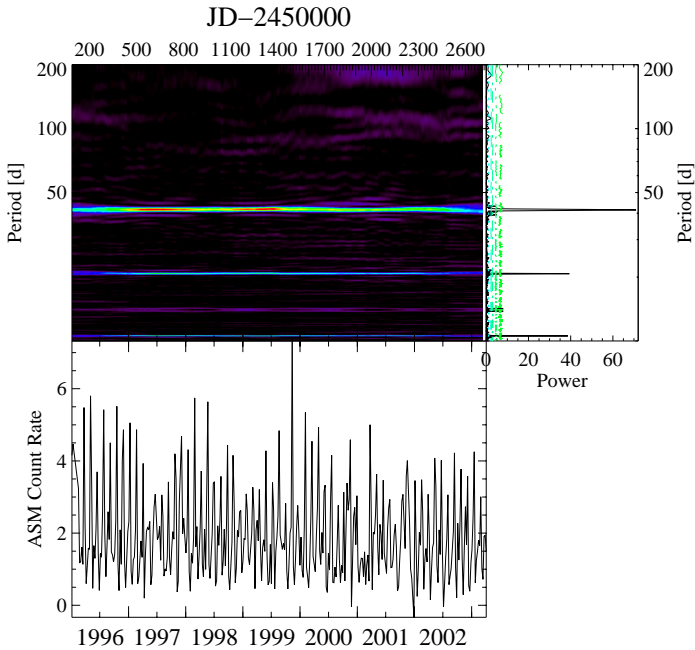
GX 301−2 is an accreting NS with a 41.5 day eccentric orbit (Sato et al., 1986).
The *RXTE*/ASM light curve has recently been modeled in detail by Leahy (2002)
using wind models. The dynamical periodogram shows peaks around 40, 20,
10 days which correspond to P_{orb} and its aliases. The set of dashed lines represent
in ascending order the 68%, 90%, 95%, 99%, and 99.9% "local significance"
levels for a set of 5000 Monte Carlo white noise simulations.

6.8.7   LMC X-4
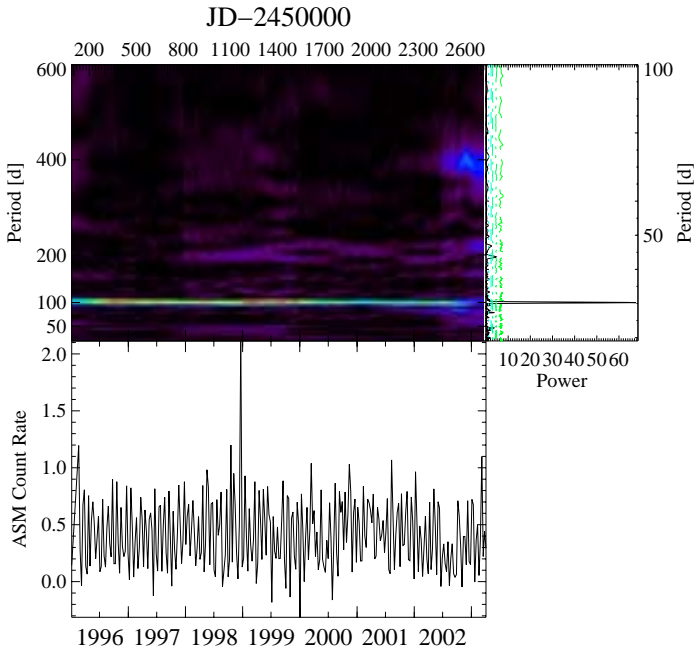
LMC X-4 is a pulsar HMXB with a 1.4 d binary period and a 30.5 day X-ray variation believed to be due to the precession of a warped accretion disk (Laycock et al., 2003). The dynamical periodogram confirms the precessional period. The set of dashed lines represent in ascending order the 68%, 90%, 95%, 99%, and 99.9% "local significance" levels for a set of 5000 Monte Carlo white noise simulations.

6.8.8   2S 0114+650
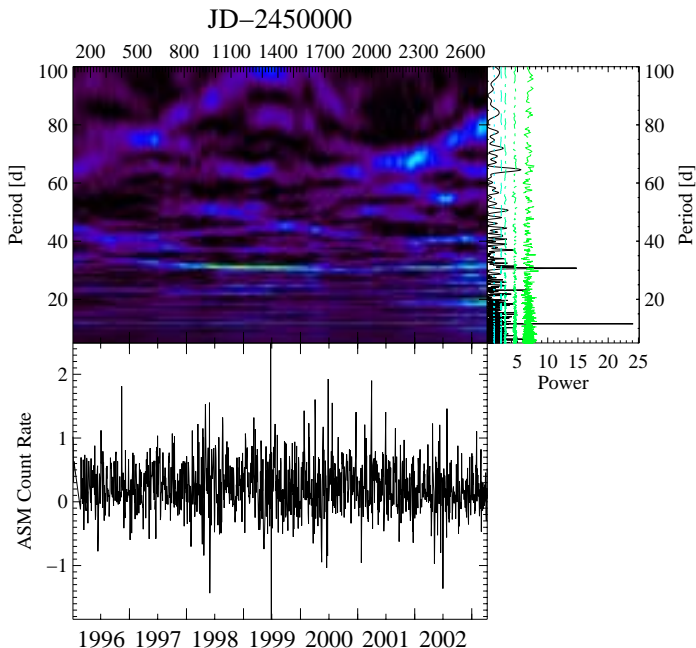
2S 0114+650 is a HMXB with a 2.3 hr pulsating NS and a P_{orb} of 11.6 days. Both periods have been also seen in the X-ray domain with *RXTE*/ASM (Corbet, Finley & Peele, 1999). The dynamical periodogram shows a ~12 day modulation and another period (somewhat less significant) around 30 days. The set of dashed lines represent in ascending order the 68%, 90%, 95%, 99%, and 99.9% "local significance" levels for a set of 5000 Monte Carlo white noise simulations.
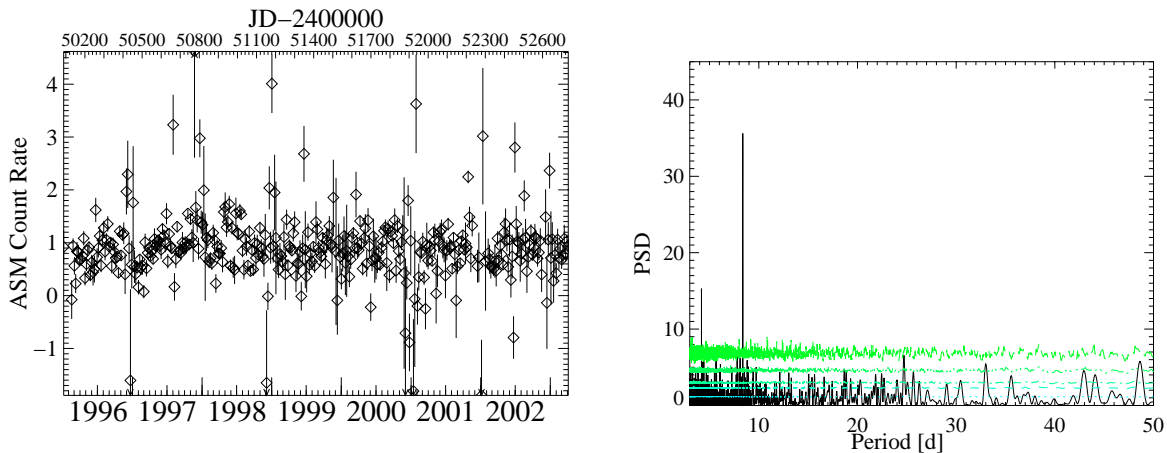
4U 1907+097 is a HMXB pulsar in which P_{orb} is believed to be 8.38 days. Two periods of 16.8 and 7.39 days have been found from the BATSE light curve (Laycock et al., 2003). *Left*: 7 day binned *RXTE*/ASM light curve. *Right*: the PSD diagram reveals the 8.37 day period and its aliases. The set of dashed lines represent in ascending order the 68%, 90%, 95%, 99%, and 99.9% "local significance" levels for a set of 5000 Monte Carlo white noise simulations.

6.8.10   *EXO 2030+375*
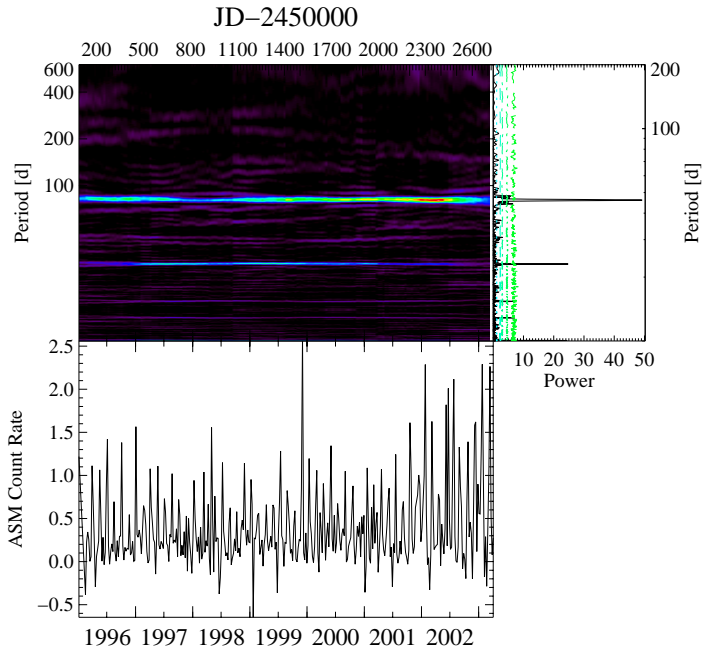
EXO 2030+375 is a Be/X-ray binary with P_{orb} of 46 days (Stollberg, 1997). The dynamical periodogram of the *RXTE*/ASM data corroborates this period and shows also its aliases seen also by Laycock et al. (2003). The set of dashed lines represent in ascending order the 68%, 90%, 95%, 99%, and 99.9% "local significance" levels for a set of 5000 Monte Carlo white noise simulations.
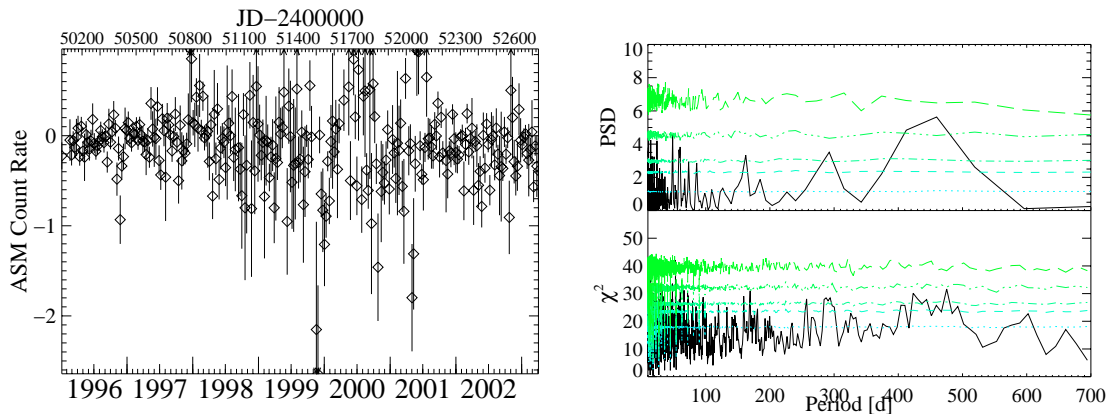
A 0535−668 is a Be/X-ray binary with a P_{orb} of 16.65 days and a long-term period of 420.82 days due to the formation and depletion of a circumnuclear disk surrounding the Be star (Alcock et al., 2001; McGowan & Charles, 2003). No significant periods are present in the PSD and epoch-folding diagrams of the *RXTE*/ASM data. The set of dashed lines represent in ascending order the 68%, 90%, 95%, 99%, and 99.9% "local significance" levels for a set of 5000 Monte Carlo white noise simulations.

JD−2400000
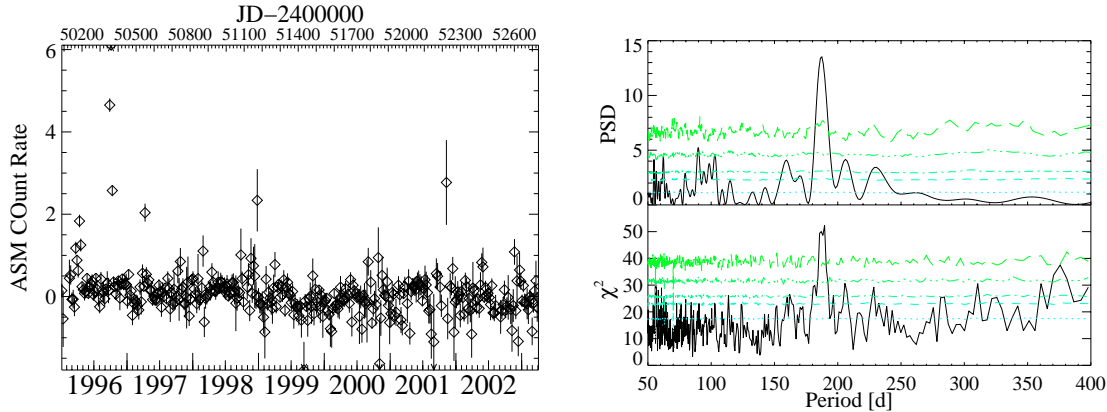
4U 1145−619 is a Be/X-ray binary showing recurrent outbursts with a period of 186.5 days (Laycock et al., 2003) which may be the consequence of phase-dependent accretion from the Be stars circumstellar disk. *Left*: 7 day binned *RXTE*/ASM light curve. *Right*: the corresponding PSD and epoch-folding diagrams which show a peak around ~185 days. The set of dashed lines represent in ascending order the 68%, 90%, 95%, 99%, and 99.9% "local significance" levels for a set of 5000 Monte Carlo white noise simulations.

6.8.13   *GRO J1944+26*
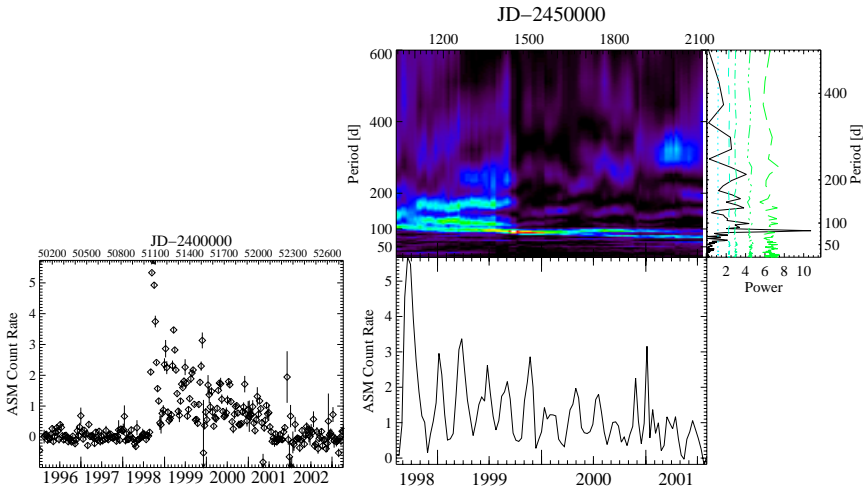
GRO J1944+26 is a Be/X-ray binary with P_{orb} of 169.2 days (Wilson et al., 2003). Campana, Israel & Stella (1999) found evidence of an ~80 day modulation during the outburst activity with the *RXTE*/ASM light curve until Sept. 1999, which may represent half the value of the orbital period. *Left*: 10 day binned *RXTE*/ASM light curve. *Right*: the dynamical periodogram from the outburst activity between Sep. 1998 and Jun. 2001 shows nothing around 170 days, but one peak at ~82 days dominant only during this period. The set of dashed lines represent in ascending order the 68%, 90%, 95%, 99%, and 99.9% "local significance" levels for a set of 5000 Monte Carlo white noise simulations.

6.8.14   Cyg X-2
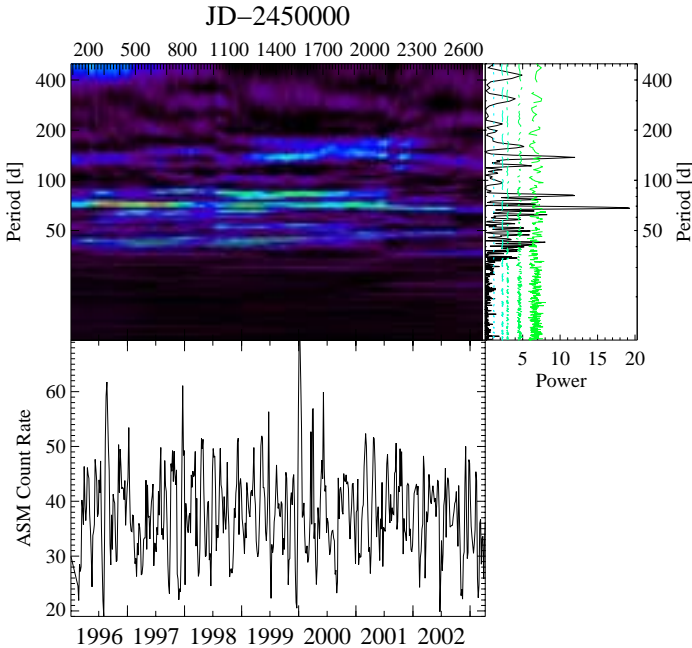
Cyg X-2 is a LMXB with NS as compact object. It shows several periods at 40.4, 68.8 days found with *RXTE*/ASM, 53.7, 61.3 days found with *Ginga*/ASM (Paul, Kitamoto & Makino, 2000), and ~78 days found also with *RXTE*/ASM and *Vela 5B* (Wijnands, Kuulkers & Smale, 1996; Smale & Lochner, 1992), which may be associated with an accretion disk precession non-stable time scale. Boyd & Smale (2002) found that the excursion times between X-ray minima in Cyg X-2 can be characterized as a series of integer multiples of the 9.8 binary orbital period. In the dynamical periodogram a predominant peak at ~70 days, and others at 140 days (may be an alias), 80 days, 40 days are present. The set of dashed lines represent in ascending order the 68%, 90%, 95%, 99%, and 99.9% "local significance" levels for a set of 5000 Monte Carlo white noise simulations. LSSM produces good fits with high order; the highest one is AR[6] with $P_1 = 74.4 \pm 5.3$ days, $P_2 = 43.64 \pm 3.09$ days, $P_3 = 136.13 \pm 11.7$ days, and $\tau_1 = 33.6 \pm 13.6$ days, $\tau_2 = 131.7 \pm 85.2$ days and $\tau_2 = 250.4 \pm 146.8$ days. This fit is also a indicator of the presence of more than one period.

6.8.15   GX 13+1
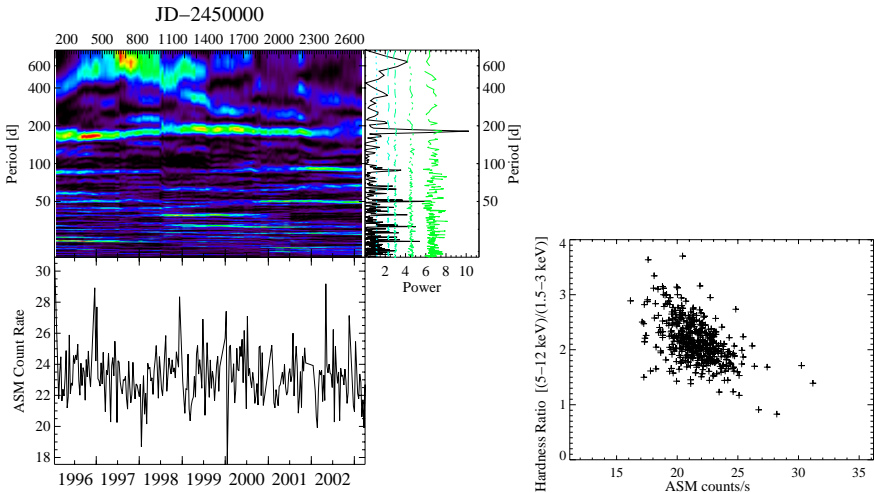
GX 13+1 is one of the brightest LMXB with a NS as compact object. Corbet (1996) suggested the presence of a modulation with a period of ~25 days in the first year of the *RXTE*/ASM light curve. *Left*: the dynamical periodogram show a peak around 25 day but with small significance, on the other hand a peak at ~180 days is present and may be associate with the sun (see section 6.1.1).The set of dashed lines represent in ascending order the 68%, 90%, 95%, 99%, and 99.9% "local significance" levels for a set of 5000 Monte Carlo white noise simulations. *Right*: the source shows a hardness anti-correlation with the *RXTE*/ASM flux.

6.8.16   GX 354−0
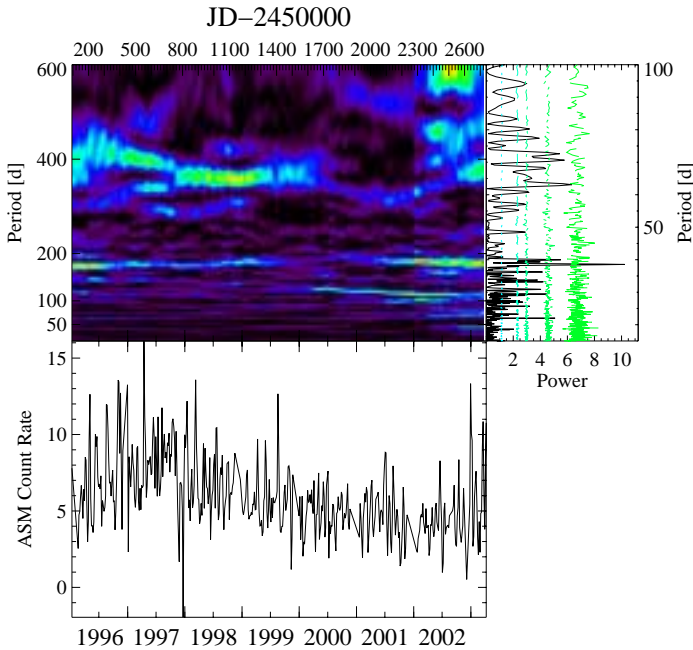
GX 354−0 is a LMXB with several super-orbital periodicities of 72 days from the *RXTE*/ASM light curve until 1998, 63 days with *Ariel 5*/ASM (Kong, Charles & Kuulkers, 1998), and the recent quasi-periodic oscillation of ∼40 days from all the available *RXTE*/ASM data until the start of 2003 (Galloway et al., 2003). The dynamical periodogram shows one dominant period at ∼39 days with a significance > 99.9%, and two other less significant periods at ∼63 days and a double peak around ∼71 days. The set of dashed lines represent in ascending order the 68%, 90%, 95%, 99%, and 99.9% "local significance" levels for a set of 5000 Monte Carlo white noise simulations.

6.8.17   4U 1820−303
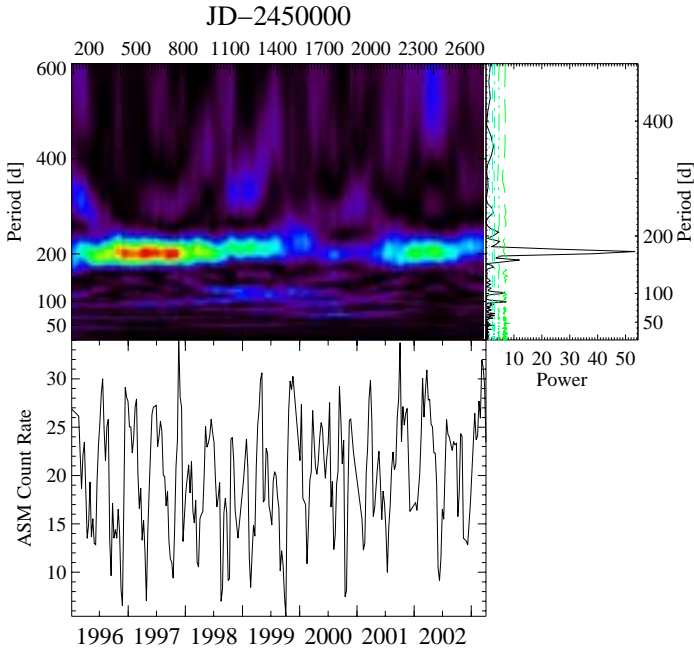
4U 1820−303 is a LMXB X-ray burster with a white dwarf companion star. A ~175 day stable long-term variation was observed by *Vela 5B* and confirmed with the *RXTE*/ASM between 1996 and 2000 (Priedhorsky & Terrell, 1984a; Chou & Grindlay, 2001). This period may be attributable to a hierarchical triple companion in the system. The dynamical periodogram shows a relative constant broad peak at ~173 days. The set of dashed lines represent in ascending order the 68%, 90%, 95%, 99%, and 99.9% "local significance" levels for a set of 5000 Monte Carlo white noise simulations. LSSM produces a good fit with an AR[2] with $\tau = 61 \pm 15$ d and $P = 182 \pm 10$ d.

6.8.18   XB 1916−053
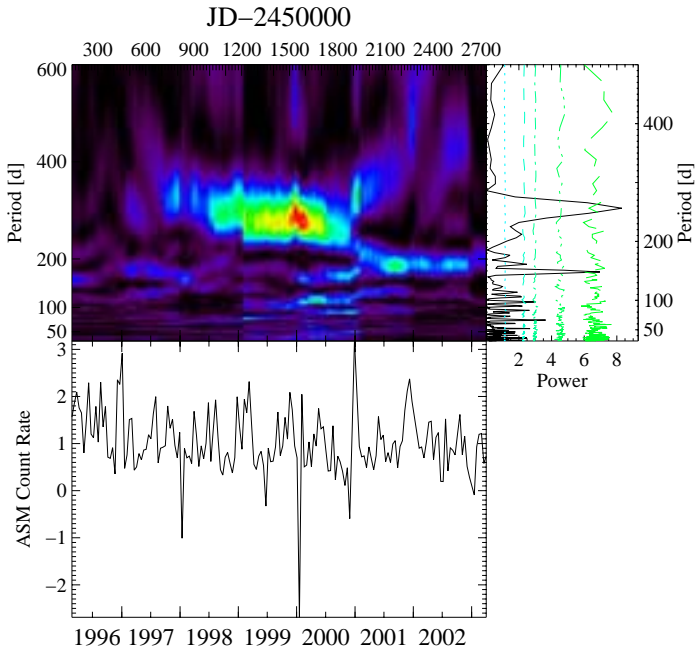
XB 1916−053 is a LMXB with a NS. It shows a possible long-term variation of 199 days (Priedhorsky & Terrell, 1984b). The dynamical periodogram shows two peaks at ~256 days and ~148 days. The set of dashed lines represent in ascending order the 68%, 90%, 95%, 99%, and 99.9% "local significance" levels for a set of 5000 Monte Carlo white noise simulations.

6.8.19   *Cyg X-3*
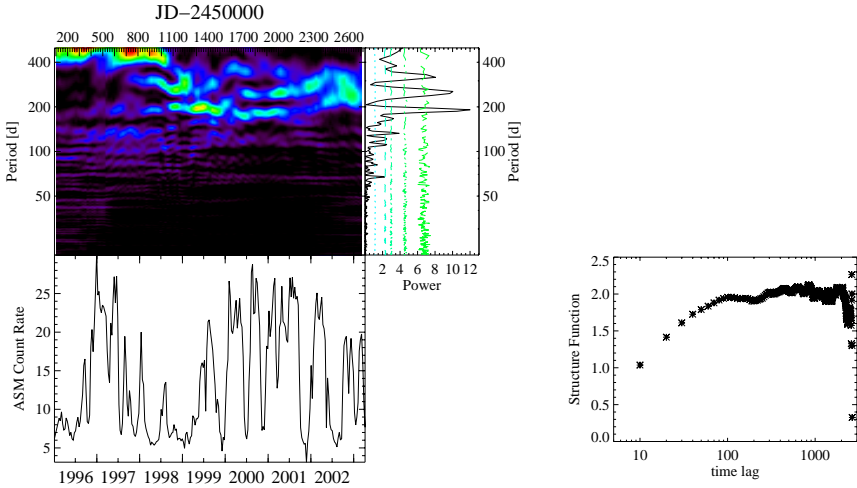
Cyg X-3 is a HMXB with a modulation in the X-ray and infrared emission of 4.8 h, which has been interpreted as the orbital period of the system (e.g., Mason, Cordova & White, 1986). It is considered to be a microquasar with ∼100 day characteristic time scale (Priedhorsky & Terrell, 1986). Boyd & Smale (2002) founded that the excursion times between X-ray minima in Cyg X-3 can be characterized as a series of integer multiples of a 71 day period. Such a period is consistent with the period range for the jet precession of ≳ 60 days proposed by Mioduszewski et al. (2001). *Left*: the dynamical periodogram shows three significant peaks around ∼192 days,, ∼255 days, and ∼317 days. The set of dashed lines represent in ascending order the 68%, 90%, 95%, 99%, and 99.9% "local significance" levels for a set of 5000 Monte Carlo white noise simulations. *Right*: the SF diagram corroborates the ∼100 day time scale.
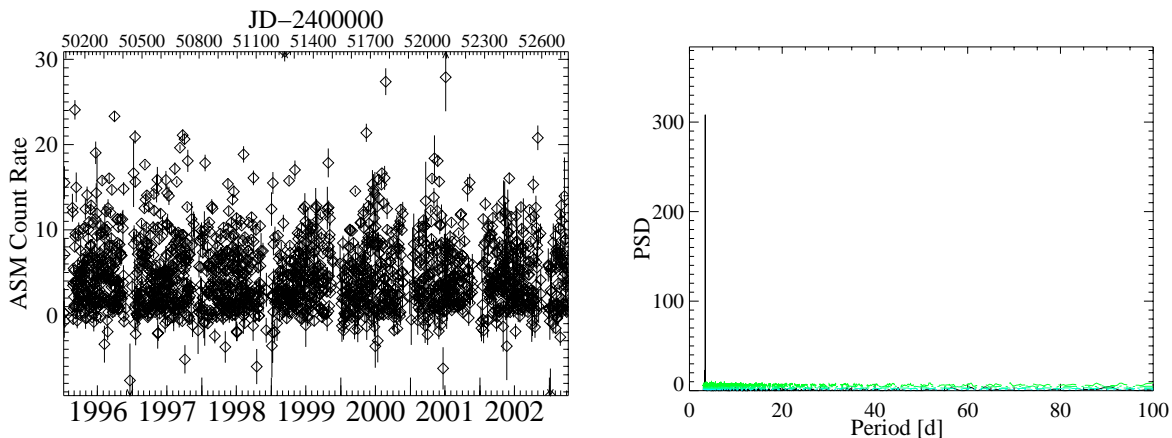
4U 1700−377 is a non-pulsating HMXB with a P_{orb} of ~3.4 days and a 13.8 day periodicity claimed by König & Maisack (1997). Due to the absence of any X-ray pulsations and the unusually hard nature of the spectrum it has been believed to have a low mass black hole as a compact object, however, it has been also proposed to be a neutron star given that the X-ray spectrum of 4U 1700−377 is qualitatively similar to those of accreting neutron stars (see Clark et al., 2002, and references therein). *Left*: 1 d binned *RXTE*/ASM light curve. *Right*: the corresponding PSD diagram which shows only the 3.4 day period. The set of dashed lines represent in ascending order the 68%, 90%, 95%, 99%, and 99.9% "local significance" levels for a set of 5000 Monte Carlo white noise simulations.
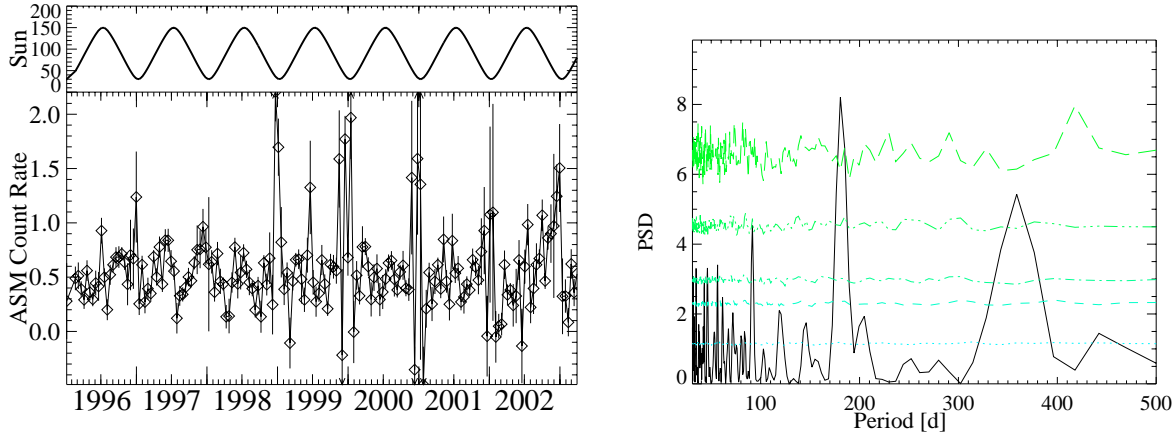
4U 1908+075 is a HMXB with a possible P_{orbital} of 4.4 days observed with *RXTE*/ASM until January 1999 (Wen, Remillard & Bradt, 2000). *Left*: 15 days binned *RXTE*/ASM light curve. *Right*: the PSD diagram shows the 4.4 day period plus one at ~200 days perhaps due to the Sun radiation effect (see section 6.1.1). The set of dashed lines represent in ascending order the 68%, 90%, 95%, 99%, and 99.9% "local significance" levels for a set of 5000 Monte Carlo white noise simulations.

Summary and outlook

X-ray variability on long time scales (from days to years) is a common phenomenon in many astronomical sources, but its origin is often unclear. Furthermore, due to the shortage of instrumentation suitable for long-term monitoring, the datasets do not yield precise periods in their analysis. Therefore, for the detection of periodic signals, it is worth scrutinizing the methods used to determine their significance. The major contribution of this thesis is the description of methods to compute significance levels for the existence of quasi-periodic oscillations (QPOs) in X-ray light curves which take the noise character of the astronomical objects into account.

I present two methods to determine the significance of possible quasi-periodic signals in "colored"-noise light curves using Monte Carlo simulations following the algorithm presented by Timmer & König (1995): (1) a frequency-dependent "local significance" test and (2) a "global significance" test. Both approaches involve simulating many light curves that match the real data in sampling time, count rate, and variance, and comparing their power diagrams to the power diagrams of the real data. For a discrete peak in an observed power diagram to be significant, it must have greater power than nearly all of the simulations at that frequency.

Two classes of objects have been analyzed in this work: Active Galactic Nuclei (AGN) and X-ray Binaries (XRBs).

The variability study applied to the ~110 ks X-ray observations of the AGN Centaurus A, which was carried out with *RXTE* between 1996 and 2000, reveals no significant temporal variability on timescales of weeks or shorter, and a relatively simple spectrum in the 2–200 keV range. The best fit spectral model consists of a heavily absorbed primary flux and a narrow emission line from cool iron. The 2–10 keV flux was the same in 1996 and 1998, and increased by 60% in 2000. This implies that the line emitting region is not very close to the region containing the primary flux generation. This is consistent with the lack of a significant reflection component contribution to the overall flux. We conclude that the Fe line

does not originate close to the central X-ray source, although a strong Fe line is observed. The Fe line originates then within material of a large column outside of the line of sight. A possible source of the Fe line flux could be for example the postulated molecular torus. Our conclusion is also confirmed by the presence of no correlation between the variability behavior of N_H and the iron line flux, since N_H varied with observation and the line flux did not. The N_H could originate at the edge of the accretion disk and thus its variability might be due to small changes in the disk structure, while the iron line material lies outside of this line of sight.

Applying epoch folding and periodogram analysis to the *XMM-Newton* observation of the Seyfert galaxy Mrk 766, a possible QPO at a timescale of 4200 s has been reported (Boller et al., 2001). The "local significance" test based on this method shows that the 4200 s feature in Mrk 766 is in fact not significant at the 95% level. The "global significance" of the 4200 s feature is 45%, i.e., higher peaks in the 2000–5000 s period range are found in roughly half of all simulated light curves. We conclude that we cannot confirm the claim of a ~4200 s QPO. Rather, the 4200 s peak is attributable to a random occurrence due to the red noise character of AGN data.

Lastly, I have shown that XRBs exhibit a wide range of different variability patterns. Temporal variability behavior from long-term light curves obtained with the ASM on board the RXTE have been reviewed. Some results of searches for periodicities in the ASM light curves from X-ray binaries are presented. For the BH candidate Cyg X-1 I confirm the 150 day periodicity to be associated with the hard state, where also a ~ 420 day modulation is present. Analyzing the hardness ratio of the different ASM energy bands I show that the 150 day period corresponds to intensity variations of the source flux and the ~420 day modulation to spectral variations which may be linked to the failed spectral transitions. A period on the ~150 day time scale is probably due to precession and/or radiative warping of an accretion disk, as suggested by Brocksopp et al. (1999). For the soft X-ray transient Aql X-1 I find a time scale of ~226 days which might be consistent with the underlying period of Priedhorsky & Terrell (1984b) (since $2 \times 122 \simeq 226$). A modulation of about 450 days (equivalent to the 436 days of Priedhorsky & Terrell, 1984b) is also present. Furthermore the color versus intensity diagram shows a hardening of the X-ray spectrum as the system declines into quiescence, which together with the outbursts I interpret as a thermal instability in the outer disk which propagates inward (Shahbaz et al., 1998). The BH candidate GX 339−4 shows a strong peak around 24 hours in his periodogram. It has been demonstrated in this work, that this period corresponds to an observational effect of the *RXTE* satellite and not to a physical modulation of the source. On long time scales I confirm the 240 day characteristic time scale found by Nowak, Wilms & Dove (1999), and observe a significant peak in the Off state from 1999 to 2002 at ~ 120 days,

which can be an alias of the 240 day characteristic time scale. As noted by Nowak, Wilms & Dove (1999), the observed long-term variability of GX 339−4 could be due to a combination of a quasi-steadily precessing disk at large radii with coronal structure changes on small radii, making the quasi-periodic oscillation a possible characteristic precursor to the LS/HS transition. The atoll source 4U 1705−44 shows a ∼ 200 day period which is consistent with the *Vela 5B* period (Priedhorsky, 1986). A second peak at ∼119 days was clearly more significant between 1998 and 2000. This might be due to a change in the underlying period by a factor of ∼0.5 during this years. The LMXB 4U 1957+11 shows a long-term variability behavior much more complicated than one simple period, and furthermore, no complete stable periods are present in the system. The eclipsing binary pulsar SMC X-1 shows a not steady high-low state variation with a quasi-periodic cycle of ∼60 days. The superorbital period is believed to be the consequence of a precessing, warped accretion disk (Gruber & Rothschild, 1984; Zhang et al., 1996). We observe a correlation between the characteristic frequency of the variability and the source flux, i.e., a correlation between the X-ray flux and the disk precession. It is likely that the increased source flux corresponds to an increased mass accretion rate, $\dot{M}$. This implies that increased mass accretion rates lead to an increase of the accretion disk precessional frequency. Looking at the XRB sample overview I conclude that the long-term modulations present in systems containing a NS as compact object are usually more stable that those for systems containing a BH, which show broad variable features in the periodograms.

Analysis on the two main areas of this research, the significance level determination of periodic or quasi-periodic modulations, and the long-term variability behavior, should be continued. On the one hand, due to the dubious veracity of the kilosecond QPO detections claimed for AGN in the last years, the significance of these features should be re-calculated for already published results and also for future detections. On the other hand, the Monte Carlo simulation code should be improved with the implementation of new noise models or the combination of them. Also, the process of categorizing the patterns for the XRB sources with the *RXTE*/ASM instrument has not been concluded. Furthermore, new data from new satellite missions, such *INTEGRAL* or *MIRAX*, can improve the interpretation of the long-term behavior of these objects.

Bibliography

Abraham, Z., Kaufmann, P., & Botti, L., 1982, AJ, 87, 532

Alcock, C., et al., 2001, MNRAS, 321, 678

Antonucci, R., 1993, ARA&A, 31, 473

Apparao, K. M. V., 1994, Space Sci. Rev., 69, 255

Arnaud, K. A., 1996, in Astronomical Data Analysis Software and Systems V, ed. G. H. Jacoby, J. Barnes, (San Francisco: Astron. Soc. Pacific), 17

Baity, W. A., et al., 1981, ApJ, 244, 429

Band, D. L., König, M., & Chernenko, A., 1998, in Gamma-Ray Bursts, 4th Hunstville Symposium, 211

Begelman, M. C., McKee, C. F., & Shields, G. A., 1983, ApJ, 271, 70

Benlloch, S., Rothschild, R. E., Wilms, J., Reynolds, C. S., Heindl, W. A., & Staubert, R., 2001a, A&A, 371, 858

Benlloch, S., Wilms, J., Edelson, R., Tahir, Y., & Staubert, R., 2001b, ApJ, 562, L121

Benlloch, S., Wilms, J., Staubert, R., & Nowak, M., 2001c, in Exploring the gamma-ray universe. Proceedings of the Fourth INTEGRAL Workshop, 4-8 September 2000, Alicante, Spain. Editor: B. Battrick, Scientific editors: A. Gimenez, V. Reglero & C. Winkler. ESA SP-459, Noordwijk: ESA Publications Division, ISBN 92-9092-677-5, 2001, p. 263 - 266, 263

Bevington, P. R., & Robinson, D. K., 1992, Data Reduction and Error Analysis for the Physical Sciences, (New York: McGraw-Hill), 2nd edition

Boller, T., Keil, R., Trümper, J., O'Brien, P. T., Reeves, J., & Page, M., 2001, A&A, 365, L146

Bolton, C. T., 1972, Nat, 235, 271

Bond, I. A., et al., 1996, A&A, 307, 708

Boyd, P. T., & Smale, A. P., 2002, ApJ, submitted

Bregman, J. N., et al., 1988, ApJ, 331, 746

Brocksopp, C., Fender, R. P., Larionov, V., Lyuty, V. M., Tarasov, A. E., Pooley, G. G., Paciesas, W. S., & Roche, P., 1999, MNRAS, 309, 1063

Byram, E. T., Chubb, T. A., & Friedman, H., 1966, Science, 152, 66

Callanan, P. J., Charles, P. A., Honey, W. B., & Thorstensen, J. R., 1992, MNRAS, 259, 395

Campana, S., Israel, G., & Stella, L., 1999, A&A, 352, L91

Carson, M., McKernan, B., Yaqoob, T., & Fegan, D., 1998, in 19th Texas Symposium on Relativistic Astrophysics and Cosmology, ed. J. Paul, T. Montmerle, E. Aubourg

Chatfield, C., 1989, in The analysis of time series. An introduction, Chapman & Hall), Chapt. 7

Chester, T. J., 1978, ApJ, 219, L77

Chevalier, C., & Ilovaisky, S. A., 1991, A&A, 251, L11

Chou, Y., & Grindlay, J. E., 2001, ApJ, 563, 934

Clark, J. S., Goodwin, S. P., Crowther, P. A., Kaper, L., Fairbairn, M., Langer, N., & Brocksopp, C., 2002, A&A, 392, 909

Clarkson, W. I., Charles, P. A., Coe, M. J., & Laycock, S., 2003a, MNRAS, 339, 447

Clarkson, W. I., Charles, P. A., Coe, M. J., & Laycock, S., 2003b, MNRAS, accepted (astro-ph/0304073)

Corbel, S., Fender, R. P., an dM. Nowak, A. K. T., McIntyre, V., Durouchoux, P., & Sood, R., 2000, A&A, 359, 251

Corbet, R., 1996, IAU Circ.

Corbet, R. H. D., Finley, J. P., & Peele, A. G., 1999, ApJ, 511, 876

Corbet, R. H. D., Thorstensen, J. R., Charles, P. A., Honey, W. B., Smale, A. P., & Menzies, J. W., 1987, MNRAS, 227, 1055

Cowley, A. P., & Schmidtke, P. C., 2002, ApJ, 123, 1741

Cowley, A. P., Schmidtke, P. C., Ebisawa, K., Makino, F., Remillard, R. A., Crampton, D., & Hutchings, J. B., 1991, ApJ, 381, 526

Czerny, M., Czerny, B., & Grindlay, J. E., 1987, ApJ, 312, 122

Davies, S. R., 1990, MNRAS, 244, 93

Davies, S. R., 1991, MNRAS, 251, 64

Deeming, T. J., 1975, Ap&SS, 36, 137

Deeter, J. E., & Boynton, P. E., 1982, ApJ, 261, 337

Dermer, C. D., & Gehrels, N., 1995, ApJ, 447, 103

Döbereiner, S., Junkes, N., Wagner, S. J., Zinnecker, H., Fosbury, R., Fabbiano, G., & Schreier, E. J., 1996, ApJ, 470, L15

Done, C., Madejski, G. M., Mushotzky, R. F., Turner, T. J., Koyama, K., & Kunieda, H., 1992, ApJ, 400, 138

Ebneter, K., & Balick, B., 1983, PASP, 95, 675

Edelson, R., & Nandra, K., 1999, ApJ, 514, 682

Esin, A. A., Narayan, R., Cui, W., Grove, J. E., & Zhang, S.-N., 1998, ApJ, 505, 854

Fabian, A. C., Eggleton, P. P., Hut, P., & Pringle, J. E., 1986, ApJ, 305, 333

Fanaroff, B. L., & Riley, J. M., 1974, MNRAS, 167, 31

Feigelson, E. D., Schreier, E. J., Delvaille, J. P., Giacconi, R., Grindlay, J. E., & Lightman, A. P., 1981, ApJ, 251, 31

Fender, R., 2001a, Ap&SS, 276, 69

Fender, R., 2001b, in High Energy Gamma-Ray Astronomy, 221

Fender, R., 2002, in LNP Vol. 589: Relativistic Flows in Astrophysics, 101

Fender, R., et al., 1999, Astrophys. J., Lett., 519, L165

Fender, R. P., 2001c, in AIP Conf. Proc. 599: X-ray Astronomy: Stellar Endpoints, AGN, and the Diffuse X-ray Background, 101

Feng, Y. X., Zhang, S. N., Sun, X., Durouchoux, P., Chen, W., & Cui, W., 2001, ApJ, 553, 394

Fiore, F., Massaro, E., Perola, G. C., & Piro, L., 1989, ApJ, 347, 171

Foster, G., 1996, ApJ, 112, 1709

Francey, R. J., Fenton, A. G., Harries, J. R., & McCracken, K. G., 1967, Nat, 216, 773

Friesdman, H., & Byram, E. T., 1967, Science, 158, 257

Galloway, D. K., Psaltis, D., Chakrabarty, D., & Muno, M. P., 2003, ApJ, 590, 999

Gantert, C., 1989, *Ph.D. thesis*, Universität Freiburg

Giacconi, R., Gursky, H., Paolini, F. R., & Rossi, B. B., 1962, Phys. Rev. Lett., 9, 439

Gliozzi, M., Sambruna, R. M., & Eracleous, M., 2003, ApJ, 584, 176

Grandi, P., et al., 2000, Adv. Space Res., 25,

485

Green, A. R., McHardy, I. M., & Done, C., 1999, MNRAS, 305, 309

Green, A. R., McHardy, I. M., & Lehto, H. J., 1993, MNRAS, 265, 664

Greenhough, J., Chapman, S. C., Chaty, S., Dendy, R. O., & Rowlands, G., 2003, MNRAS, 340, 851

Greiner, J., Cuby, J. G., & McCaughrean, M. J., 2001, Nat, 414, 522

Grossmann, A., Kronland-Martinet, R., & Morlet, J., 1989, in Wavelets: time-frequency methods and phase space, Springer-Verlag), Chapt. 2

Gruber, D. E., & Rothschild, R. E., 1984, ApJ, 283, 546

Halpern, J. P., Leighly, K. M., & Marshall, H. L., 2003, ApJ, 585, 665

Halpern, J. P., & Marshall, H. L., 1996, ApJ, 464, 760

Hasinger, G., 1996, A&AS, 120, 607

Hasinger, G., & van der Klis, M., 1989, A&A, 225, 79

Hjellming, R. M., & Narayan, R., 1986, ApJ, 310, 768

Holt, S. S., Kaluzienski, L. J., Boldt, E. A., & Serlemitsos, P. J., 1979, ApJ, 227, 563

Honerkamp, J., 1994, Stochastic Dynamical Systems: Concepts, Numerical Methods, Data Analysis, (Weinheim: VCH)

Horne, J. H., & Baliunas, S. L., 1986, ApJ, 302, 757

Hughes, P. A., Aller, H. D., & Aller, M. F., 1992, ApJ, 396, 469

Hui, X., Ford, H. C., Ciardullo, R., & Jacoby, G. H., 1993, ApJ, 414, 463

Hynes, R. I., Steeghs, D., Casares, J., Charles, P. A., & O'Brien, K., 2003, ApJ, 583, L95

Israel, F. P., 1998, A&AR, 8, 237

Iwasawa, K., Fabian, A. C., Brandt, W. N., Kunieda, H., Misaki, K., Reynolds, C. S., & Tershima, Y., 1998, MNRAS, 295, L20

Jahoda, K., Swank, J. H., Giles, A. B., Stark, M. J., Strohmayer, T., Zhang, W., & Morgan, E. H., 1996, in EUV, X-Ray, and Gamma-Ray Instrumentation for Astronomy VII, ed. O. H. Siegmund, (Bellingham, WA: SPIE), 59

Jourdain, E., et al., 1993, ApJ, 412, 586

Kaspi, V. M., Gavriil, F. P., Chakrabarty, D., Lackey, J. R., & Muno, M. P., 2001, ApJ, 558, 253

Kaspi, V. M., Gavriil, F. P., Woods, P. M., Jensen, J. B., Roberts, M. S. E., & Chakrabarty, D., 2003, Astrophys. J., Lett., 588, L93

Katz, J. I., 1973, Nat, Phys. Sci., 246, 87

Kawaguchi, T., & Mineshige, S., 1998, in IAU Symp. 194, Activity in galaxies and related phenomena

Kemp, J. C., et al., 1983, ApJ, 271, L65

Kemp, J. C., Karitskaya, E. A., Kumsiashvili, M. I., Lyutyi, V. M., Khruzina, T. S., & Chereoashchuk, A. M., 1987, SvA, 31, 170

Kinzer, R. L., et al., 1995, ApJ, 449, 105

Kitamoto, S., Egoshi, W., Miyamoto, S., Tsunemi, H., Ling, J. C., Wheaton, W. A., & Paul, B., 2000, ApJ, 531, 546

Kitamoto, S., Tsunemi, H., Miyamoto, S., & Roussel-Dupre, D., 1993, ApJ, 403, 315

Kong, A. K. H., Charles, P. A., & Kuulkers, E., 1998, New Astron., 3, 301

Kong, A. K. H., Charles, P. A., Kuulkers, E., & Kitamoto, S., 2002, MNRAS, 329, 588

Kong, A. K. H., Kuulkers, E., Charles, P. A., & Homer, L., 2000, MNRAS, 312, L49

König, M., 1997, *Ph.D. thesis*, Eberhard Karls Universität Tübingen

König, M., & Maisack, M., 1997, A&A, 327, L33

König, M., Staubert, R., & Wilms, J., 1997, A&A, 326, L25

König, M., & Timmer, J., 1997, A&AS,

124, 589

Kraft, R. P., et al., 2000, ApJ, 531, L9

Krolik, J. H., 1999, Active Galactic Nuclei, (Princeton, NJ: Princeton University Press)

Kuster, M., Benlloch, S., Kendziorra, E., & Briel, U. G., 1999, in EUV, X-ray and Gamma-Ray Instrumentation for Astronomy X, ed. O. H. Siegmund, K. A. Flanagan, (Bellingham, WA: SPIE), 673

Lainela, M., & Valtaoja, E., 1993, ApJ, 416, 485

Langmeier, A., Hasinger, G., & Trümper, J., 1989, ApJ, 340, L21

Langmeier, A., Sztajno, M., Hasinger, G., Trümper, J., & Gottwald, M., 1987, ApJ, 323, 288

Larsson, S., 1996, A&AS, 117, 197

Laycock, S., Coe, M. J., Wilson, C. A., Harmon, B. A., & Finger, M., 2003, MNRAS, 338, 211

Leahy, D. A., 2002, A&A, 391, 219

Leahy, D. A., Darbro, W., Elsner, R. F., Weisskopf, M. C., Sutherland, P. G., Kahn, S., & Grindlay, J. E., 1983, ApJ, 266, 160

Lee, J. C., Fabian, A. C., Reynolds, C. S., Brandt, W. N., & Iwasawa, K., 2000, MNRAS, 318, 857

Lehto, H. J., 1989, in Proc. 23rd ESLAB Symposium on Two Topics in X-Ray Astronomy, ed. J. Hunt, B. Battrick, Vol. 1, (Noordwijk: ESA Publications Division), 499

Lehto, H. J., Czerny, B., & McHardy, I. M., 1993, MNRAS, 261, 125

Leighly, K. M., Mushotzky, R. F., Yaqoob, T., Kunieda, H., & Edelson, R., 1996, ApJ, 469, 147

Levine, A., Rappaport, S., Deeter, J. E., Boynton, P. E., & Nagase, F., 1993, ApJ, 410, 328

Levine, A. M., Bradt, H., Cui, W., Jernigan, J. G., Morgan, E. H., Remillard, R.,

Shirey, R. E., & Smith, D. A., 1996, ApJ, 469, L33

Levine, A. M., Bradt, H. V., Enevoldsen, A., Morgan, E. H., Remillard, R. A., Wen, L., & Smith, D. A., 2000, BAAS, 32, 1260

Lewin, W. H. G., & Joss, P. C., 1983, in Accretion-Driven Stellar X-ray Sources, 41

Lewin, W. H. G., Paradijs, J. V., & Taam, R. E., 1995, in Lewin, van Paradijs & van den Heuvel (1995), Chapt. 4, 175–232

Lewin, W. H. G., van Paradijs, J., & van den Heuvel, E. P. J., (eds.) 1995, X-Ray Binaries, Cambridge Astrophysics Series 26, (Cambridge: Cambridge Univ. Press)

Liu, Q. Z., van Paradijs, J., & van den Heuvel, E. P. J., 2000, A&AS, 147, 25

Liu, Q. Z., van Paradijs, J., & van den Heuvel, E. P. J., 2001, A&A, 368, 1021

Lomb, N. R., 1976, Ap&SS, 39, 447

Lyutyi, V. M., 1985, SvA, 29, 429

Madejski, G. M., Done, C., Turner, T. J., Mushotzky, R. F., Serlemitsos, P., Fiore, F., Sikora, M., & Begelman, M. C., 1993, Nat, 365, 626

Magdziarz, P., & Zdziarski, A. A., 1995, MNRAS, 273, 837

Maloney, P. R., Begelman, M. C., & Nowak, M. A., 1998, ApJ, 504, 77

Maloney, P. R., Begelman, M. C., & Pringle, J. E., 1996, ApJ, 472, 582

Marconi, A., Schreier, E. J., Koekemoer, A., Capetti, A., Axon, D., Macchettoand, D., & Caon, N., 2000, ApJ, 528, 276

Markowitz, A., & Edelson, R., 2000, in Rossi2000: Astrophysics with the Rossi X-ray Timing Explorer. March 22-24, 2000 at NASA's Goddard Space Flight Center, Greenbelt, MD USA, E38

Marshall, N., Warwick, R. S., & Pounds, K. A., 1981, MNRAS, 194, 987

Mason, K. O., Cordova, F. A., & White, N. E., 1986, ApJ, 309, 700

Mather, J. C., et al., 1990, Astrophys. J., Lett., 354, L37

McGowan, K. E., & Charles, P. A., 2003, MNRAS, 339, 748

McHardy, I., 1988, Mem. Soc. Astron. Ital., 59, 239

Mereghetti, S., & Stella, L., 1995, Astrophys. J., Lett., 442, L17

Meyer, F., 1986, in Radiation Hydrodynamics in Stars and Compact Objects, ed. D. Mihalas, K.-H. A. Winkler, (New York: Astron. Soc. Pacific), 249

Mioduszewski, A. J., Rupen, M. P., Hjellming, R. M., Pooley, G. G., & Waltman, E. B., 2001, ApJ, 553, 766

Mitsuda, K., et al., 1984, PASJ, 36, 741

Mittaz, J. P. D., & Branduardi-Raymont, G., 1989, MNRAS, 238, 1029

Miyamoto, S., Kimura, K., & Kitamoto, S., 1991, ApJ, 383, 784

Miyamoto, S., Kitamoto, S., Iga, S., Negoro, H., & Terada, K., 1992, ApJ, 391, L21

Morganti, R., Fosbury, R. A. E., Hook, R. N., Robindon, A., & Tsvetanov, Z., 1992, MNRAS, 256, 1

Morganti, R., Killeen, N. E. B., Ekers, R. D., & Oosterloo, T. A., 1999, MNRAS, 307, 750

Morrison, R., & McCammon, D., 1983, ApJ, 270, 119

Mushotzky, R. F., Done, C., & Pounds, K. A., 1993, ARA&A, 31, 717

Nagase, F., Corbet, R. H. D., Day, C. S. R., Inoue, H., Takeshima, T., & Yoshida, K., 1992, ApJ, 396, 147

Nandikotkur, G., Sreekumar, P., & Carter-Lewis, D. A., 1997, in Proc. 4th Compton Symposium, ed. C. D. Dermer, M. S. Strickman, J. D. Kurfess, (Woodbury: AIP), 1361

Nandra, K., George, I. M., Mushotzky, R. F., Turner, T. J., & Yaqoob, T., 1997, ApJ, 476, 70

Nowak, M. A., Dove, J. B., Vaughan, B. A., Wilms, J., & Begelman, M. C., 1998, in The Active X-Ray Sky: Results from Beppo-SAX and RXTE, ed. L. Scarsi, H. Bradt, P. Giommi, F. Fiore, Vol. 69, (Amsterdam: Elsevier), 302

Nowak, M. A., & Wilms, J., 1999, ApJ, 522, 476

Nowak, M. A., Wilms, J., & Dove, J. B., 1999, ApJ, 517, 355

Nowak, M. A., Wilms, J., & Dove, J. B., 2002, MNRAS, 332, 856

Ogilvie, G. I., & Dubus, G., 2001, MNRAS, 320, 485

Osaki, Y., 1985, A&A, 144, 369

Osone, S., Teshima, M., & Mase, K., 2001, in Proc. 27th ICRC, (astro-ph/0106223)

Özdemir, S., & Demircan, O., 2001, Ap&SS, 278, 319

Page, M. J., et al., 2001, A&A, 365, L152

Paltani, S., Courvoisier, T. J.-L., Blecha, A., & Bratschi, P., 1997, A&A, 327, 539

Paltani, S., Courvoisier, T. J.-L., & Walter, R., 1998, A&A, 340, 47

Papadakis, I. E., & Lawrence, A., 1993a, MNRAS, 261, 612

Papadakis, I. E., & Lawrence, A., 1993b, Nat, 361, 233

Papadakis, I. E., & Lawrence, A., 1995, MNRAS, 272, 161

Paul, B., Kitamoto, S., & Makino, F., 2000, ApJ, 528, 410

Peterson, B. M., 2001, in Advanced Lectures on the Starburst-AGN, 3

Petterson, J. A., 1977, ApJ, 214, 550

Pfefferkorn, F., Boller, T., Burwitz, V., & Predehl, P., 2001, in Proc. MAXI workshop on AGN variability, (astro-ph/0106203)

Pooley, G. G., Fender, R. P., & Brocksopp, C., 1999, MNRAS, 302, 1

Pottschmidt, K., 2002, *Ph.D. thesis*, Eberhard Karls Universität Tübingen

Pottschmidt, K., König, M., Wilms, J., &

Staubert, R., 1998, A&A, 334, 201

Pottschmidt, K., et al., 2003, A&A, submitted (astro-ph/0202258)

Poutanen, J., & Coppi, P. S., 1998, in Abstracts of the 19th Texas Symposium on Relativistic Astrophysics and Cosmology, held in Paris, France, Dec. 14-18, 1998. Eds.: J. Paul, T. Montmerle, and E. Aubourg (CEA Saclay).

Press, W. H., 1978, Comments on Astrophysics, 7, 103

Press, W. H., Flannery, B. P., Teukolsky, S. A., & Vetterling, W. T., 1986, Numerical Recipes, Cambridge university Press)

Press, W. H., & Rybicki, G. B., 1989, ApJ, 338, 277

Priedhorsky, W., 1986, Space Sci. Rev., 126, 89

Priedhorsky, W., & Terrell, J., 1984a, ApJ, 284, L17

Priedhorsky, W., & Terrell, J., 1986, ApJ, 301, 886

Priedhorsky, W. C., & Holt, S. S., 1987, Space Sci. Rev., 45, 291

Priedhorsky, W. C., & Terrell, J., 1984b, ApJ, 280, 661

Priedhorsky, W. C., Terrell, J., & Holt, S. S., 1983, ApJ, 270, 233

Pringle, J. E., 1996, MNRAS, 281, 357

Rau, A., Greiner, J., & McCollough, M. L., 2003, ApJ, 590, L37

Rees, M. J., 1984, ARA&A, 22, 471

Reig, P., Méndez, M., van der Klis, M., & Ford, E. C., 2000, ApJ, 530, 916

Ribó, M., Peracaula, M., Paredes, J. M., Núñez, J., & Otazu, X., 2000, in Exploring the Gamma-Ray Universe, ed. A. Gimenez, V. Reglero, C. Winkler, ESA Publications, (Noordwijk), 333

Roberts, W. J., 1974, ApJ, 187, 575

Rothschild, R. E., et al., 1999, ApJ, 510, 651

Rothschild, R. E., et al., 1998, ApJ, 496, 538

Samimi, J., et al., 1979, Nat, 278, 434

Sato, N., Nagase, F., Kawai, N., Kelley, R. L., Rappaport, S., & White, N. E., 1986, ApJ, 304, 241

Scargle, J. D., 1981, ApJ, 45, 1

Scargle, J. D., 1982, ApJ, 263, 835

Scargle, J. D., 1989, ApJ, 343, 874

Scargle, J. D., 1993, in Applications of time series analysis in astronomy and meteorology, ed. O. Lessi, (Padova, Italy)

Schandl, S., & Meyer, F., 1994, A&A, 289, 149

Schlittgen, R., & Streitberg, B. H. J., 1995, Zeitreihenanalyse, (München, Wien: Oldenbourg), 6th edition

Schreier, E. J., Feigelson, E., Delvaille, J., Giacconi, R., Grindlay, J., Schwartz, D. A., & Fabian, A. C., 1979, ApJ, 234, L39

Schwarzenberg-Czerny, A., 1992, A&A, 260, 268

Schwarzenberg-Czerny, A., 1997, ApJ, 489, 941

Schwarzenberg-Czerny, A., 1999, ApJ, 516, 315

Setti, G., & Woltjer, L., 1979, A&A, 76, L1

Shahbaz, T., Bandyopadhyay, R. M., Charles, P. A., Wagner, R. M., Muhli, P., Hakala, P., Casares, J., & Greenhill, J., 1998, MNRAS, 300, 1035

Shakura, N. I., Ketsaris, N. A., Prokhorov, M. E., & Posnov, K. A., 1998, MNRAS, 300, 992

Shields, G. A., McKnee, C. F., Lin, D. N. C., & Begelman, M. C., 1986, ApJ, 306, 90

Šimon, V., 2002, A&A, 381, 151

Simonetti, J. H., Cordes, J. M., & Heeschen, D. S., 1985, ApJ, 296, 46

Slettebak, A., 1988, PASP, 100, 770

Smale, A. P., & Lochner, J. C., 1992, ApJ, 395, 582

Smith, D. A., & Done, C., 1996, MNRAS,

280, 355

Smith, D. M., Heindl, W. A., & Swank, J. H., 2002, ApJ, 578, L129

Soria, R., Wu, K., & Johnston, H. M., 1998, in Abstracts of the 19th Texas Symposium on Relativistic Astrophysics and Cosmology, held in Paris, France, Dec. 14-18, 1998. Eds.: J. Paul, T. Montmerle, and E. Aubourg (CEA Saclay).

Staubert, R., König, M., Friedrich, S., Lamer, G., Sood, R. K., James, S. D., & Sharma, D. P., 1994, A&A, 288, 513

Staubert, R., Schandl, S., & Wilms, J., 2000, in Proc. 5th Compton Symposium, ed. M. McConnell, J. Ryan, (Woodbury: AIP), 153

Steinle, H., et al., 1998, A&A, 330, 97

Steinle, H., et al., 1999, Adv. Space Res., 23, 911

Steinle, H., Dennerl, K., & Englhauser, J., 2000, A&A, 357, L57

Stellingwerf, R. F., 1978, apj, 224, 953

Stollberg, M. T., 1997, *Ph.D. thesis*, University of Alabama in Huntsville

Strüder, L., et al., 2001, A&A, 365, L18

Szatmáry, K., Vinkó, J., & Gál, J., 1994, aa, 108, 377

Tagliaferri, G., Bao, G., Israel, G. L., Stella, L., & Treves, A., 1996, ApJ, 465, 181

Tanaka, Y., Nandra, K., & Fabian, A. C., 1995, Nat, 375, 659

Terrell, J., 1986, ApJ, 300, 669

Terrell, N. J., 1972, ApJ, 174, L35

Thompson, C., & Duncan, R. C., 1996, ApJ, 473, 322

Timmer, J., & König, M., 1995, A&A, 300, 707

Trümper, J., Kahabka, P., Ögelman, H., Pietsch, W., & Voges, W., 1986, ApJ, 300, L63

Turner, P. C., Forrest, W. J., Pipher, J. L., & Shure, M. A., 1992, ApJ, 393, 648

Turner, T. J., George, I. M., Mushotzky, R. F., & Nandra, K., 1997a, ApJ, 475, 118

Turner, T. J., George, I. M., Nandra, K., & Mushotzky, R. F., 1997b, ApJS, 113, 23

Turner, T. J., George, I. M., Nandra, K., & Turcan, D., 1999, ApJ, 524, 667

Urry, C. M., & Padovani, O., 1995, PASP, 107, 803

Uttley, P., & McHardy, I. M., 2001, MNRAS, 323, L26

van der Klis, M., 1989, in Timing neutron stars, ed. H. Ögelman, E. van den Heuvel, (Dordrecht: Kluwer), 27

van der Klis, M., 1994, ApJS, 92, 511

van der Klis, M., 1995, in Lewin, van Paradijs & van den Heuvel (1995), Chapt. 6, 252–307

van der Klis, M., Jansen, F., van Paradijs, J., Lewin, W. H. G., van den Heuvel, E. P. J., Trümper, J. E., & Sztajno, M., 1985, Nat, 316, 225

van Paradijs, J., 1996, ApJ, 464, L139

van Paradijs, J., Taam, R. E., & van den Heuvel, E. P. J., 1995, A&A, 299, L41

Watson, M. G., 1976, MNRAS, 176, 19

Webster, B. L., & Murdin, P., 1972, Nat, 235, 37

Wen, L., Remillard, R. A., & Bradt, H. V., 2000, ApJ, 532, 1119

White, N. E., Nagase, F., & Parmar, A. N., 1995, in Lewin, van Paradijs & van den Heuvel (1995), Chapt. 1, 1–57

Wijers, R. A. M. J., & Pringle, J. E., 1999, MNRAS, 308, 207

Wijnands, R., Miller, J. M., & van der Klis, M., 2002, MNRAS, 331, 60

Wijnands, R. A. D., Kuulkers, E., & Smale, A. P., 1996, ApJ, 473, L45

Wilms, J., 1998, *Ph.D. thesis*, Eberhard Karls Universität Tübingen

Wilms, J., Nowak, M. A., Dove, J. B., Fender, R. P., & di Matteo, T., 1999, ApJ, 522, 460

Wilms, J., Nowak, M. A., Pottschmidt, K., Heindl, W. A., Dove, J. B., & Begelman,

M. C., 2001, MNRAS, 320, 327

Wilson, C. A., Finger, M. H., COe, M. J., & Negueruela, I., 2003, ApJ, 584, 996

Wojdowski, P., Clark, G. W., Levine, A. M., Woo, J. W., & Zhang, S. N., 1998, ApJ, 502, 253

Woźniak, P. R., Zdziarski, A. A., Smith, D., Madejski, G. M., & Johnson, W. N., 1998, MNRAS, 299, 449

Yaqoob, T., McKernan, B., Ptak, A., Nandra, K., & Serlemitsos, P. J., 1997, ApJ, 490, L25

Yule, G. U., 1927, Phil. Trans. R. Soc. A, 226, 304

Zdziarski, A. A., Poitaten, J., PCaiesas, W. S., & Wen, L., 2002, ApJ, 578, 357

Zhang, S. N., Robinson, C. R., Wilson, R. B., Harmon, B. A., Scott, D. M., & Remillard, R., 1996, IAU Circ., 6468, 1

Zhang, S. N., Yu, W., & Zhang, W., 1998, ApJ, 494, L71

Zhang, W., Jahoda, K., Kelley, R. L., Strohmayer, T. E., Swank, J. H., & Zhang, S. N., 1998, Astrophys. J., Lett., 495, L9

Zhang, W., Jahoda, K., Swank, J. H., Morgan, E. H., & Giles, A. B., 1995, ApJ, 449, 930

Zhang, W., Morgan, E. H., Jahoda, K., Swank, J. H., Strohmayer, T. E., Jernigan, G., & Klein, R. I., 1996, Astrophys. J., Lett., 469, L29

List of Abbreviations

ADAF	: Advection Dominated Accretion Flow	IS	: Intermediate State
AGN	: Active Galactic Nuclei	LINERS	: Low-Ionization Nuclear Emission-Line Regions
AR	: Autoregressive processes	LMXB	: Low Mass X-ray Binaries
ASM	: All-Sky Monitor	LS	: Low/hard State
AXP	: Anomalous X-ray Pulsars	LSSM	: Linear State Space Model
BATSE	: Burst and Transient Source Experiment	MIT	: Massachusetts Institute of Technology
BH	: Black Hole	NELG	: Narrow-Emission-Line Galaxies
BHXB	: Black Hole X-ray Binary		
BL Lac	: BL Lacertae	NASA	: National Aeronautics and Space Administration
BLR	: Broad-Line Region		
BLRG	: Broad-Line Radio Galaxies	NLR	: Narrow Line Region
CASS	: Center for Astrophysics and Space Sciences	NS	: Neutron Star
		OVV	: Optically Violently Variable
CGRO	: Compton Gamma Ray Observatory	PCA	: Proportional Counter Array
		PCU	: proportional Counter Units
CV	: Cataclysmic Variable	PD	: Power Diagram
DFT	: Discrete Fourier Transform	PDM	: Phase Dispersion Minimization
EPF	: Excess Pair Fraction		
FFT	: Fast Fourier Transform	PSD	: Power Spectral Density or Periodogram
FR 1	: Fanaroff-Riley type I radio galaxies		
		QPO	: Quasi Periodic Oscillations
FR 2	: Fanaroff-Riley type II radio galaxies	QSO	: Quasi-Stellar Objects
		ROSAT	: Röntgensatellit
GSFC	: NASA Goddard Space Flight Center	*RXTE*	: Rossi X-ray Timing Explorer
		SAA	: South Atlantic Anomaly
HMXB	: High Mass X-ray Binaries	SF	: Structure Function
HS	: High/soft State	SSRQ	: Steep Spectrum Radio Quasars
HEASARC	: High Energy Astrophysics Science Archive Research Center	SXT	: Soft X-ray Transient
		UT	: Universal Time
		VHS	: Very High State
HEXTE	: High Energy X-ray Timing Experiment	WD	: White Dwarf
		XMM	: X-ray Multi-Mirror Mission
IAAT	: Institut für Astronomie und Astrophysik Tübingen	XRB	: X-ray Binary
		$\chi^2(P)$	: Epoch-folding

Acknowledgments

Curriculum Vitae

27.05.1972:	Born in Madrid, Spain
1978–1979:	Primary school Estados Unidos de América, Madrid
1979–1980:	Primary school Las Dominicas, Valencia
1980–1986:	Primary and Secondary El Armelar, Valencia
1986–1990:	High School El Armelar, Valencia
06.1990:	School leaving certificate (*Abitur*)
1990–1997:	University of Valencia, studies in Mathematical Sciences
1994–1995:	ERASMUS fellowship (of the European Economic Community) to carry out academic studies at the Eberhard Karl Universität Tübingen (Germany), complemented with BANCAJA-ERASMUS fellowship
1995–1997:	Collaboration in the project LEGRI at the Astronomy and Space Science Group of the University of Valencia headed by Prof. Dr. V. Reglero with the development of the LEGRI's Software (imaging) in Minisat-01 mission
07.1997:	Degree in Mathematical Sciences; Special field Astronomy and Astrophysics
04.1998–09.1998:	Statistical scientific auxiliary worker at the Institut für medizinische Biometrie at the Eberhard Karl Universität Tübingen
09.1998–09.1999:	La Caixa-DAAD Scholarship for doctoral studies at the section Astronomy of the Institut für Astronomie und Astrophysik Tübingen (IAA Tübingen) at the Eberhard Karl Universität Tübingen
10.1999–12.1999:	Scientific auxiliary worker at the IAA Tübingen
09.1998–08.2003:	Preparation of the thesis with the title "Long-term X-ray variability of Active Galactic Nuclei and X-ray Binaries" at the IAA Tübingen under supervision of Prof. Dr. R. Staubert
01.2000–:	Scientific employee at the IAA Tübingen

Aside from the professors of the University of Valencia, my academic teachers of the University of Tübingen have been the professors and lecturers: R. Nagel, R. Staubert, K. Werner, J. Wilms, and S. Dreizler